

CKM unitarity puzzle with Abelian flavour symmetries

Ricardo António da Silva Amadeu

Thesis to obtain the Master of Science Degree in

Engineering Physics

Supervisors: Prof. Doutor Filipe Rafael Joaquim

Prof. Henrique Pedro Fernandes de Noronha Brito Câmara

Examination Committee

Chairperson: Prof. Doutor Mário João Martins Pimenta

Supervisor: Prof. Doutor Filipe Rafael Joaquim

Member of the Committee: Prof.^a Doutora Maria Margarida Nesbitt Rebelo da Silva

May 2024

"Explore the world.

Nearly everything is really interesting if you go into it deeply enough."

Richard P. Feynman

Declaration

I declare that this document is an original work of my own authorship and that it fulfills all the requirements of the Code of Conduct and Good Practices of the Universidade de Lisboa.

Acknowledgments

Firstly, I would like to deeply thank my supervisors, Professor Filipe Rafael Joaquim and Henrique Brito Câmara, for the relentless, everpresent support and invaluable insights that greatly elevated the quality of this work. I feel truly honored and grateful for being provided with such a fruitful learning experience.

I thank my mother, for the unfathomable support and words of reassurance, and my father, for always driving me to strive for more. To my lovely sister, I express my gratitude for the shared carefree and playful moments in stressful times.

I thank my friends, especially Francisco, Joana and João, for always being a safe haven of heartwarming affection. Your truly endearing words always uplift me in my moments of despair.

Resumo

Um desenvolvimento recente nas medidas da primeira linha da matriz Cabibbo-Kobayashi-Maskawa, conhecido na literatura como anomalia do ângulo de Cabibbo, está em tensão com a previsão de mistura de quarks unitária.

Nesta tese consideramos uma extensão do Modelo Padrão com um isosinglete quark do tipo vetor. Fermiões do tipo vetor são campos de matéria cujas componentes de direita e esquerda estão na mesma representação do grupo de gauge do Modelo Padrão. A inclusão destas partículas resulta numa matriz de mistura de quarks não unitária, sendo esta uma possível explicação da anomalia do ângulo de Cabibbo. Tratamos do puzzle de sabor através da identificação do conjunto maximamente restritivo de texturas zero nas matrizes de massa dos quarks, compatíveis com os dados das massas e mistura dos quarks. Determinamos o cenário mínimo para implementação destas texturas, que consiste em estender o sector escalar com um segundo dubleto de Higgs e uma única simetria $U(1)$ Abelianiana de sabor. Em seguida, procedemos à exploração das consequências fenomenológicas do modelo. Focamo-nos na física do sabor, nomeadamente na mistura de mesões neutros, decaimentos de mesões e decaimentos raros do quark top. Mostramos que o poder restritivo dos processos de sabor varia consoante os diferentes padrões de texturas zero. Encontramos dois cenários interessantes, referidos por texturas 5_1^d e 5_3^s , que apresentam uma melhoria no ajuste da anomalia do ângulo de Cabibbo em relação ao Modelo Padrão. O processo de sabor mais restritivo para ambos os casos é a oscilação de mesões $D^0 - \bar{D}^0$.

Palavras-chave: Anomalia do ângulo de Cabibbo; quarks do tipo vetor; *puzzle* de sabor; texturas zero; simetrias Abelianas de sabor; correntes neutras com mudança de sabor.

Abstract

A recent development in the measurement of the first row of the Cabibbo-Kobayashi-Maskawa matrix is in tension with the prediction of unitary quark mixing, commonly known as Cabibbo angle anomaly.

In this thesis, we consider a Standard Model extension with an isosinglet vector-like quark. Vector-like fermions are matter fields whose right and left handed components fall under the same representation of the Standard Model gauge group. The inclusion of these particles result in a non-unitary quark mixing matrix, thus presenting a possible explanation of the Cabibbo angle anomaly. We address the flavour puzzle by identifying the set of maximally-restrictive texture zeros in quark Yukawa and mass matrices, compatible with quark masses and mixing data. We determine the minimal scenario for the implementation of these textures, consisting of an extended scalar sector with a second Higgs doublet and a single U(1) Abelian flavour symmetry. We then proceed to explore the phenomenological consequences of tree-level flavour changing neutral currents present in the model. We focus on flavour physics, specifically neutral meson mixing, meson decays and rare top decays. It is shown that the constraining power of flavour processes varies according to the different texture zeros patterns. Finally, we perform a global fit to both quark data and flavour phenomenology. We report two interesting scenarios, dubbed as 5_1^d and 5_3^s textures, that present an improvement in the fit of the Cabibbo angle anomaly compared to the Standard Model. The most constraining flavour process for both these cases is $D^0 - \bar{D}^0$ meson oscillations.

Keywords: Cabibbo angle anomaly; vector-like quarks; *flavour puzzle*; texture zeros; Abelian flavour symmetries; flavour changing neutral currents.

Contents

Acknowledgments	v
Resumo	vii
Abstract	ix
List of Tables	xiii
List of Figures	xvii
List of Abbreviations	xix
1 Introduction	1
2 The Standard Model of particle physics	4
2.1 Electroweak interactions and particle content	5
2.2 Electroweak symmetry breaking	8
2.2.1 Fermion masses and mixing	9
2.3 Cabibbo angle anomaly	10
3 Standard Model extensions with isosinglet vector-like quarks	15
3.1 Mass Lagrangian	15
3.2 Charged and neutral currents	17
3.3 Relation between CKM non-unitarity and flavour changing neutral currents	18
3.4 Vector-like quark mass scale and perturbativity bounds	21
4 Minimal SM extension with an up-type isosinglet vector-like quark	25
4.1 Maximally restrictive texture zeros for quarks	25
4.2 Abelian symmetry realisation of compatible textures	29
4.3 Parameter space scan	32
5 Flavour phenomenology	37
5.1 Observables	37
5.1.1 Meson mixing	38
5.1.2 Rare top decays	41
5.1.3 Rare meson decays	42
5.1.4 CP violation parameter ϵ'/ϵ	46
5.2 Results	47

5.2.1	Methodology	48
5.2.2	Global fits	52
5.2.3	Impact on the Cabibbo angle anomaly	59
6	Concluding remarks	63
	Bibliography	65
A	Non-realisable texture pairs	73
B	Inami-Lim functions	78

List of Tables

2.1	Particle content of the SM. The numbers between parenthesis define the representation of the fields under the $SU(3)_c$, $SU(2)_L$ and $U(1)_Y$ groups, in this order. For the matter fields, the third isospin component T_3 and electric charge Q is also presented. The index $i = 1, 2, 3$ concerns the generation/family of the fermions.	6
3.1	Possible VLQ representations under G_{SM} that can mix with SM quarks via Yukawa couplings, assuming a scalar sector comprised of only $SU(2)_L$ scalar doublets.	16
4.1	Current data for the SM quark masses, moduli of the CKM matrix entries without imposing unitarity and value of the γ phase [37].	26
4.2	Maximally-restrictive $(\mathcal{M}_u, \mathbf{M}_d)$ texture-zeros pairs compatible with quark data at 1σ level.	27
4.3	Maximally-restrictive $(\mathcal{M}_u, \mathbf{M}_d)$ texture-zeros pairs compatible with quark data only at 3σ level.	27
4.4	Textures for the 3×3 SM down-type quark mass matrix \mathbf{M}_d	28
4.5	Textures for the full 4×4 up-type quark mass matrix \mathcal{M}_u , featuring 10 and 11 zeros.	28
4.6	Textures for the full 4×4 up-type quark mass matrix \mathcal{M}_u , featuring 9 zeros.	29
4.7	Textures for the full 4×4 up-type quark mass matrix \mathcal{M}_u , featuring 8 zeros.	30
4.8	Maximally-restrictive texture sets $(\mathcal{M}_u, \mathbf{M}_d)$ realisable through an Abelian flavour symmetry $U(1)_F$. We provide the field transformation charges under $U(1)_F$ expressed as multiples of an arbitrary charge q_F	32
4.9	Decomposition of mass matrices into the Yukawa or bare mass textures, according to Eqs. (4.6) and (4.7), for the maximally-restrictive texture pairs $(\mathcal{M}_u, \mathbf{M}_d)$ of Table 4.8.	32
4.10	Quark mass matrices identified applying the χ^2 minimisation procedure described in Sec. 4.1 to the maximally-restrictive textures presented in Table 4.8. The superscript $q = d, s, b$ corresponds to the decoupled down quark state. The results are presented in units of MeV.	35
5.1	SM physical constants taken from the PDG [37].	38
5.2	Numerical values used in meson mixing calculations.	42
5.3	Numerical values used in rare top decays calculations.	42
5.4	Numerical values used in meson decays calculations.	46
5.5	Numerical values used in ϵ'/ϵ calculations.	47

5.6	Quark mass matrices identified applying the χ^2 minimisation procedure described in Sec. 5.2 to the maximally-restrictive textures presented in Table 4.8. The subscript $q = d, s, b$ corresponds to the decoupled down quark state. The results are presented in units of MeV.	50
5.7	Mixing \mathbf{V} and FCNC \mathbf{F}^u matrices corresponding to the texture pairs identified in Table 5.6. The subscript $q = d, s, b$ corresponds to the decoupled down quark state.	51
5.8	Model predictions for $\Delta_{\text{SM}}^{B_d}$ and $\Delta_{\text{NP}}^{B_d}$ for each texture pair identified in Table 5.6. Comparing the ratios $\Delta_{\text{NP}}^{B_d}/\Delta_{\text{SM}}^{B_d}$ with the constraints in Eqs. (5.17) and (5.18), we observe that the texture pairs present consistently $\chi^2 \sim 1.6$ and $\chi^2 \sim 10.3$ tension in the real and imaginary parts of $\Delta_{\text{NP}}^{B_d}/\Delta_{\text{SM}}^{B_d}$ respectively.	54
5.9	Model predictions for $\Delta_{\text{SM}}^{B_s}$ and $\Delta_{\text{NP}}^{B_s}$ for each texture pair identified in Table 5.6. Comparing the ratios $\Delta_{\text{NP}}^{B_s}/\Delta_{\text{SM}}^{B_s}$ with the constraints in Eqs. (5.19) and (5.20), we conclude that the texture pairs are compatible with B_s^0 meson oscillation data.	54
5.10	Model predictions for $ \Delta_{\text{NP}}^{K^0} $ and $ \text{Im}\Delta_{\text{NP}}^{K^0} $ for each texture pair identified in Table 5.6. Comparing these values with the bounds in Eqs. (5.15) and (5.16), we conclude that these texture pairs are compatible with kaon oscillation data.	55
5.11	Model predictions for $ \mathbf{F}_{cu}^u ^2$ for each texture pair identified in Table 5.6. Comparing these values with the upper bound in Eq. (5.22), we observe that the texture pairs are compatible with D^0 meson oscillation data at 1σ	55
5.12	Model predictions for $ \mathbf{F}_{tu}^u $ and $ \mathbf{F}_{tc}^u $ for each texture pair identified in Table 5.6. Comparing these values with the upper bounds in Eq. (5.25), we observe that the texture pairs are compatible with rare top decays data.	55
5.13	Model predictions regarding the $B_d^0 \rightarrow \mu^+\mu^-$ decay for each texture pair identified in Table 5.6 [check the terms in Eqs. (5.32) and (5.34)]. Comparing these values with the constraint in Eq. (5.36), we observe that the texture pairs are compatible with $B_d^0 \rightarrow \mu^+\mu^-$ data. We denote $\Delta_{\text{NP}}^{\text{pen.}} = \sum \mathbf{V}_{id}^* (\mathbf{F}_{ij}^u - \delta_{ij}) \mathbf{V}_{jb} N(x_i, x_j)$	56
5.14	Model predictions regarding the $B_s^0 \rightarrow \mu^+\mu^-$ decay for each texture pair identified in Table 5.6 [check the terms in Eqs. (5.32) and (5.34)]. Comparing these values with the constraint in Eq. (5.37), we observe that the texture pairs present a tension with $B_s^0 \rightarrow \mu^+\mu^-$ data at $\sim 1.73\sigma$. We denote $\Delta_{\text{NP}}^{\text{pen.}} = \sum \mathbf{V}_{is}^* (\mathbf{F}_{ij}^u - \delta_{ij}) \mathbf{V}_{jb} N(x_i, x_j)$	56
5.15	Model predictions regarding the $\text{Br}(K_L \rightarrow \mu^+\mu^-)_{\text{SD}}/\text{Br}(K^+ \rightarrow \mu^+\nu)$ ratio for each texture pair identified in Table 5.6 [check the terms in Eqs. (5.33) and (5.35)]. Comparing these values with the constraint in Eq. (5.38), we observe that the texture pairs are compatible with experimental data. We denote $\Delta_{\text{NP}}^{\text{pen.}} = \sum \eta_i^Y \text{Re} [\mathbf{V}_{is}^* (\mathbf{F}_{ij}^u - \delta_{ij}) \mathbf{V}_{jd}] N(x_i, x_j)$. The column “Value” presents the theoretical value computed from the bound (5.38).	57

5.16	Model predictions regarding the $\text{Br}(K^+ \rightarrow \pi^+ \nu \bar{\nu}) / \text{Br}(K^+ \rightarrow \pi^0 e^+ \bar{\nu})$ ratio for each texture pair identified in Table 5.6 [check the terms in Eqs. (5.39) and (5.41)]. Comparing these values with the constraint in Eq. (5.43), we observe that the texture pairs are compatible with $\text{Br}(K^+ \rightarrow \pi^+ \nu \bar{\nu}) / \text{Br}(K^+ \rightarrow \pi^0 e^+ \bar{\nu})$ data at $\sim 1\sigma$. We denote $\Delta_{\text{NP}}^{\text{pen.}} = \sum \eta_i^X \mathbf{V}_{is}^* (\mathbf{F}_{ij}^u - \delta_{ij}) \mathbf{V}_{jd} N(x_i, x_j)$. The column “Value” presents the theoretical value computed from the bound (5.43).	57
5.17	Model predictions regarding the $\text{Br}(K_L \rightarrow \pi^0 \nu \bar{\nu}) / \text{Br}(K_L \rightarrow \pi^0 \nu \bar{\nu})_{\text{SM}}$ ratio for each texture pair identified in Table 5.6 [check the terms in Eqs. (5.40) and (5.42)]. Comparing these values with the constraint in Eq. (5.44), we observe that the texture pairs are compatible with $\text{Br}(K_L \rightarrow \pi^0 \nu \bar{\nu}) / \text{Br}(K_L \rightarrow \pi^0 \nu \bar{\nu})_{\text{SM}}$ data. We denote $\Delta_{\text{NP}}^{\text{pen.}} = \sum \mathbf{V}_{is}^* (\mathbf{F}_{ij}^u - \delta_{ij}) \mathbf{V}_{jd} N(x_i, x_j)$. The column “Value” presents the theoretical value computed from the bound (5.44).	58
5.18	Model predictions regarding the CP violation parameter ϵ/ϵ' for each texture pair identified in Table 5.6 [check the terms in Eqs. (5.45) and (5.53)]. Comparing these values with $\epsilon/\epsilon' = (1.66 \pm 0.23) \times 10^{-3}$ [37], we observe that the texture pairs are compatible with ϵ/ϵ' data. We denote $\Delta_{\text{NP}}^{\text{pen.}} = (P_X + P_Y + P_Z) \sum_{i,j=u,c,t,T} \text{Im} [\mathbf{V}_{is}^* (\mathbf{F}_{ij}^u - \delta_{ij}) \mathbf{V}_{jd} N(x_i, x_j)]$. . .	58
A.1	Classification of textures for the full 4×4 up-type quark mass matrix under conditions (A.1) and (A.2).	74
A.2	Classification of textures for the 3×3 SM down-type quark mass matrix under conditions (A.1) and (A.2).	74
A.3	Possible decompositions of $\mathbf{M}_u^{\text{Yuk.}}$ and \mathbf{M}_d for the textures 10_1^u and 4_1^d . The entries 1 and 2 correspond to non-zero entries coupled to Φ_1 and Φ_2 , respectively. The \times entries of the textures 11^u and 5^d may couple to either Φ_a	76
A.4	Incompatibility under (A.3) between each of the decompositions of 11_1^u and the respective forbidden down texture pairings.	77
A.5	Incompatibility under (A.3) between each of the decompositions of 10_1^u and 10_3^u and the respective forbidden down texture pairings.	77
A.6	Incompatibility under (A.3) between each of the decompositions of 9_9^u and the respective forbidden down texture pairings. For the pairings $(9_{9A}^u, 5_3^d)$ and $(9_{9B}^u, 5_1^d)$, we present the results for the \times entry of 5^d coupling to $\Phi_1 \Phi_2$. The checkmarks correspond to the decompositions presented in Table 4.9.	77

List of Figures

2.1	Semileptonic $Kl3$ decay tree-level diagram. The quark q corresponds to a $d(u)$ quark when representing the decay of a $K^0(K^+)$ meson into a $\pi^-(\pi^0)$ meson, respectively.	11
2.2	$K^-(\pi^-)$ leptonic decay diagram for $q = s(d)$	12
2.3	Superaligned $0^+ - 0^+$ nuclear and free neutron β -decays diagram.	13
2.4	The values of $ (\mathbf{V}_{\text{CKM}})_{us} $ from Eq. (2.33), $ (\mathbf{V}_{\text{CKM}})_{ud} $ from Eq. (2.40) and $ (\mathbf{V}_{\text{CKM}})_{us}/(\mathbf{V}_{\text{CKM}})_{ud} $ from Eq. (2.35) correspond to the purple, red and blue regions. The green cross represents the best fit point (bfp). The green curves delimit the 1σ , 2σ and 3σ contours, which correspond to $\Delta\chi^2_{\text{non-uni.}} = 2.3; 6.18; 11.83$. The black curve is obtained from the unitarity constraint of the first row of \mathbf{V}_{CKM} . The dashed black curve corresponds to the unitarity constraint corrected by δ_{CKM}	14
4.1	Constraints on the (x_2, θ) parameter space imposed by quark experimental data in Table 4.1. The 1, 2 and 3σ regions for $\Delta\chi^2$ are coloured in grey, blue and magenta, respectively. The green contours representing the 1, 2 and 3σ for $\Delta\chi^2_{\text{non-uni.}}$ are determined following the procedure described in Sec. 2.3.	34
5.1	Leading order contribution to $P^0 - \overline{P}^0$ mixing, where $u_i, u_j = u, c, t, T$. The K^0, B_d^0 and B_s^0 mesons correspond to $(\alpha, \beta) = (d, \bar{s}), (d, \bar{b}), (s, \bar{b})$	39
5.2	$D^0 - \overline{D}^0$ mixing via a tree level Z mediated FCNC.	41
5.3	Tree-level decay of the top quark via Z and Higgs mediated FCNC.	41
5.4	SM box diagram contributing to leptonic decays in unitary gauge. The semileptonic decay box is similar, with external neutrinos and the corresponding internal lepton.	43
5.5	SM Z -mediated penguin diagrams for leptonic and semileptonic decays in unitary gauge.	43
5.6	Self-energy diagrams inducing flavour-changing contributing to leptonic and semileptonic decays in unitary gauge.	43
5.7	NP penguin diagram with tree-level FCNC induced by the Z -boson in unitary gauge. The internal quarks are $u_i, u_j = u, c, t, T$	44

5.8	$((\mathbf{V}_{\text{CKM}})_{us} , (\mathbf{V}_{\text{CKM}})_{ud})$ points corresponding to the texture pairs in the Tables 4.10 and 5.6, represented as circles and triangles, respectively (see text for details). The purple error bars correspond to the SM fit to quark mixing data in Ref. [37]. The green contours and black curves are analogous to the ones in Fig. 2.4. The magenta and brown diamonds represent the global fit results obtained when using $\eta_D = 0.25$ and $\eta_D = 1$ as input. . . .	60
5.9	Constraints on the (x_2, θ) parameter space imposed by quark experimental data in Table 4.1 and flavour phenomenology described in Sec 5.1. The 1, 2 and 3σ regions for $\Delta\chi^2$ are coloured in grey, blue and magenta, respectively. The green contours representing the 1, 2 and 3σ for $\Delta\chi^2_{\text{non-uni.}}$ are determined following the procedure described in Sec. 2.3. . . .	61
B.1	Inami-Lim functions for $m_T \in [0.1; 10]$ TeV. The dotted blue lines correspond to the values $S_0(x_t) = 2.52$ and $S_0(x_c) = 2.50 \times 10^{-4}$	80

List of Abbreviations

2HDM	Two-Higgs-doublet model
BR	Branching ratio
BSM	Beyond the standard model
CC	Charged current
CKM	Cabibbo-Kobayashi-Maskawa
CAA	Cabibbo angle anomaly
CP	Charge-conjugation and parity
EW	Electroweak
EWSB	Electroweak symmetry breaking
FCNC	Flavour changing neutral currents
GIM	Glashow-Iliopoulos-Maiani
H.c.	Hermitian conjugate
LH	Left-handed
LHC	Large hadron collider
NC	Neutral current
NP	New Physics
RH	Right-handed
SM	Standard model
SNF	Smith normal form
SSB	Spontaneous symmetry breaking
VEV	Vacuum expectation value
VLQ	Vector-like quarks
WB	Weak basis

Chapter 1

Introduction

The Standard Model (SM) of particle physics, considered to be one of the greatest theoretical achievements of Physics, successfully describes the electroweak (EW) and strong interactions among the elementary particles known to mankind. It has withstood extensive experimental tests, showing a great level of agreement between experimental observations and theoretical predictions. The discovery of the Higgs boson at the CERN Large Hadron Collider (LHC), in 2012 by the ATLAS [1] and CMS [2] collaborations, whose existence had been predicted around 50 years before, was another testament of the success of the SM. However, there are several experimental evidences that the SM fails to explain. Namely, neutrino oscillations, which indicate that neutrinos are massive particles and that there is lepton mixing, the existence of dark matter, and the observed baryon asymmetry of the Universe, are phenomena that require beyond the SM (BSM) physics in order to be accounted for. This statement is further motivated by the fact that the SM leaves several of its features unanswered from a theoretical standpoint. Among which stands out the fact that SM does not provide a guiding principle to explain the observed fermion masses and mixing patterns, which is often referred to as the *flavour puzzle*.

Once the Higgs neutral component develops a non-zero vacuum expectation value (VEV), the EW symmetry is spontaneously broken (EWSB), and via the famous Brout-Englert-Higgs (BEH) mechanism [3–6], the EW gauge bosons acquire a non-zero mass while the photon remain massless. Through the couplings between the Higgs doublet and the fermions, known as the Yukawa sector of the SM, stem after EWSB fermion masses and quark mixing. Namely, the SM predicts a unitary Cabibbo-Kobayashi-Maskawa (CKM) matrix \mathbf{V}_{CKM} [7, 8], which encodes the couplings for quark charged currents (CC). The thorough study of these quantities provides a vital test to the SM. A recent reduction on the hadronic uncertainties in the short-distance radiative corrections to neutron and superallowed nuclear β decays [9], improved the computation of $|(\mathbf{V}_{\text{CKM}})_{ud}|$. Together with the precise determination of $|(\mathbf{V}_{\text{CKM}})_{us}|$ and $|(\mathbf{V}_{\text{CKM}})_{us}/(\mathbf{V}_{\text{CKM}})_{ud}|$, resulting from semileptonic $Kl3$, and kaon and pion leptonic decays, respectively, these currently are in tension with the unitarity condition of the first row of \mathbf{V}_{CKM} . Firstly, the $|(\mathbf{V}_{\text{CKM}})_{ud}|$ and $|(\mathbf{V}_{\text{CKM}})_{us}|$ values lead to a deficit in the first row unitarity. Secondly, the indirect determination of $|(\mathbf{V}_{\text{CKM}})_{us}|$ from the ratio $|(\mathbf{V}_{\text{CKM}})_{us}/(\mathbf{V}_{\text{CKM}})_{ud}|$ assuming unitarity disagrees with the direct measurement from the $Kl3$ decay. These discrepancies, collectively known as Cabibbo angle

anomaly (CAA), may provide a hint of BSM physics if confirmed by future experiments.

This non-unitarity hint has gathered the attention of the theoretical particle physics community with numerous proposals put forward to address it. Namely, an interesting framework to tackle the CAA relies on the extension of the SM particle content with vector-like quarks (VLQs) [10–33]. Vector-like fermions are under the same representation of the SM gauge group regardless of their chirality. Consequently, VLQs admit bare mass terms, contrary to the SM chiral quarks, which obtain mass via Yukawa couplings to the Higgs boson. This, in turn, results in a modification of the quarks couplings to the W boson: the mixing matrix \mathbf{V} containing the quark CC couplings, whose upper left 3×3 block corresponds to the \mathbf{V}_{CKM} matrix, is no longer unitary. This feature allows the deviation from unitarity in the first row of \mathbf{V}_{CKM} , presenting a possible solution to the CAA. However, the addition of VLQs to the SM induce tree-level flavour changing neutral currents (FCNC) mediated by the Z and H bosons, which violate the Glashow-Iliopoulos-Maiani (GIM) mechanism [34]. Hence, careful attention must be given to the phenomenological effects of FCNCs, namely its influence on meson mixing and decay observables, as well as FCNC mediated by rare top decays (see e.g. Refs [33, 35]).

An intriguing observation that has been eluding physicists for several decades is the highly hierarchical nature of fermion masses and mixing. The fermion masses in the SM span over six orders of magnitude¹. Regarding the structure of the quark mixing matrix \mathbf{V}_{CKM} , we observe that the absolute value of the diagonal entries are close to unity while the remaining entries exhibit the hierarchy: $|\mathbf{V}_{\text{CKM}}|_{us} \approx |\mathbf{V}_{\text{CKM}}|_{cd} \sim 0.225$, $|\mathbf{V}_{\text{CKM}}|_{cb} \approx |\mathbf{V}_{\text{CKM}}|_{ts} \sim 0.04$, and $|\mathbf{V}_{\text{CKM}}|_{ub} \sim |\mathbf{V}_{\text{CKM}}|_{td} < 10^{-2}$ [37]. These values originate from Yukawa couplings of fermions to the Higgs boson, which are unrestrained in the SM. An interesting approach to increase the predictivity of the theory, while maintaining compatibility with data, is to reduce the number of free parameters in the Yukawa and mass matrices by imposing texture zeros [38–41]. This can be achieved in a simple manner via horizontal Abelian symmetries that can be discrete \mathbb{Z}_N and/or continuous $U(1)$ [42–56], that forbid specific quark couplings to the Higgs field. However, enforcing texture zeros with Abelian symmetries in the context of the SM is not viable, as they would lead either to massless quarks and/or vanishing mixing angles [46, 53, 54]. Consequently, one of the simplest extensions of the SM that allows for the implementation of such symmetries is the two-Higgs-doublet model (2HDM) [57]. In fact, Abelian symmetries have been previously employed within the 2HDM to tackle the *flavour puzzle* [45, 46, 53, 54].

Inspired by the above ideas, in this thesis we consider a minimal extension of the SM featuring a isosinglet up-type VLQ and a 2HDM scalar sector. Furthermore, we will supplement this framework with the minimal Abelian flavour symmetry group which implements the most restrictive flavour patterns, while maintaining compatibility with current quark data. Our aim is to provide a mechanism that addresses both the *flavour puzzle* and the CAA in a predictive scenario. Moreover, we also verify if this minimal model sustains stringent quark flavour constraints by investigating the phenomenological implications stemming from tree-level FCNC induced by VLQ mixing.

This thesis is organised as follows. In Chapter 2, we review the fundamental aspects of the SM, focusing on the EW sector, the BEH mechanism and quark masses and mixing. We also discuss the

¹This interval is increased to at least nine order of magnitude if we include the current bounds on neutrino masses [36].

current tension in the first row unitarity of \mathbf{V}_{CKM} , explaining in detail the CAA. The general features of SM extensions with an arbitrary number of up and down-type isosinglet VLQs are addressed in Chapter 3. We start by describing the modifications on the EW and Higgs interactions, followed by a discussion on the relation between non-unitarity of \mathbf{V}_{CKM} and FCNC. We also explore the impact of perturbativity bounds and the VLQ mass scale on deviations from unitarity. Focusing on the case of a single isosinglet up-type VLQ, in Chapter 4, we identify the maximally-restrictive texture zeros consistent with quark data. We then proceed to determine in Sec. 4.2 the textures realisable within a 2HDM. In Sec. 4.3 we comment on the constraints imposed by quark data on the parameter space of the mass matrices. The phenomenological constraints of flavour physics are analysed in Chapter 5. We briefly review the theoretical framework of neutral meson mixing, rare meson decays and top decays in the SM, as well as the new physics (NP) effects introduced by the VLQ. We then discuss the results obtained from a global fit, of the identified textures in Sec. 4.2, to all aforementioned experimental restrictions. Finally, in Chapter 6 we summarize the findings and concluding remarks of this work. Details regarding the maximally-restrictive quark textures and the Inami-Lim functions used in the computations of quark flavour processes are collected in the appendices.

Chapter 2

The Standard Model of particle physics

The SM is the culmination of several physicists contributions during the second half of the 20th century. Yang and Mills published in 1954 a groundbreaking paper extending gauge theories to non-abelian groups [58], which would later on constitute the mathematical foundation of the SM. In 1961, Glashow proposed that the electromagnetic and weak interactions may be unified through "partial symmetries", i.e. only part of the EW Lagrangian would exhibit gauge invariance [59]. In the same year, Nambu and Jona-Lasinio [60, 61] pioneered the application of spontaneous symmetry breaking (SSB) to particle physics, which provides a mechanism to generate particle mass terms. Goldstone [62] showed that SSB leads to the emergence of a massless scalar for each continuous symmetry spontaneously broken by scalars with non zero vacuum expectation values (VEV). In 1964, Brout and Englert [3], Higgs [4, 5] and Guralnik, Hagen and Kibble [6] showed that the massless scalars resulting from SSB of a local gauge symmetry are non-physical and ensure gauge invariance. In fact, these scalars correspond to the longitudinal component of massive vector bosons. This procedure is commonly known as the BEH mechanism. In 1967-68, A. Salam and S. Weinberg [63, 64] proposed a non-abelian gauge theory based on the $SU(2)_L \times U(1)_Y$ group which unified the EW interactions. The elementary particles in this model obtain mass through the BEH mechanism. A model addressing the strong interactions was independently proposed by Gell-Mann [65] and Zweig [66] in 1964. Finally, in 1971-2, 't Hooft and Veltmann [67, 68] proved the renormalisability of the theory.

In this chapter, after reviewing the EW sector of the SM, we discuss the commonly known *flavour puzzle*, a SM limitation concerning the lack of a theoretical framework that explains the observed structure of fermion masses and mixing [69]. This analysis is focused on a recent hint of new physics (NP) regarding the unitarity deficit of the first row of the quark mixing matrix.

2.1 Electroweak interactions and particle content

The SM is a non-abelian gauge quantum field theory with internal symmetry group

$$G_{\text{SM}} = \text{SU}(3)_c \times \text{SU}(2)_L \times \text{U}(1)_Y, \quad (2.1)$$

under which the SM Lagrangian

$$\mathcal{L}_{\text{SM}} = \mathcal{L}_{\text{QCD}} + \mathcal{L}_{\text{gauge}} + \mathcal{L}_{\text{fermion}} + \mathcal{L}_{\text{Higgs}} + \mathcal{L}_{\text{Yuk}}. \quad (2.2)$$

must be locally invariant. This requirement, known as the gauge principle, introduces real massless vector fields in the SM in order to preserve local invariance. These gauge vector fields, which are in the adjoint representation of the gauge group, correspond, after being quantised, to the gauge bosons. Gauge invariance under the $\text{SU}(3)_c$, where c stands for colour, results in the introduction of 8 gluon fields G_μ^k , ($k = 1, \dots, 8$), that mediate the strong interactions. Analogously, the $\text{SU}(2)_L \times \text{U}(1)_Y$, where L and Y stands for left-handness and weak hypercharge, respectively, leads to 4 gauge bosons, W_μ^i , ($i = 1, 2, 3$) from $\text{SU}(2)_L$ and B_μ from $\text{U}(1)_Y$. In what follows, for our purposes we focus on the EW sector.

While the number of gauge bosons is fixed by the symmetry group of the SM, the number of fermion and scalar fields in the SM is determined empirically. Besides the gauge bosons, the SM contains 3 generations of fermions, which are classified as leptons [singlets under $\text{SU}(3)_c$] and quarks [triplets under $\text{SU}(3)_c$], and a scalar Φ [doublet under $\text{SU}(2)_L$]. The fermion fields are described by a 4-component Dirac spinor ψ which can be decomposed into their chiral right-handed (RH) and left-handed (LH) components, defined as:

$$\psi = \psi_R + \psi_L, \quad \psi_R = \frac{1 + \gamma_5}{2} \psi = P_R \psi, \quad \psi_L = \frac{1 - \gamma_5}{2} \psi = P_L \psi, \quad (2.3)$$

where the ψ_R and ψ_L two-component Weyl spinors are eigenstates of γ_5 ¹, with chirality (eigenvalue of γ_5) $+1$ and -1 , respectively. The particle content of the SM is summarised in Table 2.1.

In principle, the Dirac Lagrangian

$$\mathcal{L}_{\text{Dirac}} = i\bar{\psi}\not{\partial}\psi - m\bar{\psi}\psi, \quad (2.4)$$

where $\not{\partial} = \gamma^\mu \partial_\mu$, would correctly describe the fermion field ψ . However, it presents two major issues. Firstly, the kinetic term is not invariant under G_{SM} . To preserve gauge invariance, we substitute the ordinary derivative ∂_μ by the covariant derivative D_μ

$$\partial_\mu \longrightarrow D_\mu = \partial_\mu - ig \sum_{i=1}^3 \frac{\tau^i}{2} W_\mu^i - ig' \frac{Y}{2} B_\mu, \quad (2.5)$$

where g and g' are the coupling constants of $\text{SU}(2)_L$ and $\text{U}(1)_Y$, and τ^i are the Pauli matrices. Using

¹The matrix $\gamma_5 = i\gamma^0\gamma^1\gamma^2\gamma^3$, where γ^i ($i = 0, 1, 2, 3$) are Dirac matrices.

Gauge Fields		Rep. in G_{SM}		
$\text{SU}(3)_c$	G_μ^k ($k = 1, \dots, 8$)	$(\mathbf{8}, \mathbf{1}, 0)$		
$\text{SU}(2)_L$	W_μ^i ($i = 1, 2, 3$)	$(\mathbf{1}, \mathbf{3}, 0)$		
$\text{U}(1)_Y$	B_μ	$(\mathbf{1}, \mathbf{1}, 0)$		
Matter Fields		Rep. in G_{SM}	T_3	Q
Quarks	$q_{iL} = \begin{pmatrix} u_{iL} \\ d_{iL} \end{pmatrix}$	$(\mathbf{3}, \mathbf{2}, +1/3)$	$+1/2$	$+2/3$
			$-1/2$	$-1/3$
	u_{iR}	$(\mathbf{3}, \mathbf{1}, +4/3)$	0	$+2/3$
	d_{iR}	$(\mathbf{3}, \mathbf{1}, -2/3)$	0	$-1/3$
Leptons	$l_{iL} = \begin{pmatrix} \nu_{iL} \\ e_{iL} \end{pmatrix}$	$(\mathbf{1}, \mathbf{2}, -1)$	$+1/2$	0
			$-1/2$	-1
	e_{iR}	$(\mathbf{1}, \mathbf{1}, -2)$	0	-1
Higgs	$\Phi = \begin{pmatrix} \phi^+ \\ \phi^0 \end{pmatrix}$	$(\mathbf{1}, \mathbf{2}, +1)$	$+1/2$	$+1$
			$-1/2$	0

Table 2.1: Particle content of the SM. The numbers between parenthesis define the representation of the fields under the $\text{SU}(3)_c$, $\text{SU}(2)_L$ and $\text{U}(1)_Y$ groups, in this order. For the matter fields, the third isospin component T_3 and electric charge Q is also presented. The index $i = 1, 2, 3$ concerns the generation/family of the fermions.

the lowering and raising operators T_- and T_+ , we define the EW charged gauge bosons W_μ^\pm :

$$T_\pm = \frac{T^1 \pm iT^2}{\sqrt{2}} \implies W_\mu^1 T^1 + W_\mu^2 T^2 = W_\mu^+ T^+ + W_\mu^- T^- \implies W_\mu^\pm = \frac{W_\mu^1 \mp iW_\mu^2}{\sqrt{2}}. \quad (2.6)$$

The EW neutral gauge bosons Z_μ and A_μ are obtained from the rotation of the fields W_μ^3 and B_μ :

$$\begin{pmatrix} B_\mu \\ W_\mu^3 \end{pmatrix} = \begin{pmatrix} \cos \theta_w & \sin \theta_w \\ -\sin \theta_w & \cos \theta_w \end{pmatrix} \begin{pmatrix} A_\mu \\ Z_\mu \end{pmatrix}, \quad (2.7)$$

with the following definitions:

$$g = \frac{e}{\sin \theta_w}, \quad g' = -\frac{e}{\cos \theta_w}, \quad \sin \theta_w = -\frac{g'}{\sqrt{g^2 + g'^2}}, \quad \cos \theta_w = -\frac{g}{\sqrt{g^2 + g'^2}}, \quad (2.8)$$

where e is the electrical charge and θ_w is the weak mixing angle. We can finally rewrite the covariant derivative as:

$$D_\mu = \partial_\mu + ieQA_\mu - \frac{g}{\cos \theta_w}(T^3 - Q \sin^2 \theta_w)Z_\mu - ig(W_\mu^+ T^+ + W_\mu^- T^-), \quad (2.9)$$

where $Q = T_3 + \frac{Y}{2}$ is the electric charge operator given by the Gell-Mann-Nishijima relation [70].

Introducing the covariant derivative D_μ results in the kinetic terms for fermions and the interaction terms between fermions and EW gauge bosons described by

$$\mathcal{L}_{\text{fermion}} = \overline{q_{i_L}}(i\not{D})q_{i_L} + \overline{u_{i_R}}(i\not{D})u_{i_R} + \overline{d_{i_R}}(i\not{D})d_{i_R} + \overline{l_{i_L}}(i\not{D})l_{i_L} + \overline{e_{i_R}}(i\not{D})e_{i_R}, \quad (2.10)$$

Defining the following vectors in family space:

$$u_{L,R} = \begin{pmatrix} u_{1_{L,R}} \\ u_{2_{L,R}} \\ u_{3_{L,R}} \end{pmatrix}, \quad d_{L,R} = \begin{pmatrix} d_{1_{L,R}} \\ d_{2_{L,R}} \\ d_{3_{L,R}} \end{pmatrix}, \quad l_{L,R} = \begin{pmatrix} l_{1_{L,R}} \\ l_{2_{L,R}} \\ l_{3_{L,R}} \end{pmatrix}, \quad \nu_L = \begin{pmatrix} \nu_{1_L} \\ \nu_{2_L} \\ \nu_{3_L} \end{pmatrix}, \quad (2.11)$$

these terms are rearranged as:

$$\mathcal{L}_{\text{fermion}} = \overline{u}(i\not{D})u + \overline{d}(i\not{D})d + \overline{l}(i\not{D})l + \overline{\nu_L}(i\not{D})\nu_L + \mathcal{L}_{\text{CC}} + \mathcal{L}_{\text{NC}}, \quad (2.12)$$

where we have used the relations of Eq. (2.3).

The neutral currents (NC) $\mathcal{L}_{\text{NC}} = \mathcal{L}_{\text{NC}}^{\text{lepton}} + \mathcal{L}_{\text{NC}}^{\text{quark}}$, comprise of the interactions between fermions and the neutral EW gauge bosons A_μ and Z_μ ,

$$\begin{aligned} \mathcal{L}_{\text{NC}}^{\text{lepton}} &= e\overline{l}\gamma_\mu l A^\mu + \frac{g}{\cos\theta_w}\overline{l}\gamma_\mu \left(\sin^2\theta_w - \frac{P_L}{2}\right) l Z^\mu + \frac{g}{2\cos\theta_w}\overline{\nu_L}\gamma_\mu \nu_L Z^\mu, \\ \mathcal{L}_{\text{NC}}^{\text{quark}} &= e\left(-\frac{2}{3}\overline{u}\gamma_\mu u + \frac{1}{3}\overline{d}\gamma_\mu d\right) A^\mu \\ &\quad + \frac{g}{\cos\theta_w}\left[\overline{d}\gamma_\mu \left(\frac{1}{3}\sin^2\theta_w - \frac{P_L}{2}\right) d + \overline{u}\gamma_\mu \left(-\frac{2}{3}\sin^2\theta_w + \frac{P_L}{2}\right) u\right] Z^\mu, \end{aligned} \quad (2.13)$$

whereas $\mathcal{L}_{\text{CC}} = \mathcal{L}_{\text{CC}}^{\text{lepton}} + \mathcal{L}_{\text{CC}}^{\text{quark}}$, contain the interactions between the fermions and charged EW gauge bosons W_μ^\pm ,

$$\mathcal{L}_{\text{CC}}^{\text{lepton}} = \frac{g}{\sqrt{2}}(\overline{\nu_L}\gamma^\mu l_L W_\mu^+ + \overline{l_L}\gamma^\mu \nu_L W_\mu^-), \quad \mathcal{L}_{\text{CC}}^{\text{quark}} = \frac{g}{\sqrt{2}}(\overline{u_L}\gamma^\mu d_L W_\mu^+ + \overline{d_L}\gamma^\mu u_L W_\mu^-). \quad (2.14)$$

From the above equations we can infer that the couplings between fermions and the gauge bosons Z and W^\pm depend on the chirality of the fermions, i.e. weak interactions are chiral. Specifically, the charged bosons W^\pm only couple to LH fields.

The kinetic and self-interaction terms of the EW gauge bosons are given by:

$$\mathcal{L}_{\text{gauge}} = -\frac{1}{4}\sum_{i=1}^3 F_i^{\mu\nu} F_{\mu\nu}^i - \frac{1}{4}F^{\mu\nu} F_{\mu\nu}, \quad (2.15)$$

where

$$F_{\mu\nu}^i = \partial_\mu W_\nu^i - \partial_\nu W_\mu^i + g\sum_{j,k=1}^3 \epsilon_{ijk} W_\mu^j W_\nu^k, \quad F_{\mu\nu} = \partial_\mu B_\nu - \partial_\nu B_\mu. \quad (2.16)$$

2.2 Electroweak symmetry breaking

The other major problem of Eq. (2.4) is that the mass term:

$$-m_\psi \bar{\psi}\psi = -m_\psi (\bar{\psi}_L \psi_R + \bar{\psi}_R \psi_L) . \quad (2.17)$$

does not preserve gauge invariance, since it does not constitute a singlet of $SU(2)_L$ and LH and RH fermion fields have distinct hypercharges. However, the Dirac mass term would be invariant under an hypothetical $U(1)$ symmetry where both RH and LH fermion fields have identical charges. Furthermore, the $SU(2)_L \times U(1)_Y$ EW gauge group is not an explicit symmetry of Nature. In fact, it is electrical-charge conservation that is observed in Nature. Thus, the $SU(2)_L \times U(1)_Y$ must be broken down to $U(1)_Q$ in a process known as EW symmetry breaking (EWSB).

EWSB occurs when a field that acquires a non-zero VEV is introduced in \mathcal{L}_{SM} , rendering its ground-state not symmetric under $SU(2)_L \times U(1)_Y$. This field must be a scalar in order to preserve Lorentz invariance² and electrically neutral, in order to be invariant under $U(1)_Q$ ³. Furthermore, the scalar field must not be a singlet of $SU(2)_L$, otherwise this gauge group would remain unbroken. In the SM, EWSB is achieved via the simplest possible scalar field which satisfies the conditions above, a single $SU(2)_L$ doublet scalar field Φ , known as the Higgs field. The scalar sector of the SM $\mathcal{L}_{\text{Higgs}}$ is given by:

$$\mathcal{L}_{\text{Higgs}} = (D^\mu \Phi)^\dagger (D_\mu \Phi) - V(\Phi), \quad V(\Phi) = \mu^2 \Phi^\dagger \Phi + \lambda (\Phi^\dagger \Phi)^2, \quad \Phi = \begin{pmatrix} \phi^+ \\ \phi^0 \end{pmatrix}, \quad (2.18)$$

where the potential $V(\Phi)$ corresponds to the most general renormalisable scalar potential allowed by G_{SM} , with μ having mass dimension and λ being dimensionless. For the scalar potential to be bounded from below, λ must be positive. The parameter μ^2 controls EWSB, i.e. if $\mu^2 > 0$, the minimum of the potential occurs for $|\Phi| = 0$, and the $SU(2)_L \times U(1)_Y$ remains unbroken. However, for $\mu^2 < 0$, the minimum of the potential occurs for:

$$|\Phi|^2 = -\frac{\mu^2}{\lambda} = \frac{v^2}{2}, \quad (2.19)$$

where the VEV v is considered to be real without loss of generality. We can then parametrise the Higgs field around the minimum of the potential $V(\Phi)$ as:

$$\Phi = \frac{1}{\sqrt{2}} \begin{pmatrix} \sqrt{2} G^+ \\ v + H + iG^0 \end{pmatrix}, \quad \langle \Phi \rangle = \frac{1}{\sqrt{2}} \begin{pmatrix} 0 \\ v \end{pmatrix}, \quad (2.20)$$

The only gauge group generator of $SU(2)_L \times U(1)_Y$ that remains unbroken by the VEV of the Higgs field $\langle \Phi \rangle$ is the electric charge operator $Q = T_3 + \frac{Y}{2}$. $\mathcal{L}_{\text{Higgs}}$ is comprised of two parts: the covariant derivative of the Higgs fields and the scalar potential $V(\Phi)$. The covariant derivative results in: the kinetic terms of the scalar bosons; the interactions between gauge and scalar bosons; the mass terms of the gauge bosons.

²Remember that SM is a non-abelian gauge QFT, and as such \mathcal{L}_{SM} must be invariant under Lorentz transformations.

³To be precise, in gauge theories we first introduce scalar fields and respective VEVs, and then compute the unbroken gauge group generators. If only a single gauge group generator remains unbroken, we identify it as being the electric charge operator Q , since any physical theory must include conservation of electric charge.

The scalar potential contains the Higgs boson mass term and self-interaction terms of the scalar bosons. The masses of the gauge bosons are:

$$D_\mu \langle \Phi \rangle D^\mu \langle \Phi \rangle = m_W^2 W_\mu^- W^{+\mu} + \frac{m_Z^2}{2} Z_\mu Z^\mu, \quad m_W = \frac{gv}{2}, \quad m_Z = \frac{gv}{2 \cos \theta_w}, \quad (2.21)$$

and the Higgs boson mass is $m_H = \sqrt{-2\mu^2}$. The photon A_μ remains massless. This process of gauge bosons acquiring mass through $SU(2)_L \times U(1)_Y$ being spontaneously broken into $U(1)_Q$ is the well known BEH mechanism.

If we count the degrees of freedom (d.o.f) before and after EWSB, we would naively conclude that 3 d.o.f have been added to $\mathcal{L}_{\text{Higgs}}$. However, this is not the case, since the non-physical massless scalar bosons G^\pm and G^0 , commonly known as pseudo-Goldstone bosons, are absorbed in the longitudinal polarisations of the now massive gauge bosons W_μ^\pm and Z_μ . The non-physical scalar bosons can indeed be removed from the \mathcal{L}_{SM} through a gauge transformation, where only the massive Higgs boson remains. This gauge is known as the unitary gauge.

2.2.1 Fermion masses and mixing

We started the discussion in this section by stating that Dirac mass terms are not allowed by G_{SM} . However, these terms respect $U(1)_Q$ symmetry, hinting that fermion fields may acquire mass through EWSB. Indeed, with the introduction of the Higgs field Φ , new gauge invariant terms must be added to \mathcal{L}_{SM} :

$$\mathcal{L}_{\text{Yuk.}} = -\bar{l}_{Li}(\mathbf{Y}_l)_{ij}\Phi e_{Rj} - \bar{q}_{Li}(\mathbf{Y}_d)_{ij}\Phi d_{Rj} - \bar{q}_{Li}(\mathbf{Y}_u)_{ij}\tilde{\Phi} u_{Rj} + \text{H.c.}, \quad (2.22)$$

where $\mathbf{Y}_{l,d,u}$ are the 3×3 Yukawa coupling matrices in family space with arbitrary complex numbers, $\tilde{\Phi} = i\tau_2 \Phi^*$ and $i, j = 1, 2, 3$. After EWSB, we obtain

$$\mathcal{L}_{\text{mass}} = -\bar{e}_L \mathbf{M}_l e_R - \bar{d}_L \mathbf{M}_d d_R - \bar{u}_L \mathbf{M}_u u_R + \text{H.c.}, \quad \mathbf{M}_{l,d,u} = \frac{v}{\sqrt{2}} \mathbf{Y}_{l,d,u}, \quad (2.23)$$

which resemble Dirac mass terms. $\mathcal{L}_{\text{Yuk.}}$ also describes the interactions between fermions and scalar bosons. To obtain masses for the physical fermion fields, we must rotate the fermion fields from the weak eigenstate basis (WB) to the mass eigenstate basis:

$$\begin{aligned} l_L &= \mathbf{U}_L^l l_L^m, \quad l_R = \mathbf{U}_R^l l_R^m \implies \mathbf{D}_l = \text{diag}(m_e, m_\mu, m_\tau) = \mathbf{U}_L^{l\dagger} \mathbf{M}_l \mathbf{U}_R^l, \\ d_L &= \mathbf{U}_L^d l_L^m, \quad d_R = \mathbf{U}_R^d l_R^m \implies \mathbf{D}_d = \text{diag}(m_d, m_s, m_b) = \mathbf{U}_L^{d\dagger} \mathbf{M}_d \mathbf{U}_R^d, \\ u_L &= \mathbf{U}_L^u l_L^m, \quad u_R = \mathbf{U}_R^u l_R^m \implies \mathbf{D}_u = \text{diag}(m_u, m_c, m_t) = \mathbf{U}_L^{u\dagger} \mathbf{M}_u \mathbf{U}_R^u, \end{aligned} \quad (2.24)$$

where

$$l_{L,R}^m = \begin{pmatrix} e_{L,R} \\ \mu_{L,R} \\ \tau_{L,R} \end{pmatrix}, \quad d_{L,R}^m = \begin{pmatrix} d_{L,R} \\ s_{L,R} \\ b_{L,R} \end{pmatrix}, \quad u_{L,R}^m = \begin{pmatrix} u_{L,R} \\ c_{L,R} \\ t_{L,R} \end{pmatrix}. \quad (2.25)$$

The unitary matrices \mathbf{U} are defined from the bidiagonalisation of the mass matrices \mathbf{M} , whose non-negative singular values are the masses of the physical fermions. The absence of RH neutrinos in the SM forces neutrinos to be massless.

This rotation is performed on the whole \mathcal{L}_{SM} . The kinetic terms for the fermions and NC interactions remain invariant, since

$$\begin{aligned}\overline{\psi}_L \gamma_\mu \psi_L &\Rightarrow \overline{\psi}_L^m \mathbf{U}_L^{\psi\dagger} \gamma_\mu \mathbf{U}_L^\psi \psi_L^m = \overline{\psi}_L^m \gamma_\mu \psi_L^m, \\ \overline{\psi}_R \gamma_\mu \psi_R &\Rightarrow \overline{\psi}_R^m \mathbf{U}_R^{\psi\dagger} \gamma_\mu \mathbf{U}_R^\psi \psi_R^m = \overline{\psi}_R^m \gamma_\mu \psi_R^m.\end{aligned}\tag{2.26}$$

However, the quark CC are affected

$$\mathcal{L}_{\text{CC}}^{\text{quark}} = \frac{g}{\sqrt{2}} \left(\overline{u}_L^m \mathbf{V}_{\text{CKM}} \gamma^\mu d_L^m W_\mu^+ + \overline{d}_L^m \mathbf{V}_{\text{CKM}}^\dagger \gamma^\mu u_L^m W_\mu^- \right), \tag{2.27}$$

where $\mathbf{V}_{\text{CKM}} = \mathbf{U}_L^{u\dagger} \mathbf{U}_L^d$ is the unitary CKM matrix [7, 8]. A general $n \times n$ unitary matrix can be parameterised by $n(n-1)/2$ mixing angles and $n(n+1)/2$ phases. Therefore, \mathbf{V}_{CKM} would, in principle, depend on 3 mixing angle and 6 phases. However, 5 of these phases can be absorbed in a redefinition of the quark fields which leave the terms in \mathcal{L}_{SM} invariant. Thus, we conclude that \mathbf{V}_{CKM} depends only on 4 physical parameters: 3 mixing angles and a single charge-conjugation and parity (CP) violating phase δ . The standard parameterisation of the CKM matrix is given by [37]

$$\mathbf{V}_{\text{CKM}} = \begin{pmatrix} c_{12}c_{13} & s_{12}c_{13} & s_{13}e^{-i\delta} \\ -s_{12}c_{23} - c_{12}s_{23}s_{13}e^{i\delta} & c_{12}c_{23} - s_{12}s_{23}s_{13}e^{i\delta} & s_{23}c_{13} \\ s_{12}s_{23} - c_{12}c_{23}s_{13}e^{i\delta} & -c_{12}s_{23} - s_{12}c_{23}s_{13}e^{i\delta} & c_{23}c_{13} \end{pmatrix}, \tag{2.28}$$

with $c_{ij} = \cos(\theta_{ij})$, $s_{ij} = \sin(\theta_{ij})$, where we consider $\theta_{ij} \in [0, \frac{\pi}{2}]$ and $\delta \in [0, 2\pi]$ without loss of generality.

The absence of RH neutrinos in the SM has another consequence: lepton CC do not present lepton mixing. This stems from the freedom of performing the rotation $\nu_L \rightarrow U_L^l \nu_L$, since there are no mass terms for neutrinos. In turn, this leads to the conservation of family lepton number, whereas only the total baryon number is conserved due to the existence of quark mixing.

2.3 Cabibbo angle anomaly

The SM provides a theoretical framework that explains the EW interactions among elementary particles from four independent variables, two from the set $A_{\text{gauge}} = \{g; g'; e; \cos\theta_w\}$ and two from $A_{\text{Higgs}} = \{\mu; \lambda; v\}$, except the CCs for quarks $\mathcal{L}_{\text{CC}}^{\text{quark}}$ and the interactions between the Higgs field Φ and fermions, which depend on \mathbf{V}_{CKM} and the fermion masses, respectively. Furthermore, the SM predicts the massless photon and the relation $m_W = \cos\theta_w m_Z$, which has been repeatedly corroborated by experiment [71].

Although the SM does predict that \mathbf{V}_{CKM} is unitarity, it is not predictive regarding the fermion masses hierarchies and \mathbf{V}_{CKM} mixing structure. Namely, the Yukawa matrices $\mathbf{Y}_{l,d,u}$ in Eq. (2.22), which may be written in a WB where \mathbf{Y}_l and \mathbf{Y}_u are diagonal and \mathbf{Y}_d is hermitian, contain 13 physical parameters [33]. These parameters are responsible for 13 experimental observations (9 fermion masses, 3 mixing angles and a CP violating phase). Nonetheless, there is a strong mass hierarchy among the 3

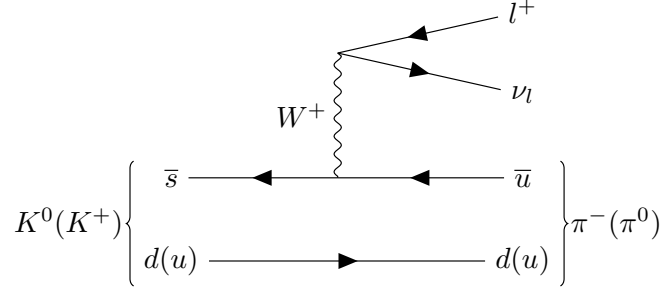


Figure 2.1: Semileptonic $Kl3$ decay tree-level diagram. The quark q corresponds to a $d(u)$ quark when representing the decay of a $K^0(K^+)$ meson into a $\pi^-(\pi^0)$ meson, respectively.

different generations of fermions, spanning over a range of 6 orders of magnitude [37]. Besides this, by examining the independent measurements of the moduli of \mathbf{V}_{CKM} entries [37]

$$|\mathbf{V}_{\text{CKM}}| = \begin{pmatrix} 0.97373 \pm 0.00031 & 0.2243 \pm 0.0008 & 0.00382 \pm 0.00020 \\ 0.221 \pm 0.004 & 0.975 \pm 0.006 & 0.0408 \pm 0.0014 \\ 0.0086 \pm 0.0002 & 0.0415 \pm 0.0009 & 1.014 \pm 0.029 \end{pmatrix}, \quad (2.29)$$

we observe that \mathbf{V}_{CKM} also exhibits a very clear structure, close to the identity matrix with small off-diagonal mixing among up and down quark flavours of different generations. This discrepancy between the arbitrariness of the Yukawa coupling constants and the resulting hierarchy observed in fermion masses and quark mixing is known as the *flavour puzzle*, and it has been hypothesised that there may be a BSM mechanism that generates these patterns. This suspicion has been further motivated by recent improvements on the experimental determination and theoretical uncertainties regarding the elements of the first row of \mathbf{V}_{CKM} :

$$|(\mathbf{V}_{\text{CKM}})_{ud}|^2 + |(\mathbf{V}_{\text{CKM}})_{us}|^2 + |(\mathbf{V}_{\text{CKM}})_{ub}|^2 = 0.9985 \pm 0.0007 < 1, \quad (2.30)$$

which exhibit a deficit in the unitarity condition. Since $|(\mathbf{V}_{\text{CKM}})_{ub}| = 0.00382$ is much smaller compared to $|(\mathbf{V}_{\text{CKM}})_{ud}|$ and $|(\mathbf{V}_{\text{CKM}})_{us}|$, its contribution to Eq. (2.30) is negligible, and the analysis of this condition reduces to determining the Cabibbo angle θ_C that parameterises $|(\mathbf{V}_{\text{CKM}})_{ud}| = \cos \theta_C$ and $|(\mathbf{V}_{\text{CKM}})_{us}| = \sin \theta_C$. Hence, the deviation from unitarity δ_{CKM} in the first row of \mathbf{V}_{CKM} , defined as

$$\delta_{\text{CKM}} \equiv 1 - |(\mathbf{V}_{\text{CKM}})_{ud}|^2 - |(\mathbf{V}_{\text{CKM}})_{us}|^2, \quad (2.31)$$

is commonly known as the Cabibbo angle anomaly (CAA).

We now present a more detailed review on the experimental status of the CAA based on [10, 16, 32]. The element $|(\mathbf{V}_{\text{CKM}})_{us}|$ is measured directly from semileptonic $Kl3$ decays, represented in Fig. 2.1, through the relation [72]:

$$f_+(0)|(\mathbf{V}_{\text{CKM}})_{us}| = 0.21634(38), \quad (2.32)$$

where $f_+(0)$ is the vector form factor at zero momentum transfer. Using the 2021 FLAG $f_+(0) =$

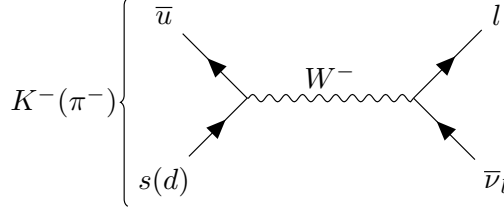


Figure 2.2: $K^-(\pi^-)$ leptonic decay diagram for $q = s(d)$.

0.9698(17) [73], we determine the value of $|(\mathbf{V}_{\text{CKM}})_{us}|$:

$$\text{A : } |(\mathbf{V}_{\text{CKM}})_{us}| = 0.2231(6). \quad (2.33)$$

It is also possible to probe the ratio $|(\mathbf{V}_{\text{CKM}})_{us}/(\mathbf{V}_{\text{CKM}})_{ud}|$ experimentally by computing the ratio of the radiative inclusive kaon and pion leptonic decay rates $K^+ \rightarrow \mu^+ \nu(\gamma)$ and $\pi^+ \rightarrow \mu^+ \nu(\gamma)$ [37]:

$$|(\mathbf{V}_{\text{CKM}})_{us}/(\mathbf{V}_{\text{CKM}})_{ud}| \times (f_{K^\pm}/f_{\pi^\pm}) = 0.27600(37). \quad (2.34)$$

Using the value $f_{K^\pm}/f_{\pi^\pm} = 1.1932(21)$ [73] we get:

$$\text{B : } |(\mathbf{V}_{\text{CKM}})_{us}/(\mathbf{V}_{\text{CKM}})_{ud}| = 0.2313(5). \quad (2.35)$$

The most precise determination of $|(\mathbf{V}_{\text{CKM}})_{ud}|$ is obtained from the analysis of superallowed $0^+ - 0^+$ nuclear β -decays. These pure Fermi transitions, which are only sensitive to the vector coupling constant for semi-leptonic weak interactions $G_V = G_F |(\mathbf{V}_{\text{CKM}})_{ud}|$, allows one to establish the relation [74, 75]:

$$|(\mathbf{V}_{\text{CKM}})_{ud}|^2 = \frac{K}{2G_F^2 Ft(1 + \Delta_R)} = \frac{0.97142(58)}{1 + \Delta_R}, \quad (2.36)$$

where $K/(\hbar c)^6 = 2\pi^3 \ln 2 \hbar / (m_e c^2)^5 = 8120.2762(3) \times 10^{-10} \text{ s/GeV}^4$, $G_F = G_\mu = 1.1663788(6) \times 10^{-5} \text{ GeV}^{-2}$ [37] and $Ft = 3072.24(1.85) \text{ s}$ is the nucleus independent value determined from the average of the 15 most precise superallowed $0^+ - 0^+$ nuclear β -decays [75]. The reduction of hadronic uncertainties allowed the recalculation of $\Delta_R = 0.02361(38)$ [76] computed in 2006. We shall consider the recently computed $\Delta_R = 0.02467(22)$ [9] in Eq. (2.36), yielding the result:

$$0^+ - 0^+ : |(\mathbf{V}_{\text{CKM}})_{ud}| = 0.97367(31). \quad (2.37)$$

We can also determine the value of $|(\mathbf{V}_{\text{CKM}})_{ud}|$ from free neutron β -decays:

$$|(\mathbf{V}_{\text{CKM}})_{ud}|^2 = \frac{K/\ln 2}{G_F^2 F_n \tau_n (1 + 3g_A^2)(1 + \Delta_R)} = \frac{5024.5(6) \text{ s}}{\tau_n (1 + 3g_A^2)(1 + \Delta_R)}, \quad (2.38)$$

where $F_n = f_n(1 + \delta_R)$ is the neutron f -value $f_n = 1.6887(2)$ corrected by the long-distance QED correction $\delta_R = 0.014902(2)$ [77]. Employing in Eq. (2.38) the PDG value $g_A = -1.2754(13)$, the neutron

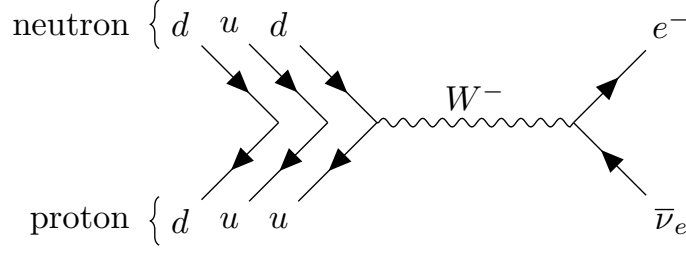


Figure 2.3: Superallowed $0^+ - 0^+$ nuclear and free neutron β -decays diagram.

lifetime $\tau_n = 878.4(5)$ s [37] and Δ_R , we obtain:

$$\text{neutron: } |(\mathbf{V}_{\text{CKM}})_{ud}| = 0.9744(9). \quad (2.39)$$

Taking the average of these results, following the procedure employed in [37], we get:

$$\text{C : } |(\mathbf{V}_{\text{CKM}})_{ud}| = 0.9737(3). \quad (2.40)$$

We perform a fit of $|(\mathbf{V}_{\text{CKM}})_{us}|$ and $|(\mathbf{V}_{\text{CKM}})_{ud}|$, which are considered independent variables, i.e. with no unitarity imposed, to the values of Eqs. (2.40), (2.33) and (2.35). This fit is presented in Fig. 2.4. The best fit point, represented by the green cross, is given by $|(\mathbf{V}_{\text{CKM}})_{us}| = 0.2242$ and $|(\mathbf{V}_{\text{CKM}})_{ud}| = 0.9737$ and corresponds to the minimum $\chi_{\text{bfp}}^2 = 8.0$. The green contours delimit the $\Delta\chi_{\text{non-uni.}}^2 = 2.3, = 6.18, = 11.83$ regions, where $\Delta\chi_{\text{non-uni.}}^2 = \chi^2(|(\mathbf{V}_{\text{CKM}})_{ud}|, |(\mathbf{V}_{\text{CKM}})_{us}|) - \chi_{\text{bfp}}^2$. The black line corresponds to the unitarity of the first line of \mathbf{V}_{CKM} . There is clearly a tension between the unitarity of \mathbf{V}_{CKM} and the best fit value, which stand $\approx \chi_{\text{bfp}}^2 + 6.18$ away. The best fit point leads to $\delta_{\text{CKM}} = 1.7 \times 10^{-3}$. Another approach to the analysis of this discrepancy is determining either $|(\mathbf{V}_{\text{CKM}})_{ud}|$ or $|(\mathbf{V}_{\text{CKM}})_{us}|$ assuming unitarity of \mathbf{V}_{CKM} . Choosing $|(\mathbf{V}_{\text{CKM}})_{us}|$, we obtain:

$$\text{A : } |(\mathbf{V}_{\text{CKM}})_{us}| = 0.2231(6), \quad \text{B : } |(\mathbf{V}_{\text{CKM}})_{us}| = 0.2254(5), \quad \text{C : } |(\mathbf{V}_{\text{CKM}})_{us}| = 0.2276(13), \quad (2.41)$$

which correspond to the vertical bars plotted in Fig. 2.4.

There have been several proposals to address the CAA [12, 13, 15, 18–20, 23–26, 30, 33, 78–82], which are subdivided into two different interpretations: either the first row of \mathbf{V}_{CKM} truly violates unitarity or the experimental determination of $|(\mathbf{V}_{\text{CKM}})_{ud}|$ and $|(\mathbf{V}_{\text{CKM}})_{us}|$ is plagued by some NP phenomena. The first approach would correspond to the translation of the black curve in Fig. 2.4 by δ_{CKM} . This is usually achieved by introducing heavy quarks to the SM particle content, leading to an extended \mathbf{V}_{CKM} . For example, extending the SM with one generation of SM-like quarks would result in a 4×4 quark mixing matrix \mathbf{V}' , leading to the unitarity relation:

$$|(\mathbf{V}_{\text{CKM}})_{ud}|^2 + |(\mathbf{V}_{\text{CKM}})_{us}|^2 + |(\mathbf{V}_{\text{CKM}})_{ub}|^2 + |(\mathbf{V}')_{ub'}|^2 = 1, \quad (2.42)$$

where b' corresponds to the introduced down-type quark. In this scenario, the currently observed deviation from unitarity would lead to $|(\mathbf{V}_{\text{CKM}})_{ub'}| = \sqrt{\delta_{\text{CKM}}} \approx 4.1 \times 10^{-2}$. On the other hand, the second approach

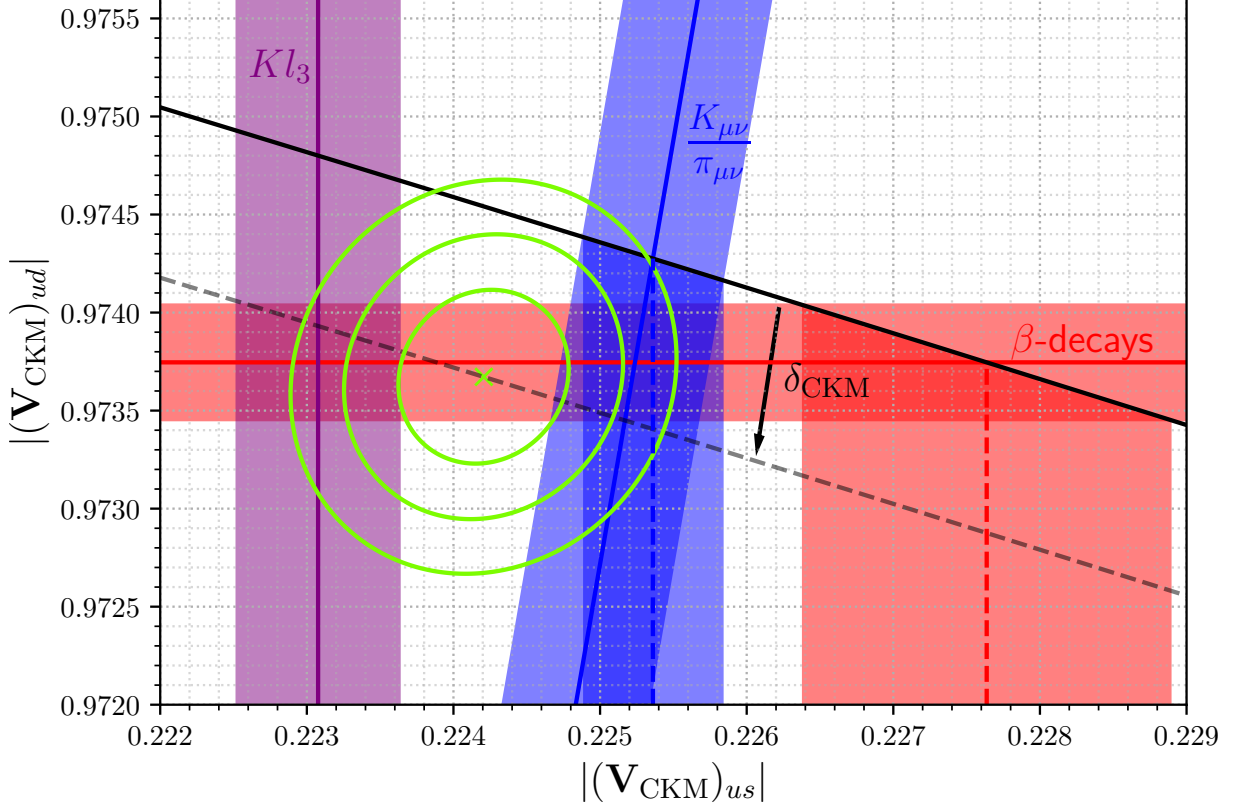


Figure 2.4: The values of $|(\mathbf{V}_{\text{CKM}})_{us}|$ from Eq. (2.33), $|(\mathbf{V}_{\text{CKM}})_{ud}|$ from Eq. (2.40) and $|(\mathbf{V}_{\text{CKM}})_{us}/(\mathbf{V}_{\text{CKM}})_{ud}|$ from Eq. (2.35) correspond to the purple, red and blue regions. The green cross represents the best fit point (bfp). The green curves delimit the 1σ , 2σ and 3σ contours, which correspond to $\Delta\chi^2_{\text{non-uni.}} = 2.3; 6.18; 11.83$. The black curve is obtained from the unitarity constraint of the first row of \mathbf{V}_{CKM} . The dashed black curve corresponds to the unitarity constraint corrected by δ_{CKM} .

consists of modifying the values of $|(\mathbf{V}_{\text{CKM}})_{us}|$ and $|(\mathbf{V}_{\text{CKM}})_{ud}|$ such that the χ^2 of the fit improves. An example of this solution is given in [10], where it is assumed that the Fermi constant G_F is different from the effective constant G_μ determined from the muon lifetime. In the low energy limit (energies much smaller than m_W), the effective interaction responsible for the muon decay is:

$$-\frac{4G_F}{\sqrt{2}}(\bar{e}_L\gamma^\mu\nu_e)(\bar{\nu}_\mu\gamma_\mu\mu_L). \quad (2.43)$$

By introducing a lepton flavour changing neutral gauge boson W' that results in the operator:

$$-\frac{4G_{F'}}{\sqrt{2}}(\bar{e}_L\gamma^\mu\mu_e)(\bar{\nu}_\mu\gamma_\mu\mu_L), \quad (2.44)$$

the constant G_μ determined by the muon decay is modified to $G_\mu = G_F + G_{F'} = G_F(1 + \delta_\mu)$. This would, in turn, result in deviations for $|(\mathbf{V}_{\text{CKM}})_{ud}|$ and $|(\mathbf{V}_{\text{CKM}})_{us}|$:

$$|(\mathbf{V}_{\text{CKM}})_{ud}| = 0.97362(26) \times (1 + \delta_\mu), \quad |(\mathbf{V}_{\text{CKM}})_{us}| = 0.22326(55) \times (1 + \delta_\mu), \quad (2.45)$$

while their ratio remains unaffected. There exists several other models based on lepton flavor universality violation that address the CAA [12, 19, 20, 23, 24, 78, 80, 83].

Chapter 3

Standard Model extensions with isosinglet vector-like quarks

As stated in the previous chapter, a possible solution to the CAA is extending the quark content of the SM. However, the possibility for a fourth generation of chiral quarks has already been ruled out not only by measurements of Higgs-mediated cross sections, combined with direct searches at the LHC [84, 85], but also by EW precision observables [86].

Vector-like quarks (VLQs) are coloured fermions, i.e. triplets under $SU(3)_c$, whose LH and RH components are in the same representation under G_{SM} . Extending the SM with VLQs is compatible with Higgs data since these particles do not obtain mass via the typical Yukawa couplings to the Higgs doublet. Furthermore, VLQs automatically preserve gauge anomaly¹ cancelation [87–89]. In Table 3.1 we present the seven possible VLQ representations under G_{SM} that can mix with SM quarks, assuming a scalar sector comprised of only $SU(2)_L$ scalar doublets [90]. Hereinafter, we discuss exclusively the extension of the SM with isosinglet VLQs.

3.1 Mass Lagrangian

Consider an extension of the SM featuring n_B down-type and n_T up-type singlet VLQs denoted $B_{L,R}$ and $T_{L,R}$, respectively. Since this model leaves the leptonic sector unchanged, we constrain our analysis to the quark sector. In this general framework, the Yukawa Lagrangian in the flavour basis is written as

$$-\mathcal{L}_{\text{Yuk.}} = -\mathcal{L}_{\text{Yuk.}}^{\text{SM}} + \overline{q}_{Li}(\mathbf{Y}_{dB})_{ij}\Phi B_{Rj} + \overline{q}_{Li}(\mathbf{Y}_{uT})_{ik}\tilde{\Phi}T_{Rk} + \text{H.c.} , \quad (3.1)$$

where \mathbf{Y}_{dB} and \mathbf{Y}_{uT} are $3 \times n_B$ and $3 \times n_T$ Yukawa matrices, respectively, and $\mathcal{L}_{\text{Yuk.}}^{\text{SM}}$ stands for the Lagrangian in Eq. (2.22). Furthermore, contrary to the SM chiral quarks, VLQs introduce bare mass terms, since, as stated before, both LH and RH components are under the same G_{SM} representation.

¹Gauge anomalies occur when a local gauge symmetry is conserved at the classical level but violated at the quantum (one-loop) level, spoiling the theory's renormalisability.

Multiplet	T	B	$\begin{pmatrix} T \\ B \end{pmatrix}$	$\begin{pmatrix} X \\ T \end{pmatrix}$	$\begin{pmatrix} B \\ Y \end{pmatrix}$	$\begin{pmatrix} X \\ T \\ B \end{pmatrix}$	$\begin{pmatrix} T \\ B \\ Y \end{pmatrix}$
T_3	0	0	$\frac{1}{2}$	$\frac{1}{2}$	$\frac{1}{2}$	1	1
Y	$\frac{4}{3}$	$-\frac{2}{3}$	$\frac{1}{3}$	$\frac{7}{3}$	$-\frac{5}{3}$	$\frac{4}{3}$	$-\frac{2}{3}$

Table 3.1: Possible VLQ representations under G_{SM} that can mix with SM quarks via Yukawa couplings, assuming a scalar sector comprised of only $\text{SU}(2)_L$ scalar doublets.

Recalling the definitions in Eq. (2.11) we obtain

$$-\mathcal{L}_{\text{b.m.}} = \overline{B}_L \mathbf{M}_{Bd} d_R + \overline{B}_L \mathbf{M}_B B_R + \overline{T}_L \mathbf{M}_{Tu} u_R + \overline{T}_L \mathbf{M}_T T_R + \text{H.c.} , \quad (3.2)$$

where $\mathbf{M}_{Bd,Tu}$ and $\mathbf{M}_{B,T}$ are $n_{B,T} \times 3$ and $n_{B,T} \times n_{B,T}$ mass matrices, respectively. After EWSB, defining the weak eigenstate vectors $D_{L,R} = (d, B)_{L,R}^T$ and $U_{L,R} = (u, T)_{L,R}^T$, of dimensions $n_d = 3 + n_B$ and $n_u = 3 + n_T$, respectively, we can write the mass Lagrangian in the compact form,

$$-\mathcal{L}_{\text{mass}} = \overline{D}_L \mathcal{M}_d D_R + \overline{U}_L \mathcal{M}_u U_R + \text{H.c.} , \quad (3.3)$$

where

$$\mathcal{M}_d = \begin{pmatrix} \mathbf{M}_d & \mathbf{M}_{dB} \\ \mathbf{M}_{Bd} & \mathbf{M}_B \end{pmatrix} , \quad \mathcal{M}_u = \begin{pmatrix} \mathbf{M}_u & \mathbf{M}_{uT} \\ \mathbf{M}_{Tu} & \mathbf{M}_T \end{pmatrix} , \quad \mathbf{M}_{dB} = \frac{v}{\sqrt{2}} \mathbf{Y}_{dB} , \quad \mathbf{M}_{uT} = \frac{v}{\sqrt{2}} \mathbf{Y}_{uT} , \quad (3.4)$$

and $\mathbf{M}_{d,u}$ are defined in Eq. (2.23). The matrices $\mathcal{M}_{d,u}$ are bidiagonalised via the unitary transformations $D_{L,R} \rightarrow \mathcal{V}_{L,R}^d D_{L,R}$ and $U_{L,R} \rightarrow \mathcal{V}_{L,R}^u U_{L,R}$ such that,

$$\begin{aligned} \mathcal{V}_L^{d\dagger} \mathcal{M}_d \mathcal{V}_R^d &= \mathcal{D}_d = \text{diag}(m_d, m_s, m_b, m_{B_1}, \dots, m_{B_{n_B}}) , \\ \mathcal{V}_L^{u\dagger} \mathcal{M}_u \mathcal{V}_R^u &= \mathcal{D}_u = \text{diag}(m_u, m_c, m_t, m_{T_1}, \dots, m_{T_{n_T}}) , \end{aligned} \quad (3.5)$$

where $m_{d,s,b}$ and $m_{u,c,t}$ are the physical SM down and up quark masses, while $m_{B,T}$ are the real and positive heavy quark masses. The above unitary matrices are obtained by bidiagonalising the Hermitian matrices $\mathcal{H}_{d,u} = \mathcal{M}_{d,u} \mathcal{M}_{d,u}^\dagger$ and $\mathcal{H}'_{d,u} = \mathcal{M}_{d,u}^\dagger \mathcal{M}_{d,u}$, as follows,

$$\begin{aligned} \mathcal{V}_L^{d\dagger} \mathcal{H}_d \mathcal{V}_L^d &= \mathcal{V}_R^{d\dagger} \mathcal{H}'_d \mathcal{V}_R^d = \mathcal{D}_d^2 , \\ \mathcal{V}_L^{u\dagger} \mathcal{H}_u \mathcal{V}_L^u &= \mathcal{V}_R^{u\dagger} \mathcal{H}'_u \mathcal{V}_R^u = \mathcal{D}_u^2 . \end{aligned} \quad (3.6)$$

It is useful to write \mathcal{V} in terms of the $3 \times n_{d,u}$ and $n_{B,T} \times n_{d,u}$ matrices, respectively denoted \mathbf{A} and \mathbf{B} ,

$$\mathcal{V}_{L,R}^{d,u} = \begin{pmatrix} \mathbf{A}_{L,R}^{d,u} \\ \mathbf{B}_{L,R}^{d,u} \end{pmatrix} \Rightarrow \begin{cases} d_{L,R} = \mathbf{A}_{L,R}^d D_{L,R}^m \\ u_{L,R} = \mathbf{A}_{L,R}^u U_{L,R}^m \end{cases} , \quad \begin{cases} B_{L,R} = \mathbf{B}_{L,R}^d D_{L,R}^m \\ T_{L,R} = \mathbf{B}_{L,R}^u U_{L,R}^m \end{cases} . \quad (3.7)$$

with $U_{L,R}^m = (u, c, t, T_1^m, \dots, T_{n_T}^m)$ and $D_{L,R}^m = (d, s, b, B_1^m, \dots, B_{n_B}^m)$ the quark vectors in the physical basis.

From the unitarity of \mathbf{V} we extract the following identities:

$$\mathbf{V}^\dagger \mathbf{V} = \mathbb{1}_{n_{d,u} \times n_{d,u}} \Rightarrow \mathbf{A}^\dagger \mathbf{A} + \mathbf{B}^\dagger \mathbf{B} = \mathbb{1}_{n_{d,u} \times n_{d,u}}, \quad (3.8)$$

$$\mathbf{V} \mathbf{V}^\dagger = \mathbb{1}_{n_{d,u} \times n_{d,u}} \Rightarrow \mathbf{A} \mathbf{A}^\dagger = \mathbb{1}_{3 \times 3}, \quad \mathbf{B} \mathbf{B}^\dagger = \mathbb{1}_{n_{B,T} \times n_{B,T}}, \quad \mathbf{A} \mathbf{B}^\dagger = \mathbb{0}_{3 \times n_{B,T}}, \quad \mathbf{B} \mathbf{A}^\dagger = \mathbb{0}_{n_{B,T} \times 3}. \quad (3.9)$$

3.2 Charged and neutral currents

The isosinglet VLQs, which are invariant under $SU(2)_L$, do not couple to the gauge bosons W^\pm . Thus, the quark CCs remain unchanged in the weak eigenstate basis [Eq. (2.14)]. Analogously to the SM case, when we rotate the quark fields to the physical basis a quark mixing matrix \mathbf{V} appears,

$$\mathcal{L}_{W^\pm} = \frac{g}{\sqrt{2}} W_\mu^\pm \sum_{i=1}^{n_u} \sum_{j=1}^{n_d} \mathbf{V}_{ij} \bar{U}_i^m \gamma^\mu P_L D_j^m + \text{H.c.}, \quad (3.10)$$

where $n_u = n_T + 3$, $n_d = n_B + 3$ and

$$\mathbf{V} = \mathbf{A}_L^{u\dagger} \mathbf{A}_L^d = \left(\begin{array}{c|c} (\mathbf{V}_{\text{CKM}})_{3 \times 3} & (\mathbf{V}_B)_{3 \times n_B} \\ \hline (\mathbf{V}_T)_{n_T \times 3} & (\mathbf{V}_{TB})_{n_T \times n_B} \end{array} \right). \quad (3.11)$$

The $n_u \times n_d$ complex matrix \mathbf{V} is not necessarily unitary, contrary to the SM case. The matrices \mathbf{V}_B (\mathbf{V}_T) encode the strength of the charged interactions between the SM up(down)-type quarks and the down(up)-type VLQs, while the matrix \mathbf{V}_{TB} concerns the interactions between VLQs. It is possible to parameterise a general \mathbf{V} matrix with mixing angles and complex phases, similarly to the PDG parameterisation of \mathbf{V}_{CKM} , using the Botella-Chau parameterisation [91], see e.g. Refs. [17, 28, 33].

The NCs in the WB are given by

$$\mathcal{L}_A^{\text{NC}} = e \left(-\frac{2}{3} \bar{U} \gamma_\mu U + \frac{1}{3} \bar{D} \gamma_\mu D \right) A^\mu, \quad (3.12)$$

$$\mathcal{L}_Z^{\text{NC}} = \frac{g}{\cos \theta_w} \left[\sin^2 \theta_w \left(-\frac{2}{3} \bar{U} \gamma_\mu U + \frac{1}{3} \bar{D} \gamma_\mu D \right) + \frac{1}{2} (\bar{u}_L \gamma_\mu u_L - \bar{d}_L \gamma_\mu d_L) \right] Z^\mu, \quad (3.13)$$

where the VLQs being isosinglets only contribute to the RH currents. From Eqs. (3.7) and (3.9), we deduce the following identities:

$$\begin{aligned} \bar{d}_L \gamma_\mu d_L &= \bar{D}_L^m \gamma_\mu (\mathbf{A}_L^d)^\dagger \mathbf{A}_L^d D_L^m = \bar{D}_L^m \gamma_\mu \mathbf{V}^\dagger \mathbf{V} D^m = \bar{D}_L^m \gamma_\mu \mathbf{F}^d D^m, \\ \bar{u}_L \gamma_\mu u_L &= \bar{U}_L^m \gamma_\mu (\mathbf{A}_L^u)^\dagger \mathbf{A}_L^u U_L^m = \bar{U}_L^m \gamma_\mu \mathbf{V} \mathbf{V}^\dagger U_L^m = \bar{U}_L^m \gamma_\mu \mathbf{F}^u U_L^m, \end{aligned} \quad (3.14)$$

leading to

$$\mathcal{L}_A^{\text{NC}} = e \left(-\frac{2}{3} \sum_{i=1}^{n_u} \bar{U}_i^m \gamma_\mu U_i^m + \sum_{i=1}^{n_d} \frac{1}{3} \bar{D}_i^m \gamma_\mu D_i^m \right) A^\mu, \quad (3.15)$$

$$\mathcal{L}_Z^{\text{NC}} = \frac{g}{c_W} Z_\mu \left[\sum_{i,j=1}^{n_u} \overline{U}_i^m \left(\frac{1}{2} \mathbf{F}_{ij}^u P_L - \frac{2}{3} s_W^2 \delta_{ij} \right) \gamma^\mu U_j^m - \sum_{i,j=1}^{n_d} \overline{D}_i^m \left(\frac{1}{2} \mathbf{F}_{ij}^d P_L - \frac{1}{3} s_W^2 \delta_{ij} \right) \gamma^\mu D_j^m \right]. \quad (3.16)$$

The interaction terms between the quarks and the Higgs bosons, considering the parameterisation in Eq. (2.20), in the WB are

$$\begin{aligned} -\mathcal{L}_{\text{Higgs}}^{\text{NC}} &= \overline{u}_L \begin{pmatrix} \mathbf{Y}_d & \mathbf{Y}_{dB} \end{pmatrix} D_R G^+ + \overline{d}_L \begin{pmatrix} \mathbf{Y}_u & \mathbf{Y}_{uT} \end{pmatrix} U_R G^- \\ &+ \frac{1}{\sqrt{2}} \left[\overline{d}_L \begin{pmatrix} \mathbf{Y}_d & \mathbf{Y}_{dB} \end{pmatrix} D_R + \overline{u}_L \begin{pmatrix} \mathbf{Y}_u & \mathbf{Y}_{uT} \end{pmatrix} U_R \right] H \\ &+ \frac{i}{\sqrt{2}} \left[\overline{d}_L \begin{pmatrix} \mathbf{Y}_d & \mathbf{Y}_{dB} \end{pmatrix} D_R - \overline{u}_L \begin{pmatrix} \mathbf{Y}_u & \mathbf{Y}_{uT} \end{pmatrix} U_R \right] G^0 + \text{H.c.} . \end{aligned} \quad (3.17)$$

After EWSB, we derive from Eqs. (3.6) and (3.7) the following relations:

$$\begin{pmatrix} \mathbf{Y}_u & \mathbf{Y}_{uT} \end{pmatrix} = \frac{\sqrt{2}}{v} \mathbf{A}_L^u \mathcal{D}_u \mathcal{V}_R^{u\dagger}, \quad \begin{pmatrix} \mathbf{Y}_d & \mathbf{Y}_{dB} \end{pmatrix} = \frac{\sqrt{2}}{v} \mathbf{A}_L^d \mathcal{D}_d \mathcal{V}_R^{d\dagger}, \quad (3.18)$$

allowing to finally write the quark-Higgs interactions in the physical basis as

$$\begin{aligned} -\mathcal{L}_{\text{Higgs}}^{\text{NC}} &= \frac{\sqrt{2}}{v} \overline{U}_L^m \mathbf{V} \mathcal{D}_d D_R^m G^+ + \frac{\sqrt{2}}{v} \overline{D}_L^m \mathbf{V}^\dagger \mathcal{D}_u U_R^m G^- \\ &+ \frac{1}{v} \left(\overline{D}_L^m \mathbf{F}^d \mathcal{D}_d D_R^m + \overline{U}_L^m \mathbf{F}^u \mathcal{D}_u U_R^m \right) H \\ &+ \frac{i}{v} \left(\overline{D}_L^m \mathbf{F}^d \mathcal{D}_d D_R^m - \overline{U}_L^m \mathbf{F}^u \mathcal{D}_u U_R^m \right) G^0 + \text{H.c.} . \end{aligned} \quad (3.19)$$

Despite SM extensions with VLQs presenting a possible solution to the CAA via the non-unitary \mathbf{V} , these also result in new interactions, such as tree-level FCNC mediated by the Z and Higgs bosons [see Eqs. (3.16) and (3.19), respectively], which violate the GIM mechanism [34]. In 1969, when the GIM mechanism was proposed, only the up, down and strange quarks were known. In order to explain the strict experimental bounds of strangeness changing neutral-current processes, generated at 1 loop, the GIM mechanism predicted the existence of the charm quark, requiring the existence of two generations of quark $\text{SU}(2)_L$ doublets. Following the discussion in Section 2.2.1, it is straightforward to conclude that this mechanism predicts a 2×2 orthogonal \mathbf{V}_{CKM} , parameterised by a single mixing angle. The orthogonality of \mathbf{V}_{CKM} would then result in a natural suppression of one-loop FCNC processes. Hence, BSM scenarios involving the introduction of VLQs must pay careful attention to phenomenological constraints regarding FCNC mediated processes.

3.3 Relation between CKM non-unitarity and flavour changing neutral currents

In this section we investigate the relation between \mathbf{V}_{CKM} non-unitarity and the strength of FCNC encoded in the matrices $\mathbf{F}^{u,d}$. Hereinafter, the superscripts and subscripts are omitted whenever possible

for the sake of simplicity. We begin by parameterising the rotation matrices in Eq. (3.7) as

$$\mathbf{v} = \begin{pmatrix} \mathbf{K}_{3 \times 3} & \mathbb{0}_{3 \times n} \\ \mathbb{0}_{n \times 3} & \bar{\mathbf{K}}_{n \times n} \end{pmatrix} \begin{pmatrix} \mathbb{1}_{3 \times 3} & \mathbf{X}_{3 \times n} \\ -\mathbf{X}_{n \times 3}^\dagger & \mathbb{1}_{n \times n} \end{pmatrix} = \begin{pmatrix} \mathbf{K} & \mathbf{K}\mathbf{X} \\ -\bar{\mathbf{K}}\mathbf{X}^\dagger & \bar{\mathbf{K}} \end{pmatrix}. \quad (3.20)$$

where $n = n_T(n_B)$ for the case of up (down) VLQs. This parameterisation of unitary matrices, originally presented within the context of a seesaw type-I [92, 93], is completely general as long as \mathbf{K} and $\bar{\mathbf{K}}$ are non-singular matrices. Using this relation, we obtain from Eq. (3.11)

$$\mathbf{V} = \begin{pmatrix} \mathbf{K}_L^{u\dagger} \mathbf{K}_L^d & \mathbf{K}_L^{u\dagger} \mathbf{K}_L^d \mathbf{X}_L^d \\ \mathbf{X}_L^{u\dagger} \mathbf{K}_L^{u\dagger} \mathbf{K}_L^d & \mathbf{X}_L^{u\dagger} \mathbf{K}_L^{u\dagger} \mathbf{K}_L^d \mathbf{X}_L^d \end{pmatrix} = \begin{pmatrix} \mathbf{V}_{\text{CKM}} & \mathbf{V}_{\text{CKM}} \mathbf{X}_L^d \\ \mathbf{X}_L^{u\dagger} \mathbf{V}_{\text{CKM}} & \mathbf{X}_L^{u\dagger} \mathbf{V}_{\text{CKM}} \mathbf{X}_L^d \end{pmatrix}. \quad (3.21)$$

The matrices $\mathbf{F}^{u,d}$ defined in Eq. (3.14) that mediate FCNC are given by

$$\mathbf{F} = \mathbf{A}_L^\dagger \mathbf{A}_L = \begin{pmatrix} \mathbf{K}_L^\dagger \mathbf{K}_L & \mathbf{K}_L^\dagger \mathbf{K}_L \mathbf{X}_L \\ \mathbf{X}_L^\dagger \mathbf{K}_L^\dagger \mathbf{K}_L & \mathbf{X}_L^\dagger \mathbf{K}_L^\dagger \mathbf{K}_L \mathbf{X}_L \end{pmatrix}. \quad (3.22)$$

By inspection of the previous equations, we infer that the matrices $\mathbf{X}_L^{u,d}$ may encode the deviation from unitarity of \mathbf{V}_{CKM} , which is intimately connected with the magnitude of FCNC. In the limit $\mathbf{X} \rightarrow \mathbb{0}$, the matrices \mathbf{K} and $\bar{\mathbf{K}}$ must be unitary for Eq. (3.20) to hold, which in turn leads to

$$\mathbf{V} \xrightarrow{\mathbf{X} \rightarrow \mathbb{0}} \begin{pmatrix} \mathbf{V}_{\text{CKM}} & \mathbb{0} \\ \mathbb{0} & \mathbb{0} \end{pmatrix}, \quad \mathbf{F} \xrightarrow{\mathbf{X} \rightarrow \mathbb{0}} \begin{pmatrix} \mathbb{1} & \mathbb{0} \\ \mathbb{0} & \mathbb{0} \end{pmatrix}, \quad (3.23)$$

resulting in a unitary CKM matrix and the absence of FCNC. In fact, this limit corresponds to a total decoupling between SM quarks and VLQs, i.e. these particles do not mix. The relation between a non-zero \mathbf{X} and the non-unitarity of \mathbf{V}_{CKM} is more explicit by noting that the unitarity of \mathbf{V} implies:

$$\mathbf{v}\mathbf{v}^\dagger = \mathbb{1} \implies \begin{cases} \mathbf{K} (\mathbb{1}_{3 \times 3} + \mathbf{X}\mathbf{X}^\dagger) \mathbf{K}^\dagger = \mathbb{1}_{3 \times 3} \\ \bar{\mathbf{K}} (\mathbb{1}_{n \times n} + \mathbf{X}^\dagger \mathbf{X}) \bar{\mathbf{K}}^\dagger = \mathbb{1}_{n \times n} \end{cases} \implies \begin{cases} \mathbf{K} = \mathbf{V}_{\mathbf{K}} (\mathbb{1}_{3 \times 3} + \mathbf{X}\mathbf{X}^\dagger)^{-\frac{1}{2}} \\ \bar{\mathbf{K}} = \mathbf{V}_{\bar{\mathbf{K}}} (\mathbb{1}_{n \times n} + \mathbf{X}^\dagger \mathbf{X})^{-\frac{1}{2}} \end{cases}, \quad (3.24)$$

where $\mathbf{V}_{\mathbf{K} 3 \times 3}$ and $\mathbf{V}_{\bar{\mathbf{K}} n \times n}$ are unitary, and $(\mathbb{1}_{n \times n} + \mathbf{X}^\dagger \mathbf{X})^{-\frac{1}{2}}$ and $(\mathbb{1}_{3 \times 3} + \mathbf{X}\mathbf{X}^\dagger)^{-\frac{1}{2}}$ are hermitian. Substituting these results in Eqs. (3.21) and (3.22), leads to

$$\mathbf{V}_{\text{CKM}} = \left(\mathbb{1}_{3 \times 3} + \mathbf{X}_L^u \mathbf{X}_L^{u\dagger} \right)^{-\frac{1}{2}} \mathbf{V}' \left(\mathbb{1}_{3 \times 3} + \mathbf{X}_L^d \mathbf{X}_L^{d\dagger} \right)^{-\frac{1}{2}}, \quad \mathbf{V}' = \mathbf{V}_{\mathbf{K}_L^u}^\dagger \mathbf{V}_{\mathbf{K}_L^d}, \quad (3.25)$$

$$\mathbf{K}^\dagger \mathbf{K} = (\mathbb{1}_{3 \times 3} + \mathbf{X}\mathbf{X}^\dagger)^{-1}, \quad (3.26)$$

where it is now clear that $\mathbf{X}_L^{u,d}$ are indeed responsible for both deviations from unitarity and the existence of FCNC. For small $\mathbf{X}_L^{u,d}$, by expanding

$$(\mathbb{1}_{3 \times 3} + \mathbf{X}\mathbf{X}^\dagger)^{-\frac{1}{2}} \approx \mathbb{1}_{3 \times 3} - \frac{1}{2} \mathbf{X}\mathbf{X}^\dagger, \quad (\mathbb{1}_{n \times n} + \mathbf{X}^\dagger \mathbf{X})^{-\frac{1}{2}} \approx \mathbb{1}_{n \times n} - \frac{1}{2} \mathbf{X}^\dagger \mathbf{X}, \quad (3.27)$$

we obtain the following expressions for \mathbf{V} and \mathbf{F} ,

$$\mathbf{V} \approx \begin{pmatrix} \mathbf{V}' - \frac{1}{2}\mathbf{X}_L^{u\dagger}\mathbf{X}_L^u\mathbf{V}' - \frac{1}{2}\mathbf{X}_L^{d\dagger}\mathbf{X}_L^d\mathbf{V}' & \mathbf{V}'\mathbf{X}_L^d \\ \mathbf{X}_L^{u\dagger}\mathbf{V}' & \mathbf{X}_L^{u\dagger}\mathbf{V}'\mathbf{X}_L^d \end{pmatrix}, \quad (3.28)$$

$$\mathbf{F} \approx \begin{pmatrix} 1 - \mathbf{X}_L\mathbf{X}_L^\dagger & \mathbf{X}_L \\ \mathbf{X}_L^\dagger & \mathbf{X}_L^\dagger\mathbf{X}_L \end{pmatrix}, \quad (3.29)$$

valid up to $\mathcal{O}(\mathbf{X}^3)$ terms.

Recalling that the mixing matrix \mathbf{V} is in general non-unitary, we define

$$\begin{aligned} \Delta_n^u &= 1 - \sum_{j=1}^{3+n_B} |\mathbf{V}_{nj}|^2 = 1 - \sum_{j=1}^{3+n_B} \mathbf{V}_{nj}(\mathbf{V}^\dagger)_{jn} = 1 - \mathbf{F}_{nn}^u \approx (\mathbf{X}^u\mathbf{X}^{u\dagger})_{nn}, \\ \Delta_n^d &= 1 - \sum_{j=1}^{3+n_T} |\mathbf{V}_{jn}|^2 = 1 - \sum_{j=1}^{3+n_T} (\mathbf{V}^\dagger)_{nj}\mathbf{V}_{jn} = 1 - \mathbf{F}_{nn}^d \approx (\mathbf{X}^d\mathbf{X}^{d\dagger})_{nn}, \end{aligned} \quad (3.30)$$

where Δ_n^u and Δ_n^d measure the deviation from unitarity of the n^{th} row and column of \mathbf{V} , respectively, and the last equality follows from the definitions of $\mathbf{F}^{u,d}$ in Eq. (3.14). However, the calculation of these quantities requires the experimental determination of the mixing elements concerning VLQs, namely the entries \mathbf{V}_{ij} with either i or j larger than 3. In practice, we are currently only able to compute the non-unitarity of \mathbf{V}_{CKM} through direct measurements of its elements moduli. The deviation from unitarity of the rows and columns of \mathbf{V}_{CKM} are given by δ_n^u and δ_n^d , respectively, with

$$\delta_n^u = 1 - \sum_{j=1}^3 |(\mathbf{V}_{\text{CKM}})_{nj}|^2, \quad \delta_n^d = 1 - \sum_{j=1}^3 |(\mathbf{V}_{\text{CKM}})_{jn}|^2. \quad (3.31)$$

From Eq. (3.21), we show that $\Delta_n^{u,d}$ and $\delta_n^{u,d}$ are related through,

$$\begin{aligned} \Delta_n^u - \delta_n^u &= \sum_{j=1}^{n_B} |\mathbf{V}_{n,j+3}|^2 = \sum_{j=1}^{n_B} |(\mathbf{V}_{\text{CKM}}\mathbf{X}_L^d)_{nj}|^2 \approx \sum_{j=1}^{n_B} |(\mathbf{V}'\mathbf{X}_L^d)_{nj}|^2, \\ \Delta_n^d - \delta_n^d &= \sum_{j=1}^{n_T} |\mathbf{V}_{j+3,n}|^2 = \sum_{j=1}^{n_T} |(\mathbf{X}_L^{u\dagger}\mathbf{V}_{\text{CKM}})_{jn}|^2 \approx \sum_{j=1}^{n_T} |(\mathbf{X}_L^{u\dagger}\mathbf{V}')_{jn}|^2. \end{aligned} \quad (3.32)$$

Finally, we discuss two distinct cases, beginning with a SM extension where only up-type VLQs are introduced. In this scenario, there are no FCNCs in the down sector:

$$\mathbf{V}^d = \mathbf{A}^d \implies \mathbf{F}^d = (\mathbf{A}_L^d)^\dagger \mathbf{A}_L^d = \mathbb{1}_{3 \times 3} \stackrel{(3.14)}{\implies} \mathbf{V}^\dagger \mathbf{V} = \mathbb{1}_{3 \times 3} \quad (3.33)$$

This condition states that the columns of $\mathbf{V}_{n_u \times 3}$ are orthonormal ($\Delta_n^d = 0$). However, this is not true for the columns of \mathbf{V}_{CKM} in general (check the structure of \mathbf{V} in Eq. (3.21) for clarity). Orthonormality of a given i^{th} column of \mathbf{V}_{CKM} implies from Eq. (3.32) that $\sum_{j=1}^{n_T} |\mathbf{V}_{j+3,i}|^2 = 0$, i.e. the corresponding SM down quark does not mix with the up-type VLQs.

Regarding the rows of \mathbf{V}_{CKM} , the absence of down type VLQs leads to $\Delta_n^u = \delta_n^u$. Note, however,

that \mathbf{V} is not unitary, and as such the rows of \mathbf{V}_{CKM} , which coincide with the first 3 rows of \mathbf{V} , do not necessarily respect $\delta_n^u = 0$.

A similar reasoning can be applied to the scenario where we extend the SM with only down type VLQs. In this context, the rows of $\mathbf{V}_{3 \times n_d}$ are orthonormal and there are no FCNCs in the up sector. Furthermore, the i^{th} row of \mathbf{V}_{CKM} respects the unitarity condition $\delta_n^u = 0$ only if the i^{th} SM up quark does not mix with the down-type VLQs. Lastly, $\Delta_n^d = \delta_n^d$ and the first 3 columns of \mathbf{V} coincide with \mathbf{V}_{CKM} .

3.4 Vector-like quark mass scale and perturbativity bounds

In Section 3.2, we mention that SM extensions with VLQs must be particularly careful with the phenomenological constraints concerning tree-level FCNC. Despite discussing in the previous section the interplay between the deviation from unitarity of \mathbf{V}_{CKM} and the magnitude of FCNC, where we concluded that a higher deviation equates to more prevalent FCNCs, we have yet to provide a mechanism to control these phenomena, in order to ensure consistency with experimental observations. For this purpose, we begin by recalling from Eqs. (3.20) and (3.24) that the rotation matrices $\mathbf{V}_{L,R}^{u,d}$ may be parameterised as

$$\mathbf{v} = \begin{pmatrix} \mathbf{V}_K (\mathbb{1} + \mathbf{X}\mathbf{X}^\dagger)^{-\frac{1}{2}} & \mathbb{0} \\ \mathbb{0} & \mathbf{V}_{\bar{K}} (\mathbb{1} + \mathbf{X}^\dagger \mathbf{X})^{-\frac{1}{2}} \end{pmatrix} \begin{pmatrix} \mathbb{1} & \mathbf{X} \\ -\mathbf{X}^\dagger & \mathbb{1} \end{pmatrix}, \quad (3.34)$$

where, by inspection of the bidiagonalisation condition of Eq. (3.6), we infer that the second matrix block diagonalises the mass matrix $\mathcal{H} = \mathcal{M}\mathcal{M}^\dagger$, while the first matrix diagonalises each of the diagonal block matrices. Besides this, the matrices \mathbf{V}_K , $\mathbf{V}_{\bar{K}}$ and \mathbf{X} depend on \mathcal{M} . In order to understand this relation, consider the alternative parameterisation

$$\mathbf{v} = \begin{pmatrix} \mathbb{1} & \mathbf{W} \\ -\mathbf{W}^\dagger & \mathbb{1} \end{pmatrix} \begin{pmatrix} (\mathbb{1} + \mathbf{W}\mathbf{W}^\dagger)^{-\frac{1}{2}} \mathbf{R} & \mathbb{0} \\ \mathbb{0} & (\mathbb{1} + \mathbf{W}^\dagger \mathbf{W})^{-\frac{1}{2}} \bar{\mathbf{R}} \end{pmatrix}. \quad (3.35)$$

The expressions of Eqs. (3.34) and (3.35) are completely equivalent, since we regain the original one by performing the substitutions $\mathbf{W} = \mathbf{V}_K \mathbf{X} \mathbf{V}_{\bar{K}}^\dagger$, $\mathbf{R} = \mathbf{V}_K$ and $\bar{\mathbf{R}} = \mathbf{V}_{\bar{K}}$. Analogously to the previous case, the first matrix block diagonalises \mathcal{H} , which implies from $\mathbf{V}_L^\dagger \mathcal{H} \mathbf{V}_L = \mathcal{D}^2$ that

$$\begin{pmatrix} \mathbb{1} & \mathbf{W}_L \\ -\mathbf{W}_L^\dagger & \mathbb{1} \end{pmatrix} \begin{pmatrix} \mathbf{M}_Y \mathbf{M}_Y^\dagger & \mathbf{M}_Y \mathbf{M}_{\text{VLQ}}^\dagger \\ \mathbf{M}_{\text{VLQ}} \mathbf{M}_Y^\dagger & \mathbf{M}_{\text{VLQ}} \mathbf{M}_{\text{VLQ}}^\dagger \end{pmatrix} \begin{pmatrix} \mathbb{1} & -\mathbf{W}_L \\ \mathbf{W}_L^\dagger & \mathbb{1} \end{pmatrix} = \begin{pmatrix} \mathbf{h} & \mathbb{0} \\ \mathbb{0} & \mathbf{H} \end{pmatrix}, \quad (3.36)$$

where

$$\mathbf{M}_Y^q = \begin{pmatrix} \mathbf{M}_q & \mathbf{M}_{qQ} \end{pmatrix}, \quad \mathbf{M}_{\text{VLQ}}^q = \begin{pmatrix} \mathbf{M}_{Qq} & \mathbf{M}_Q \end{pmatrix}, \quad (3.37)$$

with $q = u(d)$ and $Q = T(B)$ for the up (down) quark sector, and the matrices \mathbf{h} and \mathbf{H} are in general non diagonal. Note from Eq. (3.1) that $(\mathbf{M}_Y)_{ij} = \frac{v}{\sqrt{2}} \mathbf{Y}_{ij}$ is proportional to the EW scale, while the couplings of bare mass terms in Eq. (3.2) correspond to \mathbf{M}_{VLQ} , whose magnitude is determined by the

VLQ mass scale. From the upper right block matrix equality in Eq. (3.36) we obtain the exact relation

$$\mathbf{W}_L = (\mathbf{M}_Y \mathbf{M}_Y^\dagger - \mathbf{W}_L \mathbf{M}_{\text{VLQ}} \mathbf{M}_Y^\dagger) \mathbf{W}_L (\mathbf{M}_{\text{VLQ}} \mathbf{M}_{\text{VLQ}}^\dagger)^{-1} + \mathbf{M}_Y \mathbf{M}_{\text{VLQ}}^\dagger (\mathbf{M}_{\text{VLQ}} \mathbf{M}_{\text{VLQ}}^\dagger)^{-1}. \quad (3.38)$$

Assuming that the VLQ mass scale is much larger than the EW scale, i.e. $\mathbf{M}_Y/\mathbf{M}_{\text{VLQ}} \sim \epsilon$, we are able to compute \mathbf{W}_L in the limit of small deviations from unitarity, applying Eq. (3.38) iteratively, as a power series in ϵ . This hypothesis is not unreasonable, since experimental searches by the ATLAS collaboration for a fourth generation consisting of isosinglet VLQs have already excluded VLQ masses for $m_T \leq 1.31$ TeV and $m_B \leq 1.22$ TeV [94]. However, these bounds are obtained under the assumption that the VLQs only mix with third generation quarks. Hence, in a general scenario where there is no restriction in the mixing between VLQs and SM quarks, these limits must be reevaluated [95]. Nonetheless, the VLQ mass scale is expected to be at least of order of a few hundred GeV. For a more detailed analysis on the experimental constraints on isosinglet VLQs we refer the reader to Section 7 of Ref. [33].

Considering $\mathbf{W}_L = 0$ in the right-hand side of Eq. (3.38) and $\mathbf{M}_Y/\mathbf{M}_{\text{VLQ}} \sim \epsilon$, we write

$$\mathbf{W}_L = \mathbf{M}_Y (\mathbf{M}_{\text{VLQ}})^{-1} \implies \mathbf{X}_L = \mathbf{V}_{\mathbf{K}}^\dagger \mathbf{M}_Y (\mathbf{M}_{\text{VLQ}})^{-1} \mathbf{V}_{\mathbf{K}}, \quad (3.39)$$

to first order in ϵ . This equation already hints that the deviations from unitarity, and therefore the magnitude of FCNC, are controlled by the ratio between the EW scale and the VLQ mass scale. This result is more evident when we rotate the quark fields to a more useful WB, which refers to field transformations that leave the NC and CC unchanged. Namely, considering the following general quark field redefinition:

$$\begin{aligned} u_L &\rightarrow \mathbf{U}_L^u u_L, & T_L &\rightarrow \mathbf{U}_L^T T_L, & U_R &\rightarrow \mathbf{U}_R^U U_R, \\ d_L &\rightarrow \mathbf{U}_L^d d_L, & B_L &\rightarrow \mathbf{U}_L^B B_L, & D_R &\rightarrow \mathbf{U}_R^D D_R, \end{aligned} \quad (3.40)$$

the invariance of the electromagnetic interaction [see Eq. (3.15)] implies that the matrices \mathbf{U} are unitary. Furthermore, invariance of CC interactions [see Eq. (3.10)] implies,

$$\mathbf{V} = \mathbf{A}_L^{u\dagger} \mathbf{A}_L^d \rightarrow \mathbf{A}_L^{u\dagger} \mathbf{U}_L^{u\dagger} \mathbf{U}_L^d \mathbf{A}_L^d \implies \mathbf{U}_L^u = \mathbf{U}_L^d. \quad (3.41)$$

From the above, the invariance of NC is directly satisfied, since $\mathbf{F}^u = \mathbf{V} \mathbf{V}^\dagger$ and $\mathbf{F}^d = \mathbf{V}^\dagger \mathbf{V}$.

When performing a WB transformation, we may employ the well known QR decomposition to write the mass matrices \mathcal{M} in upper ($\mathbf{M}_{Qq} = 0$) or lower ($\mathbf{M}_{qQ} = 0$) triangular form. Then, we are able to diagonalise both matrices \mathbf{M}_T and \mathbf{M}_B with yet another quark field rotation. However, $\mathbf{U}_L^u = \mathbf{U}_L^d$ does not allow the simultaneous diagonalisation both \mathbf{M}_u and \mathbf{M}_d . Thus, the quark mass matrices may always be written in a WB such that

$$\mathcal{M}_u = \begin{pmatrix} \mathbf{d}'_u & \mathbf{M}'_{uT} \\ \mathbb{0} & \mathbf{D}'_u \end{pmatrix}, \quad \mathcal{M}_d = \begin{pmatrix} \mathbf{U}' \mathbf{d}'_d & \mathbf{U}' \mathbf{M}'_{dB} \\ \mathbb{0} & \mathbf{D}'_d \end{pmatrix}, \quad (3.42)$$

or, equivalently,

$$\mathcal{M}_u = \begin{pmatrix} \mathbf{U}'^\dagger \mathbf{d}'_u & \mathbf{U}'^\dagger \mathbf{M}'_{uT} \\ \mathbb{0} & \mathbf{D}'_u \end{pmatrix}, \quad \mathcal{M}_d = \begin{pmatrix} \mathbf{d}'_d & \mathbf{M}'_{dB} \\ \mathbb{0} & \mathbf{D}'_d \end{pmatrix}, \quad (3.43)$$

where \mathbf{d}' and \mathbf{D}' are diagonal matrices, in general different from the diagonal matrices containing the quark masses, and \mathbf{U}' is the residual unitary matrix due to $\mathbf{U}_L^u = \mathbf{U}_L^d$. Nonetheless, it follows from the bidiagonalisation of \mathcal{M} that $\det(\mathcal{D}_q) = \det(\mathcal{M}) = \det(\mathbf{d}'_q \mathbf{D}'_q)$. We are now able to write in this WB the simpler

$$\mathbf{W}_L^u = \mathbf{M}'_{uT} \mathbf{D}'_u{}^{-1}, \quad \mathbf{W}_L^d = \mathbf{M}'_{dB} \mathbf{D}'_d{}^{-1}, \quad (3.44)$$

where it is clear that small deviations from unitarity are determined from the ratio between the EW scale and the VLQ mass scale. However, we have not considered, up until now, the link between the perturbativity of the Yukawa couplings and the deviations from unitarity.

A rudimentary analysis allows us to infer from Eq. (3.44) that the perturbativity of the Yukawa couplings introduces an upper bound on \mathbf{M}_{uT} and \mathbf{M}_{dB} , since these stem from the Yukawa couplings between SM LH quarks and RH VLQs [recall Eq. (3.4)]. Thus, we conclude from Eq. (3.44) that the perturbativity of the Yukawa couplings introduces an upper bound on the unitarity deviations. To explore this relation in more detail, we start once again from the bidiagonalisation condition in Eq. (3.6), which enables us to write

$$\text{Tr}(\mathbf{M}_q \mathbf{M}_q^\dagger + \mathbf{M}_{qQ} \mathbf{M}_{qQ}^\dagger) = \text{Tr} \left(\mathbf{K}_L^q (\mathbf{d}_q + \mathbf{X}_L^q \mathbf{d}_Q \mathbf{X}_L^{q\dagger}) \mathbf{K}_L^{q\dagger} \right), \quad (3.45)$$

where \mathbf{d}_q and \mathbf{D}_q are diagonal matrices containing the SM quarks and VLQs masses, respectively. Considering the limit of small deviations from unitarity and Eq. (3.26), we get

$$\begin{aligned} \text{Tr}(\mathbf{M}_q \mathbf{M}_q^\dagger + \mathbf{M}_{qQ} \mathbf{M}_{qQ}^\dagger) &= \text{Tr} \left((\mathbf{d}_q^2 + \mathbf{X}_L^q \mathbf{d}_Q^2 \mathbf{X}_L^{q\dagger}) (\mathbb{1} + \mathbf{X}_L^q \mathbf{X}_L^{q\dagger})^{-1} \right) \\ &\approx \sum_{i=1}^3 m_i^2 + \sum_{i=1}^3 \sum_{j=1}^{n_Q} |(\mathbf{X}_L^q)_{ij}|^2 M_j^2, \end{aligned} \quad (3.46)$$

with m_i and M_j corresponding to the SM quarks and VLQs masses.

Considering potential small deviations of unitarity in \mathbf{V}_{CKM} , we infer from the discussion in the previous section that the top quark must have small mixings with VLQs. This, combined with the fact that $(\mathbf{V}_{\text{CKM}})_{ub} \sim 10^{-1} (\mathbf{V}_{\text{CKM}})_{cb} \sim 10^{-2} (\mathbf{V}_{\text{CKM}})_{tb}$ [recall Eq. (2.29)], indicates that the top quark mass comes predominantly from $(\mathbf{M}_u)_{33}$, which must be, in turn, the largest entry in \mathbf{M}_Y^u . Furthermore, the top quark is the heaviest quark in the SM, so the matrix elements in \mathbf{M}_Y^d should be lower than $(\mathbf{M}_u)_{33}$. Thus, taking into account the perturbativity of the Yukawa couplings, a sensible parameterisation for the bound on the left-hand side of Eq. (3.46) is

$$\text{Tr}(\mathbf{M}_q \mathbf{M}_q^\dagger + \mathbf{M}_{qQ} \mathbf{M}_{qQ}^\dagger) < \rho m_t^2 \implies \sum_{i=1}^3 \sum_{j=1}^{n_Q} |(\mathbf{X}_L^q)_{ij}|^2 M_j^2 \lesssim \rho m_t^2 - \sum_{i=1}^3 m_i^2 \quad (3.47)$$

where $\rho \lesssim \mathcal{O}(1-10)$. This relation plainly exhibits that the deviations from unitarity are bounded by the

ratio between the EW and VLQ mass scales due to the perturbativity bounds on the Yukawa couplings. This fact is more easily understood in the minimal scenario where only one VLQ is added to the particle content of the SM. In this case, \mathbf{X}_L^q is a 3×1 matrix and Eq. (3.47) is simplified to

$$|(\mathbf{X}_L^q)_1|^2 + |(\mathbf{X}_L^q)_2|^2 + |(\mathbf{X}_L^q)_3|^2 \lesssim \left(\rho m_t^2 - \sum_{i=1}^3 m_i^2 \right) / M_Q^2 \approx (\rho m_t^2 - m_3^2) / M_Q^2, \quad (3.48)$$

where in the last equality we consider $m_{1,2} \ll m_3$. This relation may also be interpreted as an upper bound on the VLQ mass M_Q for a given unitarity deviation. Assuming that the left-hand side of Eq. (3.48) is dominated by the deficit of unitarity in the first row of \mathbf{V}_{CKM} , an upper bound on M_Q is extracted using $\sqrt{\delta_{\text{CKM}}} = 4.1 \times 10^{-2}$ obtained from the fit in Section 2.3 and the quark masses m_t and m_b from the PDG [37]²,

$$M_T \lesssim \left(\sqrt{\rho - 1} \right) 4.2 \text{ TeV} < 12.6 \text{ TeV}, \quad M_B \lesssim \frac{\sqrt{\rho m_t^2 - m_b^2}}{4.1 \times 10^{-2}} < 13.3 \text{ TeV}, \quad (3.49)$$

where $\rho = 10$ in the last inequality.

²These values are presented in Table 4.1 in Chapter 4.

Chapter 4

Minimal SM extension with an up-type isosinglet vector-like quark

In this chapter, the CAA is addressed within a minimal framework featuring a single up-type VLQ $T_{L,R}$, i.e. $n_B = 0$ and $n_T = 1$ [see Eqs. (3.1) and (3.2)]. Furthermore, we approach the *flavour puzzle* by considering texture zeros in the quark mass matrices in order to reduce the number of free parameters of the model, in an attempt to increase its predictivity. These topics are explored in Sec. 4.1, where we identify the set of quark mass matrix pairs $(\mathbf{M}_u, \mathbf{M}_d)$ with a maximal number of texture zeros which are compatible with current experimental data. However, a theoretical framework which justifies the presence of texture zeros has not been provided. A prevalent solution to this issue is the introduction of symmetries which forbid certain quark mass terms, which equates to texture zeros in the mass matrices in Eq. (3.3). Typically, Abelian symmetries are considered, since these constitute one of the simplest symmetry groups. It is also necessary to extend the scalar content of the SM to explain these texture zero structures. In Section 4.2 we determine the minimal scalar sector and Abelian group which originate at least one of the $(\mathbf{M}_u, \mathbf{M}_d)$ pairs found in Section 4.1. This chapter follows closely the methodology employed in Refs. [53, 54].

4.1 Maximally restrictive texture zeros for quarks

We start our analysis by performing a systematic search to identify the maximally restrictive textures pairs $(\mathbf{M}_u, \mathbf{M}_d)$ compatible with quark masses and mixing observables. A pair of textures is said to be maximally restrictive if an additional texture zero in any of the mass matrices renders the pair incompatible with experimental data. This study is based on a standard χ^2 minimisation procedure using the function,

$$\chi^2(x) = \sum_i \frac{[\mathcal{P}_i(x) - \mathcal{O}_i]^2}{\sigma_i^2}, \quad (4.1)$$

where x denotes the matrix elements of \mathbf{M}_u and \mathbf{M}_d ; $\mathcal{P}_i(x)$ is the theoretical prediction for a given observable with corresponding best-fit value \mathcal{O}_i and 1σ experimental error σ_i . The $\chi^2(x)$ function is

Parameter	Best fit $\pm 1\sigma$	3σ range
$m_d(\times \text{ MeV})$	$4.67^{+0.48}_{-0.17}$	$4.16 \rightarrow 6.11$
$m_s(\times \text{ MeV})$	$93.4^{+8.6}_{-3.4}$	$83.2 \rightarrow 119.2$
$m_b(\times \text{ GeV})$	$4.18^{+0.03}_{-0.02}$	$4.12 \rightarrow 4.27$
$m_u(\times \text{ MeV})$	$2.16^{+0.49}_{-0.26}$	$1.38 \rightarrow 3.63$
$m_c(\times \text{ GeV})$	1.27 ± 0.02	$1.21 \rightarrow 1.33$
$m_t(\times \text{ GeV})$	172.69 ± 0.30	$171.79 \rightarrow 173.59$
$ (\mathbf{V}_{\text{CKM}})_{ud} (\times 10^{-1})$	9.7373 ± 0.0031	$9.7280 \rightarrow 9.7466$
$ (\mathbf{V}_{\text{CKM}})_{us} (\times 10^{-1})$	2.243 ± 0.008	$2.219 \rightarrow 2.267$
$ (\mathbf{V}_{\text{CKM}})_{ub} (\times 10^{-3})$	3.82 ± 0.20	$3.22 \rightarrow 4.42$
$ (\mathbf{V}_{\text{CKM}})_{cd} (\times 10^{-1})$	2.21 ± 0.04	$2.09 \rightarrow 2.33$
$ (\mathbf{V}_{\text{CKM}})_{cs} (\times 10^{-1})$	9.75 ± 0.06	$9.57 \rightarrow 9.93$
$ (\mathbf{V}_{\text{CKM}})_{cb} (\times 10^{-2})$	4.08 ± 0.14	$3.66 \rightarrow 4.50$
$ (\mathbf{V}_{\text{CKM}})_{td} (\times 10^{-3})$	8.6 ± 0.2	$8.0 \rightarrow 9.2$
$ (\mathbf{V}_{\text{CKM}})_{ts} (\times 10^{-2})$	4.15 ± 0.09	$3.88 \rightarrow 4.42$
$ (\mathbf{V}_{\text{CKM}})_{tb} $	1.014 ± 0.029	$0.927 \rightarrow 1.101$
$\gamma(^{\circ})$	$65.9^{+3.3}_{-3.5}$	$55.4 \rightarrow 75.8$

Table 4.1: Current data for the SM quark masses, moduli of the CKM matrix entries without imposing unitarity and value of the γ phase [37].

minimized with respect to the SM quark masses, the absolute value of the CKM matrix entries and the unitarity triangle angle $\gamma = \arg(-\mathbf{V}_{ud}\mathbf{V}_{cb}\mathbf{V}_{ub}^*\mathbf{V}_{cd}^*)$ presented in Table 4.1. We assume γ remains unaltered by NP, since its value is measured from tree-level B meson decays [37]. The minimisation procedure was implemented using the Python *iminuit* package [96, 97]. Furthermore, the heavy quark mass is directly constrained by the ATLAS and CMS searches for pair-produced heavy up-type VLQ [94, 98], so we apply the conservative bound $m_T \geq 1$ TeV. We consider a given pair of textures to be compatible with experimental data if the deviation of each observable is at most 3σ at the χ^2 minimum, in which case the pair is also tested at 1σ .

To simplify the analysis of the results, we divide the pairs of textures into equivalence classes with respect to WB permutations, i.e. WB transformations consisting only of permutation matrices, to preserve texture zeros. Thus, we only need to consider a single representative texture pair of each equivalence class, since pairs belonging to the same equivalence class yield the same physical consequences [53, 54]. We exclude textures which are equivalent to upper or lower triangular matrices [38], since these are equivalent to general mass matrices with no texture zeros imposed¹. For the general case of n_B down-type and n_T up-type singlet VLQs, the WB permutations are

$$\mathcal{M}_u \rightarrow \begin{pmatrix} \mathbf{P}_L & \mathbb{0}_{3 \times n_T} \\ \mathbb{0}_{n_T \times 3} & \mathbf{P}_{n_T} \end{pmatrix} \mathcal{M}_u \mathbf{P}_{3+n_T}, \quad \mathcal{M}_d \rightarrow \begin{pmatrix} \mathbf{P}_L & \mathbb{0}_{3 \times n_B} \\ \mathbb{0}_{n_B \times 3} & \mathbf{P}_{n_B} \end{pmatrix} \mathcal{M}_d \mathbf{P}_{3+n_B}, \quad (4.2)$$

where \mathbf{P}_L is a 3×3 permutation matrix common to both left field permutations and the remaining \mathbf{P}_n denote $n \times n$ independent permutation matrices. The maximally restrictive pairs of mass matrix textures $(\mathcal{M}_u, \mathcal{M}_d)$ identified as compatible with data at 1σ and only at 3σ are presented in Tables 4.2 and 4.3,

¹This is a consequence of the QR decomposition discussed in Section 3.4.

\mathcal{M}_u	\mathbf{M}_d
11_1^u	$3_1^d 3_2^d$
11_2^u	$3_2^d 3_3^d$
10_1^u	$4_1^d 4_2^d 4_3^d 4_8^d 4_9^d 4_{10}^d 4_{11}^d 4_{12}^d$
10_2^u	$4_3^d 4_4^d 4_5^d 4_6^d 4_7^d 4_8^d 4_{10}^d 4_{11}^d$
10_3^u	$4_1^d 4_2^d 4_3^d 4_4^d 4_5^d 4_6^d 4_7^d 4_8^d 4_9^d 4_{10}^d 4_{11}^d 4_{12}^d$
10_4^u	$4_1^d 4_2^d 4_3^d 4_4^d 4_5^d 4_6^d 4_7^d 4_8^d 4_9^d 4_{10}^d 4_{11}^d 4_{12}^d$
10_5^u	$4_3^d 4_4^d 4_5^d 4_6^d 4_7^d 4_8^d 4_{10}^d 4_{11}^d$
10_7^u	$4_1^d 4_2^d 4_3^d 4_4^d 4_5^d 4_6^d 4_7^d 4_8^d 4_9^d 4_{10}^d 4_{11}^d 4_{12}^d$
10_8^u	$4_2^d 4_4^d 4_5^d 4_7^d 4_9^d 4_{11}^d 4_{12}^d$

\mathcal{M}_u	\mathbf{M}_d
$9_1^u 9_2^u 9_3^u 9_4^u 9_6^u 9_7^u 9_9^u 9_{11}^u 9_{12}^u 9_{13}^u 9_{14}^u 9_{15}^u 9_{17}^u 9_{18}^u$	5_1^d
$9_1^u 9_3^u 9_4^u 9_6^u 9_7^u 9_8^u 9_9^u 9_{10}^u 9_{11}^u 9_{13}^u 9_{14}^u 9_{15}^u 9_{17}^u 9_{18}^u$	5_2^d
$9_1^u 9_3^u 9_4^u 9_5^u 9_7^u 9_8^u 9_9^u 9_{10}^u 9_{11}^u 9_{12}^u 9_{15}^u 9_{16}^u 9_{18}^u 9_{22}^u$	5_3^d
$9_1^u 9_3^u 9_4^u 9_7^u 9_9^u 9_{11}^u 9_{13}^u 9_{15}^u 9_{17}^u 9_{18}^u$	5_4^d
$9_1^u 9_3^u 9_4^u 9_5^u 9_6^u 9_7^u 9_8^u 9_9^u 9_{10}^u 9_{11}^u 9_{14}^u 9_{15}^u 9_{18}^u$	5_5^d
$9_1^u 9_3^u 9_4^u 9_7^u 9_8^u 9_9^u 9_{10}^u 9_{11}^u 9_{12}^u 9_{13}^u 9_{15}^u 9_{17}^u 9_{18}^u$	5_6^d
$8_1^u 8_2^u 8_3^u 8_4^u 8_5^u 8_6^u 8_7^u 8_8^u 8_9^u 8_{10}^u 8_{11}^u 8_{12}^u 8_{13}^u 8_{14}^u 8_{16}^u 8_{17}^u 8_{18}^u 8_{19}^u 8_{21}^u 8_{25}^u 8_{27}^u$	6_1^d

Table 4.2: Maximally-restrictive $(\mathcal{M}_u, \mathbf{M}_d)$ texture-zeros pairs compatible with quark data at 1σ level.

\mathcal{M}_u	\mathbf{M}_d
10_1^u	$4_4^d 4_5^d 4_6^d 4_7^d$
10_2^u	$4_1^d 4_2^d 4_9^d 4_{12}^d$
10_5^u	$4_1^d 4_2^d 4_9^d 4_{12}^d$
10_6^u	$4_1^d 4_2^d 4_3^d 4_4^d 4_5^d 4_6^d 4_7^d 4_8^d 4_9^d 4_{10}^d 4_{11}^d 4_{12}^d$
$9_5^u 9_8^u 9_{10}^u 9_{16}^u 9_{19}^u 9_{20}^u 9_{21}^u 9_{22}^u 9_{23}^u$	5_1^d
$9_5^u 9_{19}^u 9_{20}^u 9_{21}^u 9_{23}^u$	5_2^d
$9_{13}^u 9_{17}^u 9_{19}^u 9_{20}^u 9_{21}^u$	5_3^d
$9_5^u 9_8^u 9_{10}^u 9_{19}^u 9_{20}^u 9_{21}^u$	5_4^d
$9_{13}^u 9_{17}^u 9_{19}^u 9_{20}^u 9_{21}^u 9_{23}^u$	5_5^d
$9_5^u 9_{16}^u 9_{19}^u 9_{20}^u 9_{21}^u 9_{22}^u$	5_6^d
$8_{15}^u 8_{20}^u 8_{22}^u 8_{23}^u 8_{24}^u 8_{26}^u$	6_1^d

Table 4.3: Maximally-restrictive $(\mathcal{M}_u, \mathbf{M}_d)$ texture-zeros pairs compatible with quark data only at 3σ level.

comprising of 170 and 67 compatible pairs, respectively. The correspondence between each mass matrix label and its representative texture is presented in Tables 4.4, 4.5, 4.6 and 4.7.

As a final note, we comment on the number of non-zero entries of the pairs $(\mathcal{M}_u, \mathbf{M}_d)$. For completeness, we consider the general case of SM extensions with n_T up-type and n_B down-type isosinglet VLQs discussed in the previous Chapter. Phase rotations of quark fields are WB transformations consisting on diagonal matrices with complex phases,

$$\begin{aligned}
u_L &\rightarrow \text{diag}(e^{i\alpha_1}, e^{i\alpha_2}, e^{i\alpha_3}) u_L, & T_L &\rightarrow \text{diag}(e^{i\beta_1}, \dots, e^{i\beta_{n_T}}) T_L, \\
d_L &\rightarrow \text{diag}(e^{i\alpha_1}, e^{i\alpha_2}, e^{i\alpha_3}) d_L, & B_L &\rightarrow \text{diag}(e^{i\gamma_1}, \dots, e^{i\gamma_{n_B}}) B_L, \\
U_R &\rightarrow \text{diag}(e^{i\omega_1}, \dots, e^{i\omega_{n_u}}) U_R, & D_R &\rightarrow \text{diag}(e^{i\eta_1}, \dots, e^{i\eta_{n_d}}) D_R,
\end{aligned} \tag{4.3}$$

$3_1^d \sim \begin{pmatrix} 0 & \times & \times \\ \times & 0 & \times \\ 0 & \times & \times \end{pmatrix}$	$3_2^d \sim \begin{pmatrix} 0 & \times & \times \\ 0 & \times & \times \\ \times & 0 & \times \end{pmatrix}$	$3_3^d \sim \begin{pmatrix} 0 & \times & \times \\ \times & 0 & \times \\ \times & 0 & \times \end{pmatrix}$	
$4_1^d \sim \begin{pmatrix} 0 & \times & \times \\ \times & 0 & 0 \\ \times & 0 & \times \end{pmatrix}$	$4_2^d \sim \begin{pmatrix} 0 & 0 & \times \\ \times & \times & 0 \\ 0 & \times & \times \end{pmatrix}$	$4_3^d \sim \begin{pmatrix} 0 & \times & \times \\ 0 & 0 & \times \\ \times & \times & 0 \end{pmatrix}$	$4_4^d \sim \begin{pmatrix} 0 & \times & \times \\ \times & 0 & \times \\ 0 & 0 & \times \end{pmatrix}$
$4_5^d \sim \begin{pmatrix} 0 & 0 & \times \\ \times & \times & \times \\ 0 & \times & 0 \end{pmatrix}$	$4_6^d \sim \begin{pmatrix} 0 & \times & \times \\ \times & 0 & \times \\ \times & 0 & 0 \end{pmatrix}$	$4_7^d \sim \begin{pmatrix} 0 & 0 & \times \\ 0 & \times & \times \\ \times & \times & 0 \end{pmatrix}$	$4_8^d \sim \begin{pmatrix} \times & \times & \times \\ 0 & 0 & \times \\ 0 & \times & 0 \end{pmatrix}$
$4_9^d \sim \begin{pmatrix} 0 & 0 & \times \\ 0 & \times & \times \\ \times & 0 & \times \end{pmatrix}$	$4_{10}^d \sim \begin{pmatrix} 0 & \times & \times \\ 0 & 0 & \times \\ \times & 0 & \times \end{pmatrix}$	$4_{11}^d \sim \begin{pmatrix} 0 & \times & \times \\ \times & 0 & \times \\ 0 & \times & 0 \end{pmatrix}$	$4_{12}^d \sim \begin{pmatrix} 0 & 0 & \times \\ 0 & \times & 0 \\ \times & \times & \times \end{pmatrix}$
$5_1^d \sim \begin{pmatrix} 0 & 0 & \times \\ 0 & \times & 0 \\ \times & 0 & \times \end{pmatrix}$	$5_2^d \sim \begin{pmatrix} 0 & 0 & \times \\ 0 & \times & 0 \\ \times & \times & 0 \end{pmatrix}$	$5_3^d \sim \begin{pmatrix} 0 & 0 & \times \\ 0 & \times & \times \\ \times & 0 & 0 \end{pmatrix}$	$5_4^d \sim \begin{pmatrix} 0 & \times & \times \\ \times & 0 & 0 \\ 0 & 0 & \times \end{pmatrix}$
$5_5^d \sim \begin{pmatrix} 0 & \times & \times \\ 0 & 0 & \times \\ \times & 0 & 0 \end{pmatrix}$	$5_6^d \sim \begin{pmatrix} 0 & 0 & \times \\ \times & \times & 0 \\ 0 & \times & 0 \end{pmatrix}$		
$6_1^d \sim \begin{pmatrix} 0 & 0 & \times \\ 0 & \times & 0 \\ \times & 0 & 0 \end{pmatrix}$			

Table 4.4: Textures for the 3×3 SM down-type quark mass matrix \mathbf{M}_d .

$10_1^u \sim \begin{pmatrix} 0 & 0 & 0 & \times \\ 0 & \times & \times & 0 \\ \times & 0 & \times & 0 \\ 0 & \times & 0 & 0 \end{pmatrix}$	$10_2^u \sim \begin{pmatrix} 0 & 0 & 0 & \times \\ 0 & 0 & \times & 0 \\ 0 & \times & 0 & \times \\ \times & \times & 0 & 0 \end{pmatrix}$	$10_3^u \sim \begin{pmatrix} 0 & 0 & 0 & \times \\ 0 & 0 & \times & \times \\ \times & \times & 0 & 0 \\ 0 & \times & 0 & 0 \end{pmatrix}$	$10_4^u \sim \begin{pmatrix} 0 & 0 & 0 & \times \\ 0 & 0 & \times & 0 \\ \times & \times & 0 & 0 \\ 0 & \times & 0 & \times \end{pmatrix}$
$10_5^u \sim \begin{pmatrix} 0 & 0 & 0 & \times \\ 0 & 0 & \times & 0 \\ \times & \times & 0 & \times \\ 0 & \times & 0 & 0 \end{pmatrix}$	$10_6^u \sim \begin{pmatrix} 0 & 0 & 0 & \times \\ 0 & 0 & \times & 0 \\ 0 & \times & 0 & \times \\ \times & 0 & 0 & \times \end{pmatrix}$	$10_7^u \sim \begin{pmatrix} 0 & 0 & 0 & \times \\ 0 & 0 & \times & 0 \\ 0 & \times & 0 & \times \\ \times & 0 & \times & 0 \end{pmatrix}$	$10_8^u \sim \begin{pmatrix} 0 & 0 & 0 & \times \\ 0 & 0 & \times & 0 \\ 0 & 0 & 0 & \times \\ 0 & \times & 0 & 0 \\ \times & 0 & \times & \times \end{pmatrix}$
$11_1^u \sim \begin{pmatrix} 0 & 0 & 0 & \times \\ 0 & 0 & \times & 0 \\ \times & \times & 0 & 0 \\ 0 & \times & 0 & 0 \end{pmatrix}$	$11_2^u \sim \begin{pmatrix} 0 & 0 & 0 & \times \\ 0 & 0 & \times & 0 \\ 0 & \times & 0 & 0 \\ \times & 0 & 0 & \times \end{pmatrix}$		

Table 4.5: Textures for the full 4×4 up-type quark mass matrix \mathbf{M}_u , featuring 10 and 11 zeros.

which induce on the mass matrices,

$$\begin{aligned}
(\mathbf{M}_u)_{ij} &\rightarrow e^{i(\omega_j - \alpha_i)} (\mathbf{M}_u)_{ij}, & (\mathbf{M}_d)_{ik} &\rightarrow e^{i(\eta_k - \alpha_i)} (\mathbf{M}_d)_{ik}, \\
(\mathbf{M}_u)_{mj} &\rightarrow e^{i(\omega_j - \beta_m)} (\mathbf{M}_u)_{mj}, & (\mathbf{M}_d)_{nk} &\rightarrow e^{i(\eta_k - \gamma_n)} (\mathbf{M}_d)_{nk}.
\end{aligned} \tag{4.4}$$

Analogous to the SM, the rephasing of the fields eliminates non-physical complex phases in the mass matrices. There are in total $2(n_T + n_B) + 9$ phases. However, these are not independent. The WB transformations of Eq. (4.4) are invariant under an overall rephasing $q \rightarrow e^{i\delta} q$, where q stands for any

$9_1^u \sim \begin{pmatrix} 0 & 0 & 0 & \times \\ 0 & 0 & \times & 0 \\ 0 & \times & 0 & \times \\ \times & \times & \times & 0 \end{pmatrix}$	$9_2^u \sim \begin{pmatrix} 0 & 0 & 0 & \times \\ 0 & 0 & \times & 0 \\ 0 & \times & 0 & 0 \\ \times & \times & \times & \times \end{pmatrix}$	$9_3^u \sim \begin{pmatrix} 0 & 0 & 0 & \times \\ 0 & \times & \times & 0 \\ \times & 0 & \times & \times \\ 0 & \times & 0 & 0 \end{pmatrix}$	$9_4^u \sim \begin{pmatrix} 0 & 0 & 0 & \times \\ 0 & 0 & \times & \times \\ \times & \times & \times & 0 \\ 0 & \times & 0 & 0 \end{pmatrix}$
$9_5^u \sim \begin{pmatrix} 0 & 0 & 0 & \times \\ 0 & \times & \times & 0 \\ \times & 0 & \times & \times \\ \times & 0 & 0 & 0 \end{pmatrix}$	$9_6^u \sim \begin{pmatrix} 0 & 0 & \times & \times \\ 0 & \times & 0 & \times \\ \times & 0 & 0 & \times \\ 0 & 0 & \times & 0 \end{pmatrix}$	$9_7^u \sim \begin{pmatrix} 0 & 0 & 0 & \times \\ 0 & 0 & \times & \times \\ 0 & \times & \times & 0 \\ \times & \times & 0 & 0 \end{pmatrix}$	$9_8^u \sim \begin{pmatrix} 0 & 0 & 0 & \times \\ 0 & 0 & \times & \times \\ \times & \times & 0 & \times \\ 0 & \times & 0 & 0 \end{pmatrix}$
$9_9^u \sim \begin{pmatrix} 0 & 0 & \times & \times \\ 0 & \times & 0 & \times \\ \times & 0 & \times & 0 \\ 0 & \times & 0 & 0 \end{pmatrix}$	$9_{10}^u \sim \begin{pmatrix} 0 & 0 & 0 & \times \\ 0 & 0 & \times & \times \\ \times & \times & 0 & 0 \\ 0 & \times & 0 & \times \end{pmatrix}$	$9_{11}^u \sim \begin{pmatrix} 0 & 0 & 0 & \times \\ 0 & 0 & \times & \times \\ \times & \times & 0 & 0 \\ 0 & \times & \times & 0 \end{pmatrix}$	$9_{12}^u \sim \begin{pmatrix} 0 & 0 & 0 & \times \\ 0 & 0 & \times & 0 \\ \times & \times & 0 & 0 \\ 0 & \times & \times & \times \end{pmatrix}$
$9_{13}^u \sim \begin{pmatrix} 0 & 0 & 0 & \times \\ 0 & 0 & \times & 0 \\ 0 & \times & 0 & \times \\ \times & 0 & \times & \times \end{pmatrix}$	$9_{14}^u \sim \begin{pmatrix} 0 & 0 & 0 & \times \\ 0 & \times & \times & 0 \\ \times & 0 & \times & 0 \\ 0 & 0 & \times & \times \end{pmatrix}$	$9_{15}^u \sim \begin{pmatrix} 0 & 0 & 0 & \times \\ 0 & \times & \times & 0 \\ \times & 0 & \times & 0 \\ 0 & \times & 0 & \times \end{pmatrix}$	$9_{16}^u \sim \begin{pmatrix} 0 & 0 & 0 & \times \\ 0 & 0 & \times & 0 \\ \times & \times & \times & \times \\ 0 & \times & 0 & 0 \end{pmatrix}$
$9_{17}^u \sim \begin{pmatrix} 0 & 0 & 0 & \times \\ 0 & 0 & \times & \times \\ 0 & \times & 0 & \times \\ \times & 0 & \times & 0 \end{pmatrix}$	$9_{18}^u \sim \begin{pmatrix} 0 & 0 & 0 & \times \\ 0 & 0 & \times & 0 \\ \times & \times & 0 & \times \\ 0 & \times & \times & 0 \end{pmatrix}$	$9_{19}^u \sim \begin{pmatrix} 0 & 0 & 0 & \times \\ 0 & 0 & \times & \times \\ 0 & \times & \times & 0 \\ \times & 0 & \times & 0 \end{pmatrix}$	$9_{20}^u \sim \begin{pmatrix} 0 & 0 & 0 & \times \\ 0 & 0 & \times & \times \\ 0 & \times & \times & 0 \\ \times & 0 & 0 & \times \end{pmatrix}$
$9_{21}^u \sim \begin{pmatrix} 0 & 0 & 0 & \times \\ 0 & 0 & \times & 0 \\ 0 & \times & \times & \times \\ \times & 0 & 0 & \times \end{pmatrix}$	$9_{22}^u \sim \begin{pmatrix} 0 & 0 & 0 & \times \\ 0 & 0 & \times & 0 \\ 0 & \times & \times & \times \\ \times & \times & 0 & 0 \end{pmatrix}$	$9_{23}^u \sim \begin{pmatrix} 0 & 0 & 0 & \times \\ 0 & 0 & \times & \times \\ 0 & \times & 0 & \times \\ \times & 0 & 0 & \times \end{pmatrix}$	

Table 4.6: Textures for the full 4×4 up-type quark mass matrix \mathcal{M}_u , featuring 9 zeros.

quark field. Thus, it is possible to eliminate up to $2(n_T + n_B) + 8$ non-physical complex phases in a pair of texture-zero mass matrices $(\mathcal{M}_u, \mathcal{M}_d)$.

To reproduce the experimental quark data in Table 4.1, the mass matrices must have at least one complex entry. Hence, the pairs $(\mathcal{M}_u, \mathcal{M}_d)$ identified in Tables 4.2 and 4.3 must contain a minimum of 11 non-zero entries to introduce the experimentally required complex phase in the mass matrices. This is a consequence of the freedom to eliminate 10 non-physical complex phases through WB rotations.

4.2 Abelian symmetry realisation of compatible textures

The trivial approach would be not extending the scalar sector of the model. However, this is not possible since the presence of texture zeros in this scenario results in massless quarks, rendering the model incompatible with experimental data². Then, a minimal framework must extend the SM scalar content with at least a second Higgs doublet. Models with this scalar sector are commonly known as two-Higgs doublet models (2HDMs). The Higgs fields must have different sets of charges under the Abelian symmetries imposing the texture zeros, otherwise this framework would present the same issues as not extending the

²For details we refer the reader to the Appendix of Ref. [53].

$8_1^u \sim \begin{pmatrix} 0 & 0 & \times & \times \\ 0 & 0 & \times & \times \\ \times & \times & 0 & \times \\ 0 & \times & 0 & 0 \end{pmatrix}$	$8_2^u \sim \begin{pmatrix} 0 & 0 & \times & \times \\ 0 & \times & 0 & \times \\ \times & 0 & \times & \times \\ \times & 0 & 0 & 0 \end{pmatrix}$	$8_3^u \sim \begin{pmatrix} 0 & 0 & 0 & \times \\ 0 & \times & \times & \times \\ \times & 0 & \times & \times \\ 0 & \times & 0 & 0 \end{pmatrix}$	$8_4^u \sim \begin{pmatrix} 0 & 0 & 0 & \times \\ 0 & 0 & \times & \times \\ \times & \times & 0 & 0 \\ 0 & \times & \times & \times \end{pmatrix}$
$8_5^u \sim \begin{pmatrix} 0 & 0 & 0 & \times \\ 0 & 0 & \times & \times \\ \times & \times & 0 & \times \\ 0 & \times & \times & 0 \end{pmatrix}$	$8_6^u \sim \begin{pmatrix} 0 & 0 & 0 & \times \\ 0 & \times & \times & 0 \\ \times & 0 & \times & \times \\ 0 & \times & 0 & \times \end{pmatrix}$	$8_7^u \sim \begin{pmatrix} 0 & 0 & \times & \times \\ 0 & 0 & \times & \times \\ \times & \times & 0 & 0 \\ 0 & \times & 0 & \times \end{pmatrix}$	$8_8^u \sim \begin{pmatrix} 0 & 0 & 0 & \times \\ 0 & 0 & \times & \times \\ \times & \times & \times & 0 \\ 0 & \times & 0 & \times \end{pmatrix}$
$8_9^u \sim \begin{pmatrix} 0 & 0 & \times & \times \\ 0 & \times & 0 & \times \\ \times & 0 & 0 & \times \\ 0 & \times & \times & 0 \end{pmatrix}$	$8_{10}^u \sim \begin{pmatrix} 0 & 0 & 0 & \times \\ 0 & 0 & \times & 0 \\ 0 & \times & 0 & \times \\ \times & \times & \times & \times \end{pmatrix}$	$8_{11}^u \sim \begin{pmatrix} 0 & 0 & \times & \times \\ 0 & \times & 0 & \times \\ \times & 0 & \times & \times \\ 0 & \times & 0 & 0 \end{pmatrix}$	$8_{12}^u \sim \begin{pmatrix} 0 & 0 & \times & \times \\ 0 & \times & 0 & \times \\ \times & 0 & \times & 0 \\ 0 & \times & \times & 0 \end{pmatrix}$
$8_{13}^u \sim \begin{pmatrix} 0 & 0 & 0 & \times \\ 0 & \times & \times & 0 \\ \times & \times & \times & 0 \\ 0 & 0 & \times & \times \end{pmatrix}$	$8_{14}^u \sim \begin{pmatrix} 0 & 0 & 0 & \times \\ 0 & 0 & \times & \times \\ 0 & \times & \times & 0 \\ \times & \times & 0 & \times \end{pmatrix}$	$8_{15}^u \sim \begin{pmatrix} 0 & 0 & 0 & \times \\ 0 & 0 & \times & \times \\ 0 & \times & \times & 0 \\ \times & 0 & \times & \times \end{pmatrix}$	$8_{16}^u \sim \begin{pmatrix} 0 & 0 & 0 & \times \\ 0 & 0 & \times & 0 \\ \times & \times & 0 & \times \\ 0 & \times & \times & \times \end{pmatrix}$
$8_{17}^u \sim \begin{pmatrix} 0 & 0 & 0 & \times \\ 0 & 0 & \times & \times \\ \times & \times & \times & \times \\ 0 & \times & 0 & 0 \end{pmatrix}$	$8_{18}^u \sim \begin{pmatrix} 0 & 0 & 0 & \times \\ 0 & \times & \times & 0 \\ 0 & \times & \times & 0 \\ \times & 0 & \times & \times \end{pmatrix}$	$8_{19}^u \sim \begin{pmatrix} 0 & 0 & \times & \times \\ 0 & 0 & \times & \times \\ 0 & \times & 0 & \times \\ \times & \times & 0 & 0 \end{pmatrix}$	$8_{20}^u \sim \begin{pmatrix} 0 & 0 & \times & \times \\ 0 & 0 & \times & \times \\ 0 & \times & 0 & \times \\ \times & 0 & 0 & \times \end{pmatrix}$
$8_{21}^u \sim \begin{pmatrix} 0 & 0 & 0 & \times \\ 0 & 0 & \times & \times \\ 0 & \times & \times & \times \\ \times & \times & 0 & 0 \end{pmatrix}$	$8_{22}^u \sim \begin{pmatrix} 0 & 0 & 0 & \times \\ 0 & 0 & \times & \times \\ 0 & \times & \times & \times \\ \times & 0 & 0 & \times \end{pmatrix}$	$8_{23}^u \sim \begin{pmatrix} 0 & 0 & 0 & \times \\ 0 & 0 & \times & \times \\ 0 & \times & \times & \times \\ \times & 0 & \times & 0 \end{pmatrix}$	$8_{24}^u \sim \begin{pmatrix} 0 & 0 & \times & \times \\ 0 & 0 & \times & \times \\ 0 & \times & 0 & \times \\ \times & 0 & \times & 0 \end{pmatrix}$
$8_{25}^u \sim \begin{pmatrix} 0 & 0 & 0 & \times \\ 0 & 0 & \times & \times \\ 0 & \times & 0 & \times \\ \times & \times & \times & 0 \end{pmatrix}$	$8_{26}^u \sim \begin{pmatrix} 0 & 0 & 0 & \times \\ 0 & 0 & \times & 0 \\ 0 & \times & \times & \times \\ \times & 0 & \times & \times \end{pmatrix}$	$8_{27}^u \sim \begin{pmatrix} 0 & 0 & 0 & \times \\ 0 & 0 & \times & 0 \\ \times & 0 & \times & 0 \\ 0 & \times & \times & \times \end{pmatrix}$	

Table 4.7: Textures for the full 4×4 up-type quark mass matrix \mathbf{M}_u , featuring 8 zeros.

scalar sector. We parameterise the scalar multiplets as,

$$\Phi_a = \begin{pmatrix} \phi_a^+ \\ \phi_a^0 \end{pmatrix} = \frac{1}{\sqrt{2}} \begin{pmatrix} \sqrt{2}\phi_a^+ \\ v_a e^{i\theta_a} + \rho_a + i\eta_a \end{pmatrix}, \quad a = 1, 2, \quad (4.5)$$

where v_a are the VEVs of the neutral component of the Higgs doublets ϕ_a^0 . Note that only the phase difference $\theta = \theta_2 - \theta_1$ is physical. In this scenario, the relevant Yukawa and mass Lagrangian is

$$\begin{aligned} -\mathcal{L}_{\text{Yuk.}} = & \overline{q_L} (\mathbf{Y}_d^1 \Phi_1 + \mathbf{Y}_d^2 \Phi_2) d_R + \overline{q_L} (\mathbf{Y}_u^1 \tilde{\Phi}_1 + \mathbf{Y}_u^2 \tilde{\Phi}_2) u_R \\ & + \overline{q_L} (\mathbf{Y}_{uT}^1 \tilde{\Phi}_1 + \mathbf{Y}_{uT}^2 \tilde{\Phi}_2) T_R + \overline{T_L} \mathbf{M}_{Tu} u_R + M_T \overline{T_L} T_R + \text{H.c.}, \end{aligned} \quad (4.6)$$

where $\mathbf{Y}_{d,u}^{1,2}$ are 3×3 Yukawa matrices of SM quarks, $\mathbf{Y}_{uT}^{1,2}$ are 3×1 Yukawa vectors, \mathbf{M}_{Tu} is a 1×3 mass vector and M_T is the bare mass for the VLQ T . Upon EWSB, triggered when the Higgs doublets

acquire non-zero VEVs, the following mass matrices are generated,

$$\begin{aligned} \mathbf{M}_d &= \frac{v_1}{\sqrt{2}} \mathbf{Y}_d^1 + \frac{v_2 e^{i\theta}}{\sqrt{2}} \mathbf{Y}_d^2, & \mathbf{M}_u &= \frac{v_1}{\sqrt{2}} \mathbf{Y}_u^1 + \frac{v_2 e^{-i\theta}}{\sqrt{2}} \mathbf{Y}_u^2, \\ \mathbf{M}_{uT} &= \frac{v_1}{\sqrt{2}} \mathbf{Y}_{uT}^1 + \frac{v_2 e^{-i\theta}}{\sqrt{2}} \mathbf{Y}_{uT}^2, & \mathbf{M}_u^{\text{Yuk.}} &= \begin{pmatrix} \mathbf{M}_u & \mathbf{M}_{uT} \end{pmatrix}. \end{aligned} \quad (4.7)$$

The field transformations under a general Abelian flavour symmetry are given by

$$\Phi_a \rightarrow \mathbf{X}_{\Phi_a} \Phi_a, \quad q_L \rightarrow \mathbf{X}_{q_L} q_L, \quad d_R \rightarrow \mathbf{X}_{d_R} d_R, \quad u_R \rightarrow \mathbf{X}_{u_R} u_R, \quad T_{L,R} \rightarrow e^{ix_{T_{L,R}}} T_{L,R}, \quad (4.8)$$

where \mathbf{X}_F are diagonal matrices with complex phases e^{ix_F} without loss of generality. Requiring invariance of the full Lagrangian under these symmetry transformations imposes the following constraints on the mass matrices:

$$\begin{aligned} \mathbf{Y}_d^a &= \mathbf{X}_{q_L}^\dagger \mathbf{Y}_d^a \mathbf{X}_{d_R} \mathbf{X}_{\Phi_a}, & \mathbf{Y}_u^a &= \mathbf{X}_{q_L}^\dagger \mathbf{Y}_u^a \mathbf{X}_{u_R} \mathbf{X}_{\Phi_a}^*, \\ \mathbf{Y}_{uT}^a &= \mathbf{X}_{q_L}^\dagger \mathbf{Y}_{uT}^a \mathbf{X}_{\Phi_a}^* e^{ix_{T_R}}, & \mathbf{M}_{Tu} &= e^{-ix_{T_L}} \mathbf{M}_{Tu} \mathbf{X}_{u_R}, \\ \mathbf{M}_T &= e^{i(x_{T_R} - x_{T_L})} \mathbf{M}_T, \end{aligned} \quad (4.9)$$

which define the following system of linear equations for the phases x_F :

$$\begin{aligned} (\mathbf{Y}_d^a)_{ij} = 0 &\iff x_{q_{Li}} - x_{d_{Rj}} - x_{\Phi_a} \neq 0, & (\mathbf{Y}_u^a)_{ij} = 0 &\iff x_{q_{Li}} - x_{u_{Rj}} + x_{\Phi_a} \neq 0, \\ (\mathbf{Y}_{uT}^a)_i = 0 &\iff x_{q_{Li}} - x_{T_R} - x_{\Phi_a} \neq 0, & (\mathbf{M}_{Tu})_j = 0 &\iff x_{T_L} - x_{d_{Rj}} \neq 0, \\ (\mathbf{M}_T) &= 0 \iff x_{T_L} - x_{T_R} \neq 0. \end{aligned} \quad (4.10)$$

A given Yukawa entry is non-zero if the respective phase relation is satisfied for one of the Higgs doublets.

In what follows we determine which of the maximally restrictive texture pairs compatible with quark data (see Tables 4.2 and 4.3) are realisable by imposing discrete or continuous global Abelian symmetries. We employ the methodology described in Refs. [40, 53, 54]. This consists of employing the canonical method [45, 99], responsible for identifying the realisable texture pairs and corresponding field transformation charges, followed by the Smith Normal Form (SNF) method [100, 101], that ascertains the minimal Abelian group under which such textures are symmetric.

In the canonical method we begin by performing all possible decompositions of a given texture pair $(\mathbf{M}_u, \mathbf{M}_d)$ into the corresponding Yukawa matrices as described in Eq. (4.7). As previously explained, each decomposition defines a system of linear equations for the field transformation phases x_F , defined in Eq. (4.10). If a solution exists for a given set of charges, the corresponding decomposition is realisable by a global Abelian symmetry. This method identified two maximally restrictive texture pairs realisable through Abelian symmetries. The corresponding decompositions and $U(1)_F$ field charges are presented in Tables 4.9 and 4.8, respectively. An indepth analysis regarding the non-realisable texture pairs is performed in Appendix A.

The SNF analysis identifies $U(1)^3$ as the minimal Abelian group that leaves the $\mathcal{L}_{\text{Yuk.}}$ invariant for the decompositions identified in Table 4.9. This result is interpreted as follows: $\mathcal{L}_{\text{Yuk.}}$ is invariant under the gauge group $U(1)_Y$ [recall Eq.(2.1)], where Y stands for the hypercharge; it also exhibits an

Fields	Φ_1	Φ_2	q_{u_L}	q_{c_L}	q_{t_L}	u_R	c_R	t_R	d_R	s_R	b_R	T_L	T_R
$(9_9^u, 5_1^d)$	0	1	0	1	-1	-1	2	0	-2	1	-1	2	1
$(9_9^u, 5_3^d)$	0	1	0	1	-1	-1	2	0	-2	1	0	2	1

Table 4.8: Maximally-restrictive texture sets $(\mathcal{M}_u, \mathbf{M}_d)$ realisable through an Abelian flavour symmetry $U(1)_F$. We provide the field transformation charges under $U(1)_F$ expressed as multiples of an arbitrary charge q_F .

\mathcal{M}_u	\mathbf{Y}_u^1	\mathbf{Y}_u^2	\mathbf{Y}_{uT}^1	\mathbf{Y}_{uT}^2	\mathbf{M}_{Tu}	M_T
9_9^u	$\begin{pmatrix} 0 & 0 & \times \\ 0 & 0 & 0 \\ \times & 0 & 0 \end{pmatrix}$	$\begin{pmatrix} 0 & 0 & 0 \\ 0 & \times & 0 \\ 0 & 0 & \times \end{pmatrix}$	$\begin{pmatrix} 0 \\ \times \\ 0 \end{pmatrix}$	$\begin{pmatrix} \times \\ 0 \\ 0 \end{pmatrix}$	$\begin{pmatrix} 0 & \times & 0 \end{pmatrix}$	0
\mathbf{M}_d	\mathbf{Y}_d^1	\mathbf{Y}_d^2				
5_1^d	$\begin{pmatrix} 0 & 0 & 0 \\ 0 & \times & 0 \\ 0 & 0 & \times \end{pmatrix}$	$\begin{pmatrix} 0 & 0 & \times \\ 0 & 0 & 0 \\ \times & 0 & 0 \end{pmatrix}$				
5_3^d	$\begin{pmatrix} 0 & 0 & \times \\ 0 & \times & 0 \\ 0 & 0 & 0 \end{pmatrix}$	$\begin{pmatrix} 0 & 0 & 0 \\ 0 & 0 & \times \\ \times & 0 & 0 \end{pmatrix}$				

Table 4.9: Decomposition of mass matrices into the Yukawa or bare mass textures, according to Eqs. (4.6) and (4.7), for the maximally-restrictive texture pairs $(\mathcal{M}_u, \mathbf{M}_d)$ of Table 4.8.

accidental global symmetry $U(1)_B$, where B stands for baryon number, i.e. the interactions encoded in our framework preserve B ³. Finally, the remaining $U(1)_F$ is the Abelian flavour symmetry identified by the canonical method, which implements the texture zeros. As a final comment, the $U(1)_F$ symmetries can be discretised into a minimal set of discrete charges corresponding to a \mathbb{Z}_5 symmetry.

4.3 Parameter space scan

Recalling the discussion in Sec. 4.1, the maximally restrictive pairs identified in Table 4.9 contain a single physical complex phase θ . Thus, a possible parameterisation for these textures is:

$$9_9^u : \begin{pmatrix} 0 & 0 & a_1 & b_1 \\ 0 & b_2 & 0 & a_2 \\ a_3 & 0 & b_3 & 0 \\ 0 & c & 0 & 0 \end{pmatrix}, \quad 5_1^d : \begin{pmatrix} 0 & 0 & x_1 \\ 0 & m_{\text{dec.}} & 0 \\ x_2 & 0 & \rho e^{i\theta} \end{pmatrix}, \quad 5_3^d : \begin{pmatrix} 0 & 0 & x_1 \\ 0 & x_2 & \rho e^{i\theta} \\ m_{\text{dec.}} & 0 & 0 \end{pmatrix}, \quad (4.11)$$

where all parameters are real and positive. The textures 5_1^d and 5_3^d contain a decoupled quark state. Hence, for each texture pair we must consider the scenarios $m_{\text{dec.}} = m_d, m_s, m_b$. The Hermitian matrices

³Our framework does not present mixing among leptons. Thus, analogously to the SM, the lepton family number is conserved, while the mixing between quarks permits only total baryon number conservation.

\mathcal{H}^d defined in Eq. (3.6) are given by:

$$5_1^d : \mathcal{H} = \begin{pmatrix} x_1^2 & 0 & x_1 \rho e^{-i\theta} \\ 0 & m_{\text{dec.}}^2 & 0 \\ x_1 \rho e^{i\theta} & 0 & x_2^2 + \rho^2 \end{pmatrix}, \quad 5_3^d : \mathcal{H} = \begin{pmatrix} 0 & x_1^2 & x_1 \rho e^{-i\theta} \\ 0 & x_1 \rho e^{i\theta} & x_2^2 + \rho^2 \\ m_{\text{dec.}}^2 & 0 & 0 \end{pmatrix}. \quad (4.12)$$

The roots of the characteristic polynomial of \mathcal{H} for 5_1^d and 5_3^d lead to,

$$x_1^2 = \frac{M^2 m^2}{x_2^2}, \quad \rho^2 = \frac{(M^2 - x_2^2)(x_2^2 - m^2)}{x_2^2}, \quad m < x_2 < M, \quad (4.13)$$

where M and m correspond to the heavy and light quark mass parameter, respectively, and $m_{\text{dec.}}$ is the mass of the decoupled down quark. The mass matrices present a total of 12 physical parameters to the 16 experimental observables in Table 4.1.

Given the experimentally measured quark masses in Table 4.1, the down matrix textures are described by two parameters: θ and x_2 . In Fig. 4.1, we present the result of the parameter scan where we vary θ and x_2 , leaving the entries of \mathcal{M}_u to be determined by the minimisation procedure described in Eq. (4.1). For each pair we consider the scenario where the decoupled quark corresponds to the down ($5_{1,3}^d$), strange ($5_{1,3}^s$) or bottom ($5_{1,3}^b$) quark. Hereinafter, we use this notation to indicate which down quark is taken to be decoupled. In Table 4.10 we present the results for the best fit points, i.e. the quark mass textures which reproduce the χ^2 minimum for each case, displayed as black dots in Fig. 4.1. The overall best fit point $\chi_{\text{min}}^2 = 1.60$ is obtained from the 5_3^s pair. Defining $\Delta\chi^2 = \chi^2(x_2, \theta) - \chi_{\text{min}}^2$, we display the $\leq 1\sigma$, $\leq 2\sigma$ and $\leq 3\sigma$ regions, which correspond to $\Delta\chi^2 \leq 2.3, 6.18, 11.83$, in grey, blue and magenta, respectively. To demonstrate the parameter regions which accommodate the CAA, we take $|\mathbf{V}_{ud}|$ and $|\mathbf{V}_{us}|$ obtained for each point in the parameter scan and plot the $\Delta\chi_{\text{non-uni.}}^2$ 1, 2 and 3 σ contours (green lines), following the procedure described in Sec. 2.3. Thus, these contours are analogous to the ones in Fig. 2.4.

From the inspection of these plots, it is clear that the decoupled quark state strongly influences the compatibility of the texture pairs with experimental data: only 5_1^d , 5_3^s and 5_3^b present parameter regions compatible at the $\Delta\chi^2$ and $\Delta\chi_{\text{non-uni.}}^2$ 1 σ level. Furthermore, despite complying with experimental data and the CAA at 1 σ , the 5_3^b texture's parameter space provides less freedom to retain compatibility with both requirements when compared to 5_1^d and 5_3^s : in these cases the $\Delta\chi^2 < 3\sigma$ regions are within the $\Delta\chi_{\text{non-uni.}}^2 = 1\sigma$ contour, whereas for 5_3^b this is true only for $\Delta\chi^2 < 1\sigma$. We remark that the parameter space for all cases is heavily constrained, with the $\Delta\chi^2 \leq 3\sigma$ regions falling within a $\Delta\theta = 10^\circ$ and Δx_2 of the order of ~ 10 eV. The small Δx_2 is a consequence of the magnitude of the only complex entry in the textures pairs being controlled by the parameter ρ , which is extremely sensitive to x_2 [check Eq. (4.13)]. This is particularly noticeable for the decoupled s quark scenario, where the fine-tuning of x_2 is critical, since $\rho^2 \sim m_b^2 \left[1 - \left(\frac{m_d}{x_2} \right)^2 \right]$ with $x_2^2 - m_d^2$ of the order of $\sim 10^{-1}$ eV. This analysis is corroborated by the results obtained for the remaining cases, where the smaller mass differences between the mixing quarks allow a larger Δx_2 interval: $\left(\frac{m_d}{m_b} \right)^2 \ll \left(\frac{m_s}{m_b} \right)^2 < \left(\frac{m_d}{m_s} \right)^2$ results in $\Delta x_2^s \ll \Delta x_2^d < \Delta x_2^b$.

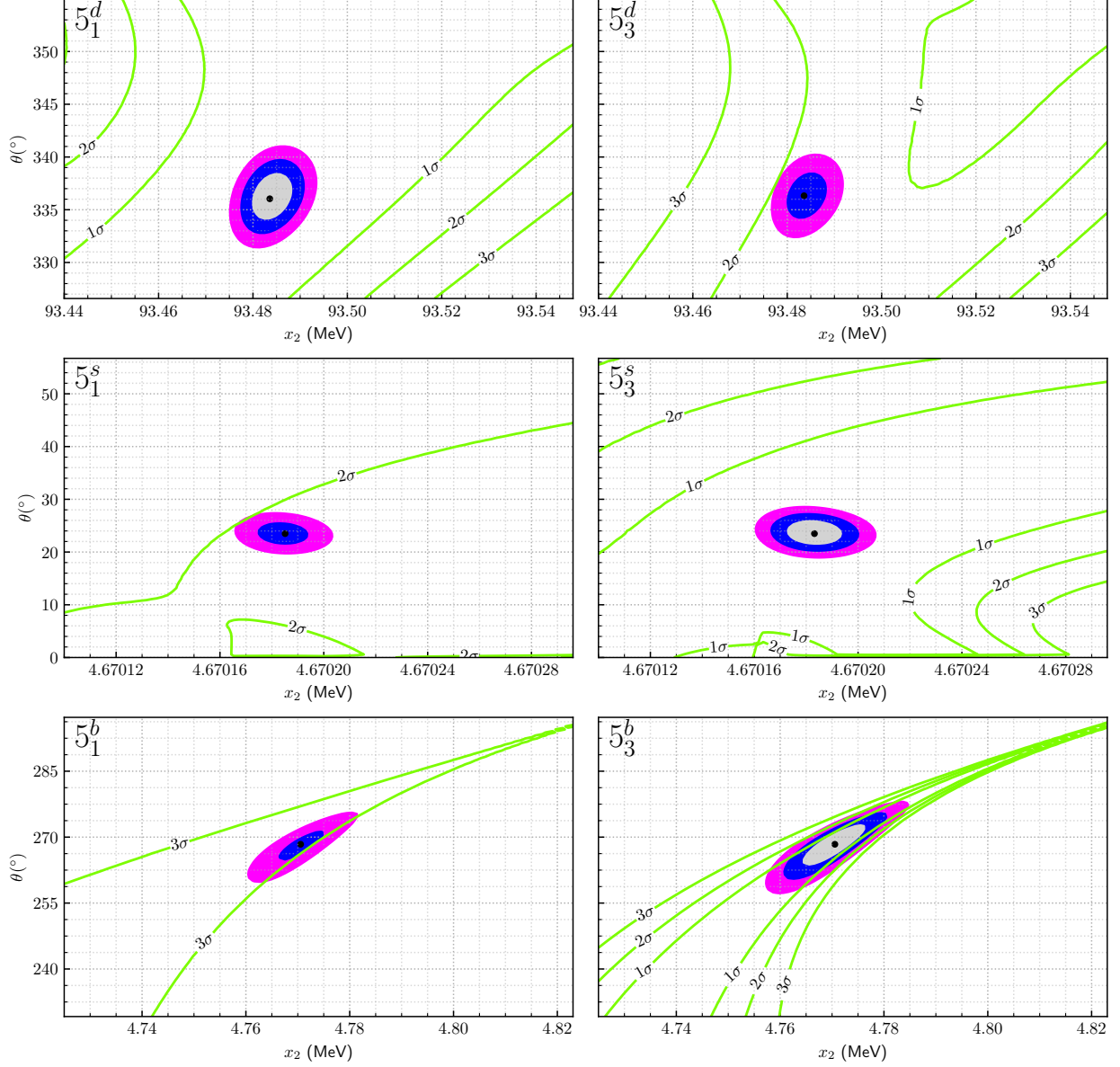


Figure 4.1: Constraints on the (x_2, θ) parameter space imposed by quark experimental data in Table 4.1. The 1, 2 and 3 σ regions for $\Delta\chi^2$ are coloured in grey, blue and magenta, respectively. The green contours representing the 1, 2 and 3 σ for $\Delta\chi^2_{\text{non-uni.}}$ are determined following the procedure described in Sec. 2.3.

	\mathcal{M}_u	\mathbf{M}_d	χ^2
5_1^d	$\begin{pmatrix} 0 & 0 & 32543.4288 & 169589.227 \\ 0 & 155377.331 & 0 & 1511.22775 \\ 9.64008562 & 0 & 1260.27030 & 0 \\ 0 & 3801809.27 & 0 & 0 \end{pmatrix}$	$\begin{pmatrix} 0 & 0 & 4176.2438 \\ 0 & 4.67 & 0 \\ 93.48401 & 0 & 162.15636 - 71.2556385i \end{pmatrix}$	1.63
5_3^d	$\begin{pmatrix} 0 & 0 & 169550.382 & 32745.1404 \\ 0 & 99245.0599 & 0 & 1266.20457 \\ 2.21782290 & 0 & 1511.62308 & 0 \\ 0 & 1006764.26 & 0 & 0 \end{pmatrix}$	$\begin{pmatrix} 0 & 0 & 4176.24058 \\ 0 & 93.48408 & 162.31258 - 71.0883833i \\ 4.67 & 0 & 0 \end{pmatrix}$	5.53
5_1^s	$\begin{pmatrix} 0 & 0 & 29616.5242 & 169982.901 \\ 0 & 505104.895 & 0 & 7242.20632 \\ 2.21744025 & 0 & 291.173026 & 0 \\ 0 & 5689602.78 & 0 & 0 \end{pmatrix}$	$\begin{pmatrix} 0 & 0 & 4179.83512 \\ 0 & 93.4 & 0 \\ 4.67018 & 0 & 34.04346 + 14.8113677i \end{pmatrix}$	5.90
5_3^s	$\begin{pmatrix} 0 & 0 & 169977.717 & 29647.5794 \\ 0 & 44930.4037 & 0 & 289.497733 \\ 9.63825232 & 0 & 7208.47370 & 0 \\ 0 & 1098465.92 & 0 & 0 \end{pmatrix}$	$\begin{pmatrix} 0 & 0 & 4179.83614 \\ 0 & 4.67018 & 33.89142 + 14.8741728i \\ 93.4 & 0 & 0 \end{pmatrix}$	1.60
5_1^b	$\begin{pmatrix} 0 & 0 & 1265.86194 & 7253.83909 \\ 0 & 312688.793 & 0 & 172913.613 \\ 2.16951456 & 0 & 115.823913 & 0 \\ 0 & 4736701.10 & 0 & 0 \end{pmatrix}$	$\begin{pmatrix} 0 & 0 & 91.427802 \\ 0 & 4180 & 0 \\ 4.77072773 & 0 & -0.607315667 - 19.05688i \end{pmatrix}$	6.72
5_3^b	$\begin{pmatrix} 0 & 0 & 7254.64591 & 1265.58205 \\ 0 & 134588.688 & 0 & 115.644411 \\ 565.232095 & 0 & 172536.618 & 0 \\ 0 & 3374995.35 & 0 & 0 \end{pmatrix}$	$\begin{pmatrix} 0 & 0 & 91.4346185 \\ 0 & 4.77038136 & -0.528168219 - 19.02745i \\ 4180 & 0 & 0 \end{pmatrix}$	1.71

Table 4.10: Quark mass matrices identified applying the χ^2 minimisation procedure described in Sec. 4.1 to the maximally-restrictive textures presented in Table 4.8. The superscript $q = d, s, b$ corresponds to the decoupled down quark state. The results are presented in units of MeV.

Focusing now on Table 4.10, we notice a similarity between some of the best fit values of $(9_9^u, 5_1^d)$ and $(9_9^u, 5_3^d)$ for the same decoupled quark state. To thoroughly explain this feature, the full reconstruction of the unitary matrices \mathbf{V}_L^u and quark masses from the mass matrices entries must be known. However, the analytical solution to the characteristic polynomial of \mathcal{H}^u and the calculation of the mixing angles of \mathbf{V}_L^u for 9_9^u are cumbersome, rendering this method unviable. Hence, in what follows we construct a heuristic argument which addresses this observation. Recalling the definition of WB permutations in Eq. (4.2) and the mass matrices parameterisation of Eq. (4.11), we rewrite the $(9_9^u, 5_3^d)$ into the physically equivalent:

$$\begin{aligned}
9_9^u : & \begin{pmatrix} 1 & 0 & 0 & 0 \\ 0 & 0 & 1 & 0 \\ 0 & 1 & 0 & 0 \\ 0 & 0 & 0 & 1 \end{pmatrix} \begin{pmatrix} 0 & 0 & a_1 & b_1 \\ 0 & b_2 & 0 & a_2 \\ a_3 & 0 & b_3 & 0 \\ 0 & c & 0 & 0 \end{pmatrix} \begin{pmatrix} 0 & 1 & 0 & 0 \\ 1 & 0 & 0 & 0 \\ 0 & 0 & 0 & 1 \\ 0 & 0 & 1 & 0 \end{pmatrix} = \begin{pmatrix} 0 & 0 & b_1 & a_1 \\ 0 & a_3 & 0 & b_3 \\ b_2 & 0 & a_2 & 0 \\ c & 0 & 0 & 0 \end{pmatrix} = 9_9^{u'} , \\
5_3^d : & \begin{pmatrix} 1 & 0 & 0 \\ 0 & 0 & 1 \\ 0 & 1 & 0 \end{pmatrix} \begin{pmatrix} 0 & 0 & x_1 \\ 0 & x_2 & \rho e^{i\theta} \\ m_{\text{dec.}} & 0 & 0 \end{pmatrix} \begin{pmatrix} 0 & 1 & 0 \\ 1 & 0 & 0 \\ 0 & 0 & 1 \end{pmatrix} = \begin{pmatrix} 0 & 0 & x_1 \\ 0 & m_{\text{dec.}} & 0 \\ x_2 & 0 & \rho e^{i\theta} \end{pmatrix} = 5_1^d .
\end{aligned} \tag{4.14}$$

It is clear in this WB that the coupling of the VLQ T_L with the SM RH quarks distinguishes the pairs $(9_9^{u'}, 5_1^d) \equiv (9_9^u, 5_3^d)$ and $(9_9^u, 5_1^d)$: in 9_9^u this coupling comes from the bare mass term $\propto \overline{T}_L u_{R_2} + \text{H.c.}$, while in $9_9^{u'}$ it stems from $\propto \overline{T}_L u_{R_1} + \text{H.c.}$. From Eqs. (3.6) and (3.11), it follows that the structure of $\mathcal{H}^{u,d}$ is critical for the fit quality of the $|\mathbf{V}_{\text{CKM}}|$ entries:

$$\begin{aligned}
9_9^u : \mathcal{H} &= \begin{pmatrix} a_1^2 + b_1^2 & a_2 b_1 & a_1 b_3 & 0 \\ a_2 b_1 & a_2^2 + b_2^2 & 0 & b_2 c \\ a_1 b_3 & 0 & a_3^2 + b_3^2 & 0 \\ 0 & b_2 c & 0 & c^2 \end{pmatrix} , \\
9_9^{u'} : \mathcal{H} &= \begin{pmatrix} a_1^2 + b_1^2 & a_1 b_3 & a_2 b_1 & 0 \\ a_1 b_3 & a_3^2 + b_3^2 & 0 & 0 \\ a_2 b_1 & 0 & a_2^2 + b_2^2 & a_3 c \\ 0 & 0 & a_3 c & c^2 \end{pmatrix} \xrightarrow{\substack{a_1 \leftrightarrow b_1 \\ a_2 \leftrightarrow b_3 \\ a_3 \leftrightarrow b_2}} \begin{pmatrix} a_1^2 + b_1^2 & a_2 b_1 & a_1 b_3 & 0 \\ a_2 b_1 & a_2^2 + b_2^2 & 0 & 0 \\ a_1 b_3 & 0 & a_3^2 + b_3^2 & b_2 c \\ 0 & 0 & b_2 c & c^2 \end{pmatrix} .
\end{aligned} \tag{4.15}$$

The matrices \mathcal{H}^u in Eq. (4.15) have an identical structure, after the relabeling performed in $9_9^{u'}$, except for the entries highlighted in red, stemming from the distinct coupling of T_L mentioned previously. Given that the $(9_9^u, 5_1^d)$ and $(9_9^{u'}, 5_1^d) \equiv (9_9^u, 5_3^d)$ pairs present the same \mathbf{M}_d texture, the more similar the \mathcal{H}^u matrices of these pairs are, the closer the resulting \mathbf{V} mixing matrix will be. Then, it is natural to assume that the entries colored in blue should be identical, while the parameters a_3 , b_2 and c differ in order to accommodate the identified structural difference. Under this assumption, the best fit values for $(9_9^u, 5_1^d)$ and $(9_9^u, 5_3^d)$ should present similar values for x_2 , θ , a_1 , a_3 , b_1 and b_2 , with one of the pairs performing the relabeling presented in Eq. (4.15). This is precisely what is observed in the textures pairs presented in Table 4.10: for each decoupled quark scenario, the corresponding a_1 , a_3 , b_1 and b_2 parameters between the texture pairs differ at most $\sim 0.7\%$.

Chapter 5

Flavour phenomenology

In the previous chapter, we identified the maximally-restrictive textures in the context of a 2HDM with an up-type isosinglet VLQ compatible with quark data. In fact, these textures present a better fit to the CAA when compared to the SM. However, as stated in Sec. 3.2, the introduction of VLQs in the theory leads to FCNC mediated by the Z and Higgs bosons. We now address solely the phenomenological consequences of introducing an up isosinglet VLQ, focusing on the NP contributions to quark flavour processes: neutral mesons mixing, rare top decays and rare meson decays. Thus, in what follows, we consider the alignment limit, i.e. one of the Higgs fields corresponds to the SM Higgs with mass $m_H = 125.25 \pm 0.17$ GeV, and assume the masses of the remaining scalars to be several orders above the EW scale, decoupling the 2HDM phenomenology from our model. In Sec. 5.1 we briefly discuss the processes which present the strongest constraints the model. In Sec. 5.2, we discuss the results of a global analysis taking into account both the quark data listed in Table 4.1 and the phenomenological constraints reviewed.

5.1 Observables

Throughout this chapter, we employ the Inami-Lim functions [102, 103] listed in Appendix B and the SM physical constants in Table 5.1. At the end of each subsection, we present a table containing the experimental values necessary to perform the theoretical calculations. Furthermore, we define the quantities

$$\lambda_{\beta\alpha}^i = V_{i\beta}^* V_{i\alpha}, \quad x_i = m_i^2/m_W^2, \quad (5.1)$$

where $i = u, c, t, T$ and $\alpha, \beta = d, s, b$, which will prove useful hereinafter.

A few comments are in order concerning the next subsections. Firstly, some of the phenomenological constraints concerning kaon physics will not present a rephasing invariant expression. These equations, namely (5.7), (5.33) and (5.52), are only valid in a parameterisation where λ_{sd}^u is real [104]. Finally, following the reasoning presented in Ref. [104], we approximate the QCD corrections to the VLQ T to the t ones, i.e. $\eta_T \approx \eta_t$ and $\eta_{cT} \approx \eta_{ct}$, since renormalisation group evolution is slower at larger scales.

G_F	$1.1663787(6) \times 10^{-5} \text{ GeV}^{-2}$ [37]	m_W	$80.377 \pm 0.012 \text{ GeV}$ [37]
s_W^2	$0.23121(4)$ [37]	α_{em}	$1/137.036$ [37]
m_H	$125.25 \pm 0.17 \text{ GeV}$ [37]	m_Z	$91.1876 \pm 0.0021 \text{ GeV}$ [37]
m_μ	$105.6583755(23) \text{ MeV}$ [37]		

Table 5.1: SM physical constants taken from the PDG [37].

5.1.1 Meson mixing

We begin by discussing the neutral meson mixings $K^0 - \bar{K}^0$, $B_d^0 - \bar{B}_d^0$ and $B_s^0 - \bar{B}_s^0$. The mesons K^0 , B_d^0 and B_s^0 have as valence quarks $d\bar{s}$, $d\bar{b}$ and $s\bar{b}$, respectively. In what follows we use the notation P^0 , to refer to any of these mesons, since the model contributions to their mixing will be similar. For details regarding meson mixing, we refer the reader to Ref. [105], that serves as the main theoretical background of this subsection.

Consider an initial state $|\psi\rangle$ which is a superposition of P^0 and \bar{P}^0 :

$$|\psi(0)\rangle = a(0)|P^0\rangle + b(0)|\bar{P}^0\rangle. \quad (5.2)$$

After a given time t , the state acquires components corresponding to the possible decay final states $|n_i\rangle$:

$$|\psi(t)\rangle = a(t)|P^0\rangle + b(t)|\bar{P}^0\rangle + \sum_i c_i(t)|n_i\rangle. \quad (5.3)$$

If we are interested in studying only the neutral meson mixing $P^0 - \bar{P}^0$, i.e. we want to compute only the $a(t)$ and $b(t)$ values, and consider a time scale t much larger than the typical strong-interaction scale, we may use a simplified formalism [106]. In this formalism, the two-component wave function:

$$|\psi(t)\rangle = \psi_1|P^0\rangle + \psi_2|\bar{P}^0\rangle \quad (5.4)$$

evolves according to the Schrödinger like equation:

$$i \frac{d}{dt} \begin{pmatrix} \psi_1 \\ \psi_2 \end{pmatrix} = \mathbf{R} \begin{pmatrix} \psi_1 \\ \psi_2 \end{pmatrix}, \quad (5.5)$$

where $\mathbf{R} = \mathbf{M} + i\mathbf{\Gamma}$, with \mathbf{M} and $\mathbf{\Gamma}$ hermitian. Note that \mathbf{R} is not hermitian: this is a consequence of the possible decay channels of the P^0 and \bar{P}^0 mesons. While \mathbf{M} encodes the $P^0 - \bar{P}^0$ oscillations via virtual intermediate states, $\mathbf{\Gamma}$ concerns transitions mediated by physical states to which both P^0 and \bar{P}^0 decay.

The phenomenological constraints coming from meson mixing that we will focus on are the mass splittings Δm between the heavy P_h and light P_l meson states and the CP violating parameter ϵ_K stemming from the decays of neutral kaons to two pions. These values are approximately given by:

$$\Delta m \approx 2|\mathbf{M}_{12}| + (\Delta m)_{\text{LD}}, \quad (5.6)$$

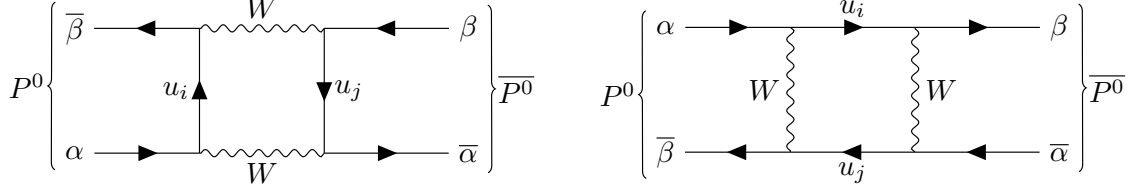


Figure 5.1: Leading order contribution to $P^0 - \overline{P^0}$ mixing, where $u_i, u_j = u, c, t, T$. The K^0 , B_d^0 and B_s^0 mesons correspond to $(\alpha, \beta) = (d, \bar{s}), (d, \bar{b}), (s, \bar{b})$.

$$|\epsilon_K| \approx \frac{k_\epsilon}{\sqrt{2}\Delta m_K} |\text{Im}(M_{12}^K)|. \quad (5.7)$$

In Eq. (5.6), $(\Delta m)_{\text{LD}}$ encompasses the long-distance contributions to the mass splitting, whose theoretical calculation is not known to date. Thus, we constrain our model by demanding that the short-distance physics does not saturate the experimental bounds.

In the SM, the leading order contribution to $P^0 - \overline{P^0}$ mixing is given by the box diagrams presented in Fig. 5.1, where the internal up-type quarks are $u_i, u_j = u, c, t$. The inclusion of the up isosinglet VLQ does not lead to FCNC in the down sector. Thus, our model presents a simple NP contribution to the SM box diagram via the introduction of the T quark in the internal quarks.

The calculation of the effective Hamiltonian generating these diagrams is performed in Ref. [105] in the limit of vanishing external masses:

$$\mathcal{H}_{\text{eff.}} = \frac{G_F^2 m_W^2}{4\pi^2} (\overline{\beta}_L \gamma^\mu \alpha_L) (\overline{\beta}_L \gamma_\mu \alpha_L) \sum_{i,j=u,c,t,T} \lambda_{\beta\alpha}^i \lambda_{\beta\alpha}^j F(x_\alpha, x_\beta), \quad (5.8)$$

where the Inami-Lim function $F(x_\alpha, x_\beta)$ encodes the meson mixing dependence on the internal quark masses and m_W in the loop. In the SM, this expression is further simplified through the unitarity of \mathbf{V}_{CKM} , together with the approximation $x_u \approx 0$. Recalling the analysis done at end of Sec. 3.3, although \mathbf{V} in our model is not unitary, it retains orthonormality with respect to its columns, allowing to perform the exact same simplification performed in the SM:

$$\mathbf{V}^\dagger \mathbf{V} = \mathbb{1}_{3 \times 3} \implies \lambda_{\beta\alpha}^u = - \sum_{i=c,t,T} \lambda_{\beta\alpha}^i, \quad (5.9)$$

This allows us to write Eq. (5.8) in the usual way:

$$\mathcal{H}_{\text{eff.}} = \frac{G_F^2 m_W^2}{4\pi^2} (\overline{\beta}_L \gamma^\mu \alpha_L) (\overline{\beta}_L \gamma_\mu \alpha_L) \sum_{i,j=c,t,T} \lambda_{\beta\alpha}^i \lambda_{\beta\alpha}^j S_0(x_\alpha, x_\beta), \quad (5.10)$$

We are now ready to compute \mathbf{M}_{12} , which is given by:

$$\mathbf{M}_{12} = \langle P^0 | \mathcal{H}_{\text{eff.}} | \overline{P^0} \rangle. \quad (5.11)$$

The determination of the hadronic matrix element $\langle P^0 | (\overline{\beta}_L \gamma^\mu \alpha_L) (\overline{\beta}_L \gamma_\mu \alpha_L) | \overline{P^0} \rangle$ is yet another calculation plagued by theoretical limitations. Hence, this computation is performed using the vacuum-insertion

approximation (VIA) yielding:

$$\langle P^0 | (\overline{\beta_L} \gamma^\mu \alpha_L) (\overline{\beta_L} \gamma_\mu \alpha_L) | \overline{P^0} \rangle_{\text{VIA}} = \frac{1}{3} f^2 m, \quad (5.12)$$

where f and m are the decay and mass values for P_0 and we defined $\mathcal{CP}|P^0\rangle = -|\overline{P^0}\rangle$. A B factor, commonly known as bag parameter, is usually included in Eq. (5.12) to correct the VIA value, leading to the final expression:

$$\mathbf{M}_{12} = \frac{G_F^2 m_W^2}{12\pi^2} B f^2 m \sum_{i,j=c,t,T} \eta_{ij} \lambda_{\beta\alpha}^i \lambda_{\beta\alpha}^j S_0(x_\alpha, x_\beta) = \frac{G_F^2 m_W^2}{12\pi^2} B f^2 m (\Delta_{\text{SM}}^{P^0} + \Delta_{\text{NP}}^{P^0}), \quad (5.13)$$

where η_{ij} are QCD correction factors. The sum may be factorized into a SM ($\Delta_{\text{SM}}^{P^0}$) and a NP ($\Delta_{\text{NP}}^{P^0}$) part:

$$\begin{aligned} \Delta_{\text{SM}}^{P^0} &= \eta_{cc}^P S_0(x_c) (\lambda_{\beta\alpha}^c)^2 + \eta_{tt}^P S_0(x_t) (\lambda_{\beta\alpha}^t)^2 + 2\eta_{ct}^P S_0(x_c, x_t) \lambda_{\beta\alpha}^c \lambda_{\beta\alpha}^t, \\ \Delta_{\text{NP}}^{P^0} &= \eta_{TT}^P S_0(x_T) (\lambda_{\beta\alpha}^T)^2 + 2 [\eta_{cT}^P S_0(x_c, x_T) \lambda_{\beta\alpha}^c \lambda_{\beta\alpha}^T + \eta_{tT}^P S_0(x_t, x_T) \lambda_{\beta\alpha}^t \lambda_{\beta\alpha}^T]. \end{aligned} \quad (5.14)$$

Regarding the $K^0 - \overline{K^0}$ mixing, the long-distance contributions are expected to dominate over the short-distance ones, which unables the computation of Δm_K . Hence, our requirement is that $(\Delta m_K)_{\text{NP}}$ does not saturate the experimental bound. A recent calculation of ϵ_K in the SM [107], where most uncertainties were removed using the unitarity of \mathbf{V}_{CKM} , is in agreement with its experimental observation. Although \mathbf{V} is not unitary, we use this result in order to provide a more restrictive bound on the model, arguing that the CAA currently corresponds to a small unitary deviation $\delta_{\text{CKM}} = 1.7 \times 10^{-3}$. These considerations translates on the following bounds using the values in Table 5.2:

$$2 \left| \left(\mathbf{M}_{12}^K \right)_{\text{NP}} \right| < (\Delta m_K)_{\text{exp}} \Rightarrow |\Delta_{\text{NP}}^{K^0}| < (2.714 \pm 0.091) \times 10^{-5}, \quad (5.15)$$

$$\frac{k_\epsilon}{\sqrt{2}(\Delta m_K)_{\text{exp}}} \left| \text{Im} \left(\mathbf{M}_{12}^K \right)_{\text{NP}} \right| < |(\epsilon_K)_{\text{exp}}| - |(\epsilon_K)_{\text{SM}}| \Rightarrow |\text{Im}(\Delta_{\text{NP}}^{K^0})| < (0.567 \pm 1.505) \times 10^{-8}. \quad (5.16)$$

Contrary to the neutral kaon mixing, the long-distance effects on the $B_{d,s}^0 - \overline{B_{d,s}^0}$ systems is negligible, allowing a precise theoretical calculation of its parameters. In Ref. [108], a model independent statistical analysis for $B_{d,s}^0 - \overline{B_{d,s}^0}$ imposes the following limits:

$$\text{Re} \left(\Delta_{\text{NP}}^{B_d} / \Delta_{\text{SM}}^{B_d} \right) = -0.18 \pm 0.14, \quad (5.17)$$

$$\text{Im} \left(\Delta_{\text{NP}}^{B_d} / \Delta_{\text{SM}}^{B_d} \right) = -0.199 \pm 0.062, \quad (5.18)$$

$$\text{Re} \left(\Delta_{\text{NP}}^{B_s} / \Delta_{\text{SM}}^{B_s} \right) = -0.03 \pm 0.13, \quad (5.19)$$

$$\text{Im} \left(\Delta_{\text{NP}}^{B_s} / \Delta_{\text{SM}}^{B_s} \right) = 0.0 \pm 0.1, \quad (5.20)$$

where the SM and NP contributions are given by:

$$\begin{aligned} \Delta_{\text{NP}}^{B_q} &= \eta_{TT}^{B_q} S_0(x_T) (\lambda_{qb}^T)^2 + 2\eta_{Tt}^{B_q} S_0(x_t, x_T) \lambda_{qb}^T \lambda_{qb}^t, \\ \Delta_{\text{SM}}^{B_q} &= \eta_{tt}^{B_q} S_0(x_t) (\lambda_{qb}^t)^2. \end{aligned} \quad (5.21)$$

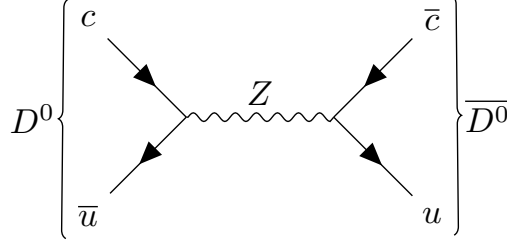


Figure 5.2: $D^0 - \overline{D^0}$ mixing via a tree level Z mediated FCNC.

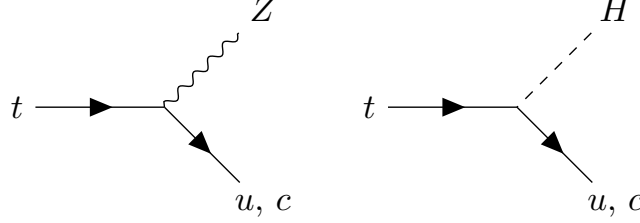


Figure 5.3: Tree-level decay of the top quark via Z and Higgs mediated FCNC.

Inspecting Table 4.1, we observe that $|\lambda_{qb}^c| \approx |\lambda_{qb}^t|$ for $q = d, s$. This, together with $S_0(x_c) < S_0(x_c, x_t) \ll S_0(x_t)$ allows us to ignore the charm contribution to $B_{d,s}^0$ meson oscillations.

Finally, we discuss the $D^0 - \overline{D^0}$ mixing. In the SM, box diagrams similar to Fig. 5.1 contribute to the mixing, where the external quarks are the valence quarks u, c of the charmed neutral meson D^0 and the internal quarks are the down-type quarks. However, it is expected that the long-distance effects dominate the mixing [109]. Hence, following the requirement for the kaon mixing, we impose that the NP contribution to Δm_D does not saturate the experimental bound. In our model, the existence of FCNC in the up-quark sector leads to a Z and Higgs mediated tree-level contribution to $D^0 - \overline{D^0}$ mixing, presented in Fig. 5.2. Note that the Higgs-mediated diagram provides no contribution in the limit of vanishing external masses. In this case, $(\mathbf{M}_{12})_{\text{NP}}$ is similar to the one presented in Eq. (5.13), since this diagram presents the vector current $(\overline{u}_L \gamma^\mu c_L)(\overline{c}_L \gamma_\mu u_L)$, where the NP effects are given by:

$$\Delta_{\text{NP}}^{D^0} = \frac{4\pi s_W^2}{\alpha_{\text{em}}} \eta^D (\mathbf{F}_{cu}^u)^2,$$

resulting in a direct bound to \mathbf{F}_{cu}^u :

$$(\Delta m_D)_{\text{NP}} = 2 |(M_{12}^D)_{\text{NP}}| < (\Delta m_D)_{\text{exp.}} \Rightarrow |\mathbf{F}_{cu}^u|^2 < (2.140 \pm 1.181) \times 10^{-8}. \quad (5.22)$$

5.1.2 Rare top decays

The top decays $t \rightarrow Z(u, c)$ and $t \rightarrow H(u, c)$ are heavily suppressed in the SM [112]. With the addition of the up VLQ, FCNC lead to the tree-level contributions displayed in Fig. 5.3 which must be controlled.

$K^0 - \bar{K}^0$			
B_K	$0.717 \pm 0.018(\text{stat.}) \pm 0.016(\text{syst.})$ [73]	f_K	155.7 ± 0.3 MeV [73]
m_K	497.611 ± 0.013 MeV [37]	η_{ct}^K	0.47 ± 0.04 [103]
η_{tt}^K	0.57 ± 0.01 [103]	k_ϵ	0.92 ± 0.02 [110]
$ \epsilon_{K_{\text{SM}}} $	$(2.16 \pm 0.18) \times 10^{-3}$ [107]	$ \epsilon_{K_{\text{exp}}} $	$(2.228 \pm 0.011) \times 10^{-3}$ [37]
Δm_K	$(3.484 \pm 0.006) \times 10^{-12}$ MeV [37]		
$B_{d(s)}^0 - \bar{B}_{d(s)}^0$			
η^B	0.55 [111]		
$D^0 - \bar{D}^0$			
B_D	1 ± 0.3 [104]	f_D	212.0 ± 0.7 MeV [73]
m_D	1864.84 ± 0.05 MeV [37]	η^D	0.59 [104]
Δm_D	$(6.562 \pm 0.764) \times 10^{-12}$ MeV [37]		

Table 5.2: Numerical values used in meson mixing calculations.

Rare top decays			
$\text{Br}(t \rightarrow Zu)$	$< 1.7 \times 10^{-3}$ [37]	$\text{Br}(t \rightarrow Zc)$	$< 2.4 \times 10^{-3}$ [37]
$\text{Br}(t \rightarrow Hu)$	$< 1.9 \times 10^{-4}$ [37]	$\text{Br}(t \rightarrow Hc)$	$< 7.3 \times 10^{-4}$ [37]

Table 5.3: Numerical values used in rare top decays calculations.

The branching ratios (BR) for these decays are approximately given by [33]:

$$\text{Br}(t \rightarrow Zq) \approx \frac{\Gamma(t \rightarrow Zq)}{\Gamma(t \rightarrow Wb)} \approx \frac{1 - 3r_Z^4 + 2r_Z^6}{1 - 3r_W^4 + 2r_W^6} \frac{|\mathbf{F}_{tq}^u|^2}{2|\mathbf{V}_{tb}|^2}, \quad (5.23)$$

$$\text{Br}(t \rightarrow Hq) \approx \frac{\Gamma(t \rightarrow Hq)}{\Gamma(t \rightarrow Wb)} \approx \frac{(1 - r_h^2)^2}{1 - 3r_W^4 + 2r_W^6} \frac{|\mathbf{F}_{tq}^u|^2}{2|\mathbf{V}_{tb}|^2}, \quad (5.24)$$

where $r_i = m_i/m_t$ and we use the fact that $\text{Br}(t \rightarrow Wb) \approx 1$. These equations translate into the following bounds:

$$\begin{aligned} Z \text{ bounds : } |\mathbf{F}_{tu}^u| &< (1.920 \pm 0.056) \times 10^{-2}, \quad |\mathbf{F}_{tc}^u| < (2.281 \pm 0.066) \times 10^{-2}, \\ H \text{ bounds : } |\mathbf{F}_{tu}^u| &< (3.854 \pm 0.112) \times 10^{-2}, \quad |\mathbf{F}_{tc}^u| < (7.554 \pm 0.219) \times 10^{-2}, \end{aligned} \quad (5.25)$$

where we consider $|\mathbf{V}_{tb}| = 0.999^1$. From Eq. (5.25), it is clear that the current experimental constraints stemming from Z mediated top decays result in more restrictive bounds for FCNC than H mediated decays.

5.1.3 Rare meson decays

In this subsection we focus on rare K and B meson decays, namely the leptonic decays $B_{d,s}^0 \rightarrow \mu^+ \mu^-$ and $K_L \rightarrow \mu^+ \mu^-$ and the semileptonic decays $K^+ \rightarrow \pi^+ \nu \bar{\nu}$ and $K_L \rightarrow \pi^0 \nu \bar{\nu}$. We discuss these decay modes simultaneously since they present a similar structure. In the SM, these processes receive contributions from the diagrams represented in Figs. 5.4, 5.5 and 5.6. The general effective Hamiltonian describing

¹This $|\mathbf{V}_{tb}|$ value is obtained in all the best fit values presented in Sec 5.2.

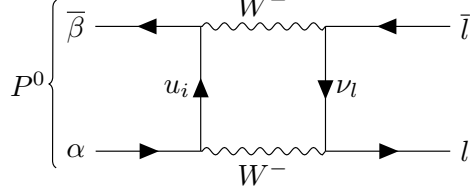


Figure 5.4: SM box diagram contributing to leptonic decays in unitary gauge. The semileptonic decay box is similar, with external neutrinos and the corresponding internal lepton.

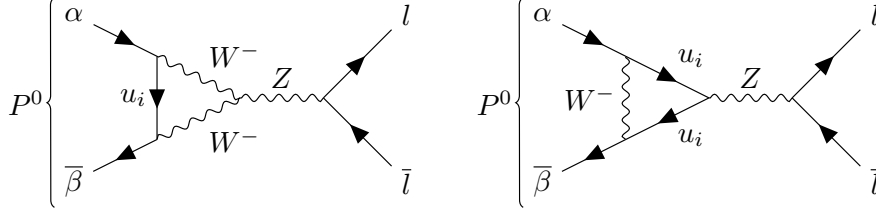


Figure 5.5: SM Z-mediated penguin diagrams for leptonic and semileptonic decays in unitary gauge.

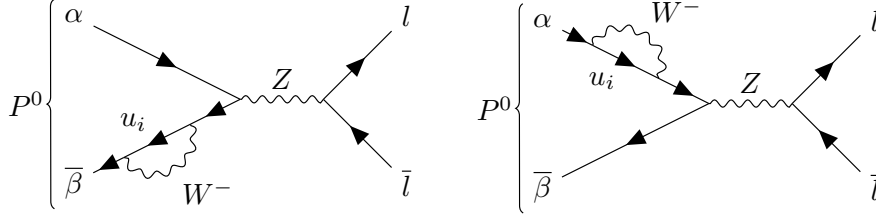


Figure 5.6: Self-energy diagrams inducing flavour-changing contributing to leptonic and semileptonic decays in unitary gauge.

these decays is given by:

$$\mathcal{H}_{\text{eff.}} = \frac{G_F}{\sqrt{2}} \frac{\alpha_{\text{em.}}}{2\pi s_W^2} [\bar{\beta} \gamma^\mu (1 - \gamma_5) \alpha] [\bar{l} \gamma_\mu (1 - \gamma_5) l] [\lambda_{\beta\alpha}^c F_{\text{IL}}(x_c) + \lambda_{\beta\alpha}^t F_{\text{IL}}(x_t)], \quad (5.26)$$

where F_{IL} is one of the Inami-Lim functions $X_0(x)$ or $Y_0(x)$. This expression once again employs $x_u \approx 0$ and eliminates the dependence on the u quark through the condition $\lambda_{\beta\alpha}^u = -\sum_{i=c,t} \lambda_{\beta\alpha}^i$. The decays considered here allow precise theoretical calculations, since the hadronic matrix elements required can be extracted by leading (nonrare) semileptonic decays, with other long distance physics being negligibly small². Thus, these processes are dominated by short-distance contributions [103].

In an arbitrary gauge, we must consider the diagrams where the W^\pm bosons are replaced by the corresponding ϕ^\pm Goldstone bosons. The Inami-Lim functions are computed in the limit of vanishing external masses. Hence, the box diagrams with at least one Goldstone boson do not contribute to leptonic decays [102]. As a consequence, the leptonic and semileptonic decays receive distinct contributions from the box diagram: the leptonic decays are controlled at leading order by $Y_0(x) = C(x) - B(x)$, while the semileptonic decays depend on $X_0(x) = C(x) - 4B(x)$. Note that the functions $B(x)$ and $C(x)$ originating

²This is not true for $K_L \rightarrow \mu^+ \mu^-$ in general. However, we focus only on the short distance contributions to this process. The main difficulty for phenomenological applications for this decay mode is the separation of the short and long distance contribution in the measured rate [103].

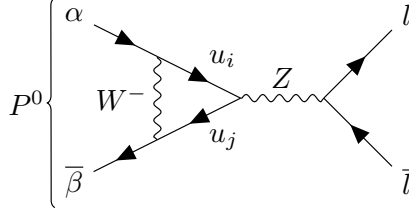


Figure 5.7: NP penguin diagram with tree-level FCNC induced by the Z -boson in unitary gauge. The internal quarks are u_i , $u_j = u, c, t, T$.

from the box diagram and Z penguin and self-energy diagrams, respectively, are gauge-dependent, while the Inami-Lim functions $Y_0(x)$ and $X_0(x)$ are gauge invariant.

The inclusion of an up-type isosinglet VLQ introduces NP contributions in two distinct ways. Firstly, the straightforward NP contribution is analogous to what was described concerning the meson mixing: the orthonormality of the columns of \mathbf{V} allows to rewrite Eq. (5.26) by simply introducing a $\lambda_{\beta\alpha}^T F_{\text{IL}}(x_T)$. This contribution stems from introducing the T quark in the internal quarks u_i in the Figs. 5.4, 5.5 and 5.6. The second contribution stems from tree-level FCNC involving the up-quark sector. The Z -mediated penguin diagram presented in Fig. 5.5 is modified due to a possible flavour change in the internal u_i quark running in the loop, as is represented in Fig. 5.7. This contribution is given by [33, 113–116]:

$$\Delta_{\text{NP}}^{\text{pen.}} = \sum_{i,j=u,c,t,T} \mathbf{V}_{i\beta}^* (\mathbf{F}_{ij}^u - \delta_{ij}) \mathbf{V}_{j\alpha} N(x_i, x_j), \quad (5.27)$$

where the loop function $N(x_i, x_j)$ is written in Appendix B. Note that the NP effect $\Delta_{\text{NP}}^{\text{pen.}}$ restores the VLQ decoupling for large m_T . In the absence of this term, we obtain, in the limit of large VLQ mass ($x_T \gg 1$):

$$\begin{aligned} Y_0(x_T) &\underset{x_T \gg 1}{\approx} \frac{x_T}{8} + \frac{3}{8} \log x, \\ X_0(x_T) &\underset{x_T \gg 1}{\approx} \frac{x_T}{8} + \frac{3}{8} \log x. \end{aligned} \quad (5.28)$$

Recalling Eq. (3.23), in the decoupling limit, i.e. $x_T \gg 1$ and considering negligible mixing between the up-VLQ and SM quarks, we obtain,

$$\mathbf{F}_u - \mathbb{1}_{4 \times 4} = - \begin{pmatrix} 0_{3 \times 3} & 0_{3 \times 1} \\ 0_{1 \times 3} & 1 \end{pmatrix}, \quad (5.29)$$

and $N(x_T, x_T) = N(x_T) = \frac{x_T}{8}$, leading to,

$$\Delta_{\text{NP}}^{\text{pen.}} \approx -\lambda_{\beta\alpha}^T \frac{x_T}{8}. \quad (5.30)$$

When we take into account $\Delta_{\text{NP}}^{\text{pen.}}$, we reduce the linear behaviour of $Y_0(x_T)$ and $X_0(x_T)$ to a logarithmic one,

$$\begin{aligned} X_0(x_T) &\rightarrow X_0(x_T) - \frac{x_T}{8} \underset{x_T \gg 1}{\approx} \frac{3}{8} (1 + \log x), \\ Y_0(x_T) &\rightarrow Y_0(x_T) - \frac{x_T}{8} \underset{x_T \gg 1}{\approx} \frac{3}{8} (-1 + \log x), \end{aligned} \quad (5.31)$$

restoring the decoupling for large VLQ mass.

We now write the set of equations relevant to constrain our model. We extract these from Ref. [33]. The leptonic decays $B_{d,s}^0 \rightarrow \mu^+ \mu^-$ and $K_L \rightarrow \mu^+ \mu^-$ yield:

$$\text{Br}(B_q^0 \rightarrow \mu^+ \mu^-) = \tau_{B_q} \frac{G_F^2}{16\pi} \left(\frac{\alpha_{\text{em}}}{\pi s_W^2} \right)^2 f_{B_q}^2 m_{B_q} m_\mu^2 \sqrt{1 - \frac{4m_\mu^2}{m_{B_q}^2}} |\eta_Y^2| |\lambda_{qb}^t Y_0(x_t) + \Delta_{\mu\mu}^{B_q}|^2, \quad (5.32)$$

$$\frac{\text{Br}(K_L \rightarrow \mu^+ \mu^-)_{\text{SD}}}{\text{Br}(K^+ \rightarrow \mu^+ \nu)} = \frac{\tau_{K_L}}{\tau_{K^+}} \frac{\alpha_{\text{em}}^2}{\pi^2 s_W^4 |\mathbf{V}_{us}|^2} [Y_{NL} \text{Re} \lambda_{sd}^c + \eta_t^Y Y_0(x_t) \text{Re} \lambda_{sd}^t + \Delta_{\mu\mu}^{K_L}]^2, \quad (5.33)$$

where the NP contributions are given by:

$$\Delta_{\mu\mu}^{B_q} = \lambda_{qb}^T Y_0(x_T) + \sum_{i,j=u,c,t,T} \mathbf{V}_{iq}^* (\mathbf{F}_{ij}^u - \delta_{ij}) \mathbf{V}_{jb} N(x_i, x_j), \quad (5.34)$$

$$\Delta_{\mu\mu}^{K_L} = \eta_T^Y Y_0(x_T) \text{Re} \lambda_{sd}^T + \sum_{i,j=u,c,t,T} \eta_i^Y \text{Re} [\mathbf{V}_{is}^* (\mathbf{F}_{ij}^u - \delta_{ij}) \mathbf{V}_{jd}] N(x_i, x_j). \quad (5.35)$$

Employing the values in Table 5.3, these equations impose the bounds:

$$|\lambda_{db}^t Y_0(x_t) + \Delta_{\mu\mu}^{B_d}|^2 = (5.107 \pm 9.484) \times 10^{-5}, \quad (5.36)$$

$$|\lambda_{sb}^t Y_0(x_t) + \Delta_{\mu\mu}^{B_s}|^2 = (1.469 \pm 0.171) \times 10^{-3}, \quad (5.37)$$

$$\frac{1}{|\mathbf{V}_{us}|^2} [Y_{NL} \text{Re} \lambda_{sd}^c + \eta_t^Y Y_0(x_t) \text{Re} \lambda_{sd}^t + \Delta_{\mu\mu}^{K_L}]^2 < (9.430 \pm 0.045) \times 10^{-6}. \quad (5.38)$$

Focusing now on the semileptonic decays $K^+ \rightarrow \pi^+ \nu \bar{\nu}$ and $K_L \rightarrow \pi^0 \nu \bar{\nu}$, we obtain the following conditions:

$$\frac{\text{Br}(K^+ \rightarrow \pi^+ \nu \bar{\nu})}{\text{Br}(K^+ \rightarrow \pi^0 e^+ \bar{\nu})} = \frac{\alpha_{\text{em}}^2 r_{K^+}}{2\pi^2 s_W^4 |\mathbf{V}_{us}|^2} \sum_{l=e,\mu,\tau} |\lambda_{sd}^c X_{NL}^l + \lambda_{sd}^t \eta_t^X X_0(x_t) + \Delta_{\pi\nu\nu}^K|^2, \quad (5.39)$$

$$\frac{\text{Br}(K_L \rightarrow \pi^0 \nu \bar{\nu})}{\text{Br}(K_L \rightarrow \pi^0 \nu \bar{\nu})_{\text{SM}}} = \left| \frac{\text{Im} [\lambda_{sd}^c X_0(x_c) + \lambda_{sd}^t X_0(x_t) + \Delta_{\pi^0 \nu \bar{\nu}}^{K_L}]}{\text{Im} [\lambda_{sd}^c X_0(x_c) + \lambda_{sd}^t X_0(x_t)]} \right|^2, \quad (5.40)$$

where,

$$\Delta_{\pi\nu\nu}^K = \eta_T^X \lambda_{sd}^T X_0(x_T) + \sum_{i,j=u,c,t,T} \eta_i^X \mathbf{V}_{is}^* (\mathbf{F}_{ij}^u - \delta_{ij}) \mathbf{V}_{jd} N(x_i, x_j), \quad (5.41)$$

$$\Delta_{\pi^0 \nu \bar{\nu}}^{K_L} = \lambda_{sd}^T X_0(x_T) + \sum_{i,j=u,c,t,T} \mathbf{V}_{is}^* (\mathbf{F}_{ij}^u - \delta_{ij}) \mathbf{V}_{jd} N(x_i, x_j). \quad (5.42)$$

Finally, the semileptonic decays impose the following bounds in our model:

$$\frac{1}{|\mathbf{V}_{us}|^2} \sum_{l=e,\mu,\tau} |\lambda_{sd}^c X_{NL}^l + \lambda_{sd}^t \eta_t^X X_0(x_t) + \Delta_{\pi\nu\nu}^K|^2 = (4.945 \pm 1.736) \times 10^{-5}, \quad (5.43)$$

$$\left| \frac{\text{Im} [\lambda_{sd}^c X_0(x_c) + \lambda_{sd}^t X_0(x_t) + \Delta_{\pi^0 \nu \bar{\nu}}^{K_L}]}{\text{Im} [\lambda_{sd}^c X_0(x_c) + \lambda_{sd}^t X_0(x_t)]} \right|^2 < (1.0 \pm 0.2) \times 10^2. \quad (5.44)$$

$B_d \rightarrow \mu^+ \mu^-$			
m_{B_d}	$5279.66 \pm 0.12 \text{ MeV}$ [37]	τ_{B_d}	$(1.519 \pm 0.004) \times 10^{-12} \text{ s}$ [37]
$\text{Br}(B_d \rightarrow \mu^+ \mu^-)$	$7_{-11}^{+13} \times 10^{-11}$ [37]	f_{B_d}	$190.0 \pm 1.3 \text{ MeV}$ [73]
η_Y	1.0113 [117]		
$B_s \rightarrow \mu^+ \mu^-$			
m_{B_s}	$5366.92 \pm 0.10 \text{ MeV}$ [37]	τ_{B_s}	$(1.520 \pm 0.005) \times 10^{-12} \text{ s}$ [37]
$\text{Br}(B_s \rightarrow \mu^+ \mu^-)$	$(3.01 \pm 0.35) \times 10^{-9}$ [37]	f_{B_s}	$230.3 \pm 1.3 \text{ MeV}$ [73]
$\text{Br}(K^+ \rightarrow \pi^+ \nu \bar{\nu})/\text{Br}(K^+ \rightarrow \pi^0 e^+ \bar{\nu})$			
$\text{Br}(K^+ \rightarrow \pi^+ \nu \bar{\nu})$	$(1.14_{-0.33}^{+0.40}) \times 10^{-10}$ [37]	$\text{Br}(K^+ \rightarrow \pi^0 e^+ \bar{\nu})$	$(5.07 \pm 0.04) \times 10^{-2}$ [37]
r_{K^+}	0.901 [118]	$X_{\text{NL}}^{e,\mu}$	$(10.6 \pm 1.5) \times 10^{-4}$ [33, 119]
X_{NL}^τ	$(7.1 \pm 1.4) \times 10^{-4}$ [33, 119]	η_t^X	0.994 [111, 119]
$\text{Br}(K_L \rightarrow \mu^+ \mu^-)_{\text{SD}}/\text{Br}(K^+ \rightarrow \mu^+ \nu)$			
$\text{Br}(K_L \rightarrow \mu^+ \mu^-)_{\text{SD}}$	$< 2.5 \times 10^{-9}$ [120]	$\text{Br}(K^+ \rightarrow \mu^+ \nu)$	(0.6356 ± 0.0011) [37]
τ_{K^+}	$(1.2380 \pm 0.0020) \times 10^{-8} \text{ s}$ [37]	τ_{K_L}	$(5.116 \pm 0.021) \times 10^{-8} \text{ s}$ [37]
η_t^Y	1.012 [111, 119]	Y_{NL}	$(2.94 \pm 0.28) \times 10^{-4}$ [33, 119]
$\text{Br}(K_L \rightarrow \pi^0 \bar{\nu} \nu)/\text{Br}(K_L \rightarrow \pi^0 \bar{\nu} \nu)_{\text{SM}}$			
$\text{Br}(K_L \rightarrow \pi^0 \bar{\nu} \nu)_{\text{SM}}$	$(3.0 \pm 0.6) \times 10^{-11}$ [121]	$\text{Br}(K_L \rightarrow \pi^0 \bar{\nu} \nu)$	$< 3.0 \times 10^{-9}$ [37]

Table 5.4: Numerical values used in meson decays calculations.

5.1.4 CP violation parameter ϵ'/ϵ

CP violation was first observed in kaon decays to two pion states in 1964 [122]. The final states $\pi^+ \pi^-$ and $\pi^0 \pi^0$ are CP-even states. Hence, if CP was conserved, the neutral meson K_L , which is CP-odd, would not decay into two pions.

CP violation in the neutral kaon system is described by the ϵ and ϵ' parameters. In the SM, the ratio ϵ/ϵ' receives contributions not only from the diagrams in Figs. 5.4, 5.5 and 5.6, where the final state is a quark-antiquark pair, but also the diagrams where the Z boson is replaced by a photon or a gluon. Note that only the right diagram of Fig. 5.5 has an analogous gluon mediated penguin diagram, since there is no interaction vertex between the W^- boson and a gluon. The electromagnetic and gluonic penguin and self-energy contributions to ϵ/ϵ' lead to the Inami-Lim functions $D_0(x)$ and $E_0(x)$, respectively (see Appendix B). The $D_0(x)$ function is gauge-dependent, contrary to $E_0(x)$ [123]. Following the procedure in Sec. 5.1.3, the gauge dependent $C_0(x)$, $B_0(x)$ and $D_0(x)$ are rewritten in the gauge independent basis $X_0(x)$, $Y_0(x)$ and $Z_0(x) = C_0(x) + 1/4 D_0(x)$. Finally, the SM contribution to the ratio ϵ/ϵ' is:

$$\Delta_{\epsilon'}^{\text{SM}} = F_{\epsilon'}(x_t) \text{Im } \lambda_{sd}^t, \quad (5.45)$$

where we define the function

$$F_{\epsilon'}(x) = P_0 + P_X X_0(x) + P_Y Y_0(x) + P_Z Z_0(x) + P_E E_0(x), \quad (5.46)$$

ϵ'/ϵ			
$B_6^{(1/2)}(1.3 \text{ GeV})$	1.36 ± 0.23 [124]	$B_8^{(3/2)}(1.3 \text{ GeV})$	0.79 ± 0.05 [124]
ϵ'/ϵ	$(1.66 \pm 0.23) \times 10^{-3}$ [37]		

Table 5.5: Numerical values used in ϵ'/ϵ calculations.

with coefficients

$$P_0 = -3.167 + 12.409 B_6^{1/2} + 1.262 B_8^{1/2}, \quad (5.47)$$

$$P_X = 0.540 + 0.023 B_6^{1/2}, \quad (5.48)$$

$$P_Y = 0.387 + 0.088 B_6^{1/2}, \quad (5.49)$$

$$P_Z = 0.474 - 0.017 B_6^{1/2} - 10.186 B_8^{1/2}, \quad (5.50)$$

$$P_E = 0.188 - 1.399 B_6^{1/2} + 0.459 B_8^{1/2}. \quad (5.51)$$

In our model, the inclusion of the up VLQ results in the extension of the SM contribution by adding the T quark to the internal up quarks in the loops of the diagrams. Moreover, the diagram represented in Fig. 5.7 resulting from the FCNC modifies the contribution coming from the penguin diagrams, which is related to the $C_0(x)$ function, and, therefore, to the functions $X_0(x)$, $Y_0(x)$ and $Z_0(x)$. Hence, the full expression for the ϵ/ϵ' is:

$$\epsilon'/\epsilon = \Delta_{\epsilon'}^{\text{NP}} + \Delta_{\epsilon'}^{\text{SM}}, \quad (5.52)$$

where,

$$\Delta_{\epsilon'}^{\text{NP}} = F_{\epsilon'}(x_T) \text{Im}(\lambda_{sd}^T) + (P_X + P_Y + P_Z) \sum_{i,j=u,c,t,T} \text{Im} [\mathbf{V}_{is}^* (\mathbf{F}_{ij}^u - \delta_{ij}) \mathbf{V}_{jd} N(x_i, x_j)]. \quad (5.53)$$

Following [104], we assume that the P coefficients entering $\Delta_{\epsilon'}^{\text{NP}}$ are identical to the corresponding ones in $\Delta_{\epsilon'}^{\text{SM}}$.

5.2 Results

We begin this section verifying if the best fit points presented in Table 4.10 are consistent with the phenomenological implications discussed previously. We list below, for each texture pair, the process which presents the strongest disagreement between its theoretical value and experimental bound:

$$(9_9^u, 5_1^d): D^0 - \overline{D^0} \text{ mixing} \rightarrow |\mathbf{F}_{uc}^u|^2 = 1.33 \times 10^{-7} > (2.140 \pm 1.181) \times 10^{-8}, \quad (5.54)$$

$$(9_9^u, 5_3^d): D^0 - \overline{D^0} \text{ mixing} \rightarrow |\mathbf{F}_{uc}^u|^2 = 4.48 \times 10^{-6} > (2.140 \pm 1.181) \times 10^{-8}, \quad (5.55)$$

$$(9_9^u, 5_1^s): D^0 - \overline{D^0} \text{ mixing} \rightarrow |\mathbf{F}_{uc}^u|^2 = 2.95 \times 10^{-6} > (2.140 \pm 1.181) \times 10^{-8}, \quad (5.56)$$

$$(9_9^u, 5_3^s): D^0 - \overline{D^0} \text{ mixing} \rightarrow |\mathbf{F}_{uc}^u|^2 = 1.33 \times 10^{-7} > (2.140 \pm 1.181) \times 10^{-8}, \quad (5.57)$$

$$(9_9^u, 5_1^b) : B_s \rightarrow \mu^+ \mu^- \text{ decay} \rightarrow |\lambda_{sb}^t Y_0(x_t) + \Delta_{\mu\mu}^{B_s}|^2 = 1.843 \times 10^{-3} \Leftrightarrow \chi^2 = 4.78, \quad (5.58)$$

$$(9_9^u, 5_3^b) : K^0 - \overline{K}^0 \text{ mixing} \rightarrow |\text{Im}(\Delta_{K^0})|^2 = 1.86 \times 10^{-5} > (0.567 \pm 1.505) \times 10^{-8}. \quad (5.59)$$

The texture pairs with the down or strange quarks decoupled present FCNC incompatible with experimental data: the $[(9_9^u, 5_1^d), (9_9^u, 5_3^d)]$ and $[(9_9^u, 5_3^s), (9_9^u, 5_1^s)]$ pairs predict $|\mathbf{F}_{uc}|^2$ (one, two) orders of magnitude above the allowed bound. It is expected that $D^0 - \overline{D}^0$ mixing provides the most restrictive flavour phenomenology: our model only provides tree-level contributions to D^0 meson oscillations and rare top decays. However, the current experimental bounds for the top decays [check Table 5.3 and Eq. (5.24)] are too permissive to restrain the model. Interestingly, the best fit points for the texture pairs with a decoupled b quark lead to negligible $|\mathbf{F}_{uc}|$. Nonetheless, the pair $(9_9^u, 5_3^b)$ is incompatible with the constraint originating from the ϵ_K bound, presenting a value for $|\text{Im}(\Delta_{K^0})|$ inconsistent at three orders of magnitude. The remaining pair $(9_9^u, 5_1^b)$ presents a disagreement with the $B_s^0 \rightarrow \mu^+ \mu^-$ data at $\chi^2 = 4.78$. Comparing this value to the SM theoretical prediction $|\lambda_{sb}^t Y_0(x_t)|^2 = 1.689 \times 10^{-3}$, obtained using the PDG \mathbf{V}_{CKM} parameterisation [37] as input for Eq. (5.37), and ignoring the NP contributions $\Delta_{\mu\mu}^{B_s}$, that corresponds to $\chi_{\text{SM}}^2 = 1.66$. Thus, we conclude that the best fit value for this texture pair presents no advantage when comparing to the SM, as it worsens data compatibility while not addressing the CAA (recall the discussion at the end of Chapter 4).

5.2.1 Methodology

The incompatibility between the textures pairs presented in Table 4.10 and the flavour phenomenological constraints, may stem from only considering the quark data (see Table 4.1) in the procedure detailed in Sec. 4.3. Thus, we repeat the fit with the modified χ^2 function:

$$\chi^2(x) = \chi_{\text{quark}}^2(x) + \chi_{\text{pheno}}^2(x), \quad (5.60)$$

where χ_{quark}^2 is defined in Eq. (4.1), $x = (x_2, \theta, \mathcal{M}_u)$ are input parameters and we include the flavour phenomenology in $\chi_{\text{pheno}}^2(x)$. In the previous section, we observed that some phenomenological constraints comprise of a definite value, e.g. the Eqs. (5.17), (5.18), (5.19) and (5.20), while others constitute an upper bound, such as Eqs. (5.15) and (5.16), with their corresponding errors. The usual definition for χ_{pheno}^2 is not suitable for the latter case: the model may predict a theoretical value several orders of magnitude below a given experimental upper bound, thus being compatible with experiment, but possibly presenting a high χ_{pheno}^2 value. Furthermore, there is no theoretical motivation for our model to present a value closer to the experimental upper bound. Hence, we establish the following criteria: for phenomenological constraints given by an interval consisting of a central value and corresponding error bar, we employ the usual $\chi^2(x)$ function; for upper bounds, we consider a theoretical value consistent with data if it is within its error bar, i.e. $\chi_{\text{pheno}}^2(x) = 0$ if $P_i(x) < \mathcal{O}_i + \sigma_i$, where $P_i(x)$ is the theoretical prediction of the model for a given experimental upper bound \mathcal{O}_i with associated uncertainty σ_i . In short, the χ_{pheno}^2 for a given

physical process is defined as:

$$\chi_{\text{pheno}}^2 = \sum_i (\chi_{\text{pheno}}^2)_i , \quad (5.61)$$

where

$$(\chi_{\text{pheno}}^2)_i = \frac{[\mathcal{P}_i(x) - \mathcal{O}_i]^2}{\sigma_i^2} \text{ for intervals ,} \quad (5.62)$$

$$(\chi_{\text{pheno}}^2)_i = \begin{cases} \frac{[\mathcal{P}_i(x) - \mathcal{O}_i]^2}{\sigma_i^2} & \text{if } P_i(x) \geq O_i(x) + \sigma_i \\ 0 & \text{if } P_i(x) < O_i(x) + \sigma_i \end{cases} \quad \text{for upper bounds .} \quad (5.63)$$

The texture pairs obtained from this method are organised in Table 5.6. The corresponding mixing \mathbf{V} and FCNC \mathbf{F}^u matrices are displayed in Table 5.7. We note that the arguments exposed at the end of Sec. 4.3 should be valid for this methodology: the only difference is the definition of the χ^2 function employed in the minimisation procedure, which takes into consideration the flavour phenomenology. We observe these textures present the same symmetries as the ones in Table 4.10. This reinforces the validity of the heuristic argument regarding the structure presented by the best fit values for the texture pairs (see discussion at the end of Section 4.3).

	\mathcal{M}_u	\mathbf{M}_d	χ^2
5_1^d	$\begin{pmatrix} 0 & 0 & 32721.3707 & 169555.030 \\ 0 & 78914.1226 & 0 & 1505.34039 \\ 9.62166554 & 0 & 1260.32296 & 0 \\ 0 & 2733123.53 & 0 & 0 \end{pmatrix}$	$\begin{pmatrix} 0 & 0 & 4176.31609 \\ 0 & 4.67 & 0 \\ 93.48239 & 0 & 160.35214 - 71.1036651i \end{pmatrix}$	18.2
5_3^d	$\begin{pmatrix} 0 & 0 & 169544.559 & 32775.5438 \\ 0 & 135249.266 & 0 & 1260.84607 \\ 2.21767698 & 0 & 1505.57998 & 0 \\ 0 & 4689259.33 & 0 & 0 \end{pmatrix}$	$\begin{pmatrix} 0 & 0 & 4176.31651 \\ 0 & 93.48238 & 160.39617 - 70.9794456i \\ 4.67 & 0 & 0 \end{pmatrix}$	21.6
5_1^s	$\begin{pmatrix} 0 & 0 & 29947.7818 & 169928.116 \\ 0 & 31171.9329 & 0 & 7139.64333 \\ 2.2203149 & 0 & 290.619248 & 0 \\ 0 & 1080564.20 & 0 & 0 \end{pmatrix}$	$\begin{pmatrix} 0 & 0 & 4179.83695 \\ 0 & 93.4 & 0 \\ 4.67018 & 0 & 33.76968 + 14.9236726i \end{pmatrix}$	21.9
5_3^s	$\begin{pmatrix} 0 & 0 & 169930.613 & 29932.9180 \\ 0 & 236866.688 & 0 & 290.058338 \\ 9.61532755 & 0 & 7139.47044 & 0 \\ 0 & 8209484.45 & 0 & 0 \end{pmatrix}$	$\begin{pmatrix} 0 & 0 & 4179.83723 \\ 0 & 4.67018 & 33.7336 + 14.9244944i \\ 93.4 & 0 & 0 \end{pmatrix}$	18.1
5_1^b	$\begin{pmatrix} 0 & 0 & 1265.72510 & 7182.42344 \\ 0 & 27.1405285 & 0 & 172540.564 \\ 2.16929313 & 0 & 116.684726 & 0 \\ 0 & 2342998.99 & 0 & 0 \end{pmatrix}$	$\begin{pmatrix} 0 & 0 & 91.4062362 \\ 0 & 4180 & 0 \\ 4.77186260 & 0 & -0.313403888 - 19.16768i \end{pmatrix}$	22.0
5_3^b	$\begin{pmatrix} 0 & 0 & 7193.90089 & 1265.86193 \\ 0 & 4570.26174 & 0 & 116.724231 \\ 564.450806 & 0 & 172539.164 & 0 \\ 0 & 1096156.08 & 0 & 0 \end{pmatrix}$	$\begin{pmatrix} 0 & 0 & 91.4070188 \\ 0 & 4.77182175 & -0.319885530 - 19.16385i \\ 4180 & 0 & 0 \end{pmatrix}$	21.9

Table 5.6: Quark mass matrices identified applying the χ^2 minimisation procedure described in Sec. 5.2 to the maximally-restrictive textures presented in Table 4.8. The subscript $q = d, s, b$ corresponds to the decoupled down quark state. The results are presented in units of MeV.

	\mathbf{V}	\mathbf{F}^u
5_1^d	$\begin{pmatrix} 9.740 \times 10^{-1} & 2.246 \times 10^{-1} & (-0.023 - 3.821j) \times 10^{-3} \\ -2.244 \times 10^{-1} & (9.736 - 0.006j) \times 10^{-1} & (3.797 - 1.658j) \times 10^{-2} \\ 8.552 \times 10^{-3} & (-3.701 - 1.699j) \times 10^{-2} & 9.991 \times 10^{-1} \\ 2.886 \times 10^{-2} & (-3.797 - 1.681j) \times 10^{-8} & 9.884 \times 10^{-7} \end{pmatrix}$	$\begin{pmatrix} 9.992 \times 10^{-1} & 1.822 \times 10^{-4} & -6.972 \times 10^{-6} & 2.811 \times 10^{-2} \\ 1.822 \times 10^{-4} & 9.999 \times 10^{-1} & 1.606 \times 10^{-6} & -6.477 \times 10^{-3} \\ -6.972 \times 10^{-6} & 1.606 \times 10^{-6} & 9.999 \times 10^{-1} & 2.478 \times 10^{-4} \\ 2.811 \times 10^{-2} & -6.477 \times 10^{-3} & 2.478 \times 10^{-4} & 8.330 \times 10^{-4} \end{pmatrix}$
5_3^d	$\begin{pmatrix} 9.743 \times 10^{-1} & 2.250 \times 10^{-1} & (-0.010 - 3.821j) \times 10^{-3} \\ -2.250 \times 10^{-1} & (9.731 - 0.001j) \times 10^{-1} & (3.797 - 1.655j) \times 10^{-2} \\ 8.559 \times 10^{-3} & (-3.702 - 1.696j) \times 10^{-2} & 9.991 \times 10^{-1} \\ 6.288 \times 10^{-13} & (2.880 - 0.002j) \times 10^{-2} & (1.107 - 0.490j) \times 10^{-3} \end{pmatrix}$	$\begin{pmatrix} 0.999 \times 10^{-1} & -1.822 \times 10^{-4} & -2.594 \times 10^{-7} & 6.484 \times 10^{-3} \\ -1.822 \times 10^{-4} & 9.992 \times 10^{-1} & -1.123 \times 10^{-6} & 2.808 \times 10^{-2} \\ -2.594 \times 10^{-7} & -1.123 \times 10^{-6} & 9.999 \times 10^{-1} & 3.997 \times 10^{-5} \\ 6.484 \times 10^{-3} & 2.808 \times 10^{-2} & 3.997 \times 10^{-5} & 8.312 \times 10^{-4} \end{pmatrix}$
5_1^s	$\begin{pmatrix} 9.743 \times 10^{-1} & 2.250 \times 10^{-1} & (-1.583 + 3.478j) \times 10^{-3} \\ (-2.250 - 0.001j) \times 10^{-4} & 9.731 \times 10^{-1} & (-4.141 - 0.080j) \times 10^{-2} \\ (-7.781 + 3.567j) \times 10^{-3} & 4.068 \times 10^{-2} & 9.991 \times 10^{-1} \\ (-2.480 + 1.097j) \times 10^{-7} & 2.884 \times 10^{-2} & 3.072 \times 10^{-5} \end{pmatrix}$	$\begin{pmatrix} 9.999 \times 10^{-1} & -1.822 \times 10^{-4} & -7.818 \times 10^{-6} & 6.489 \times 10^{-3} \\ -1.822 \times 10^{-4} & 9.992 \times 10^{-1} & -3.381 \times 10^{-5} & 2.806 \times 10^{-2} \\ -7.818 \times 10^{-6} & -3.381 \times 10^{-5} & 9.999 \times 10^{-1} & 1.204 \times 10^{-3} \\ 6.489 \times 10^{-3} & 2.806 \times 10^{-2} & 1.204 \times 10^{-3} & 8.316 \times 10^{-4} \end{pmatrix}$
5_3^s	$\begin{pmatrix} 9.740 \times 10^{-1} & 2.246 \times 10^{-1} & (-1.577 + 3.478j) \times 10^{-3} \\ (-2.244 - 0.001j) \times 10^{-1} & 9.736 \times 10^{-1} & (-4.142 - 0.080j) \times 10^{-2} \\ (-7.773 + 3.567j) \times 10^{-3} & 4.072 \times 10^{-2} & 9.991 \times 10^{-1} \\ 2.884 \times 10^{-2} & 6.699 \times 10^{-14} & (2.328 + 1.030j) \times 10^{-4} \end{pmatrix}$	$\begin{pmatrix} 9.992 \times 10^{-1} & 1.822 \times 10^{-4} & -2.358 \times 10^{-7} & 2.809 \times 10^{-2} \\ 1.822 \times 10^{-4} & 9.999 \times 10^{-1} & 5.440 \times 10^{-8} & -6.482 \times 10^{-3} \\ -2.358 \times 10^{-7} & 5.440 \times 10^{-8} & 1.000 & 8.386 \times 10^{-6} \\ 2.809 \times 10^{-2} & -6.482 \times 10^{-3} & 8.386 \times 10^{-6} & 8.318 \times 10^{-4} \end{pmatrix}$
5_1^b	$\begin{pmatrix} 9.743 \times 10^{-1} & 2.251 \times 10^{-1} & 3.821 \times 10^{-3} \\ (0.893 - 2.065j) \times 10^{-1} & (-3.858 + 8.938j) \times 10^{-1} & -4.142 \times 10^{-2} \\ (-0.026 - 8.559j) \times 10^{-3} & (-1.685 + 3.705j) \times 10^{-2} & 9.991 \times 10^{-1} \\ (-0.016 - 5.410j) \times 10^{-10} & (-1.065 + 2.342j) \times 10^{-9} & 1.165 \times 10^{-5} \end{pmatrix}$	$\begin{pmatrix} 1.000 & -6.064 \times 10^{-12} & -5.151 \times 10^{-13} & 4.427 \times 10^{-8} \\ -6.064 \times 10^{-12} & 1.000 & 5.583 \times 10^{-12} & -4.798 \times 10^{-7} \\ -5.151 \times 10^{-13} & 5.583 \times 10^{-12} & 1.000 & 1.164 \times 10^{-5} \\ 4.427 \times 10^{-8} & -4.798 \times 10^{-7} & 1.164 \times 10^{-5} & 1.356 \times 10^{-10} \end{pmatrix}$
5_3^b	$\begin{pmatrix} 9.743 \times 10^{-1} & 2.251 \times 10^{-1} & 3.827 \times 10^{-3} \\ (0.893 - 2.064j) \times 10^{-1} & (-3.860 + 8.937j) \times 10^{-1} & -4.148 \times 10^{-2} \\ (-0.023 - 8.571j) \times 10^{-3} & (-1.689 + 3.711j) \times 10^{-2} & 9.991 \times 10^{-1} \\ (4.0794 - 0.079j) \times 10^{-3} & (7.865 + 3.423j) \times 10^{-4} & 5.431 \times 10^{-13} \end{pmatrix}$	$\begin{pmatrix} 9.999 \times 10^{-1} & -1.590 \times 10^{-6} & -3.664 \times 10^{-12} & 4.152 \times 10^{-3} \\ -1.590 \times 10^{-6} & 9.999 \times 10^{-1} & -3.380 \times 10^{-13} & 3.830 \times 10^{-4} \\ -3.664 \times 10^{-12} & -3.380 \times 10^{-13} & 1.000 & 8.825 \times 10^{-10} \\ 4.152 \times 10^{-3} & 3.830 \times 10^{-4} & 8.825 \times 10^{-10} & 1.738 \times 10^{-5} \end{pmatrix}$

Table 5.7: Mixing \mathbf{V} and FCNC \mathbf{F}^u matrices corresponding to the texture pairs identified in Table 5.6. The subscript $q = d, s, b$ corresponds to the decoupled down quark state.

5.2.2 Global fits

We now comment on the compatibility between the theoretical predictions of the texture pairs and each flavour constraint. Our results from the global fit are presented in Tables 5.10 - 5.18. Following the order for each flavour constraint, presented in Sec. 5.1, we have:

- **Meson mixing:** In Tables 5.8 and 5.9 we present the $\Delta_{\text{NP}}^{B_d}/\Delta_{\text{SM}}^{B_d}$ and $\Delta_{\text{NP}}^{B_s}/\Delta_{\text{SM}}^{B_s}$ ratios computed for each texture. The NP contributions to the B mesons mixing is negligible, with the closest value $\sim 7 \times 10^{-3}$ lower than the SM counterpart in both mixings. Hence, the model's predictions for these physical processes are identical to the SM case. Indeed, examining Eqs. (5.14), (5.17), (5.18), (5.19) and (5.17), the SM prediction corresponds to the limit $\Delta_{\text{NP}}^{B_{d,s}} = 0$. This explains the consistent χ^2 discrepancy of $(0.18/0.14)^2 = 1.65$ and $(0.199/0.062)^2 = 10.30$ to experimental data exhibited by the real and imaginary parts of the $\Delta_{\text{NP}}^{B_d}/\Delta_{\text{SM}}^{B_d}$ ratio, respectively. The null value for the $\Delta_{\text{NP}}^{B_s}/\Delta_{\text{SM}}^{B_s}$ ratio is within the experimental uncertainty, maintaining the SM agreement with B_s^0 oscillation data. Given that we set the conservative lower bound for the VLQ mass $m_T > 1$ TeV, we conclude from the inspection of Fig. B.1 that $S_0(x_T) > S_0(x_T, x_t) > S_0(x_t)$. Thus, in order to achieve a negligible NP contribution comparing to the SM one, the value of λ_{qb}^T has to be much lower than λ_{qb}^t , which is a consequence of $\mathbf{V}_{Tb} \ll \mathbf{V}_{tb}$ (see Table 5.7).

Table 5.10 contains the $|\Delta_{\text{NP}}^{K^0}|$ and $|\text{Im} \Delta_{\text{NP}}^{K^0}|$ predictions relevant in kaon oscillation data. The 5_b^3 texture presents the highest value for these parameters, with $|\Delta_{\text{NP}}^{K^0}| = 1.059 \times 10^{-8}$ and $|\text{Im} \Delta_{\text{NP}}^{K^0}| = 7.498 \times 10^{-9}$. Nonetheless, these values are 3 and 1 order of magnitude below the experimental bounds in Eqs. (5.15) and (5.16), respectively.

Finally, concerning the D^0 meson oscillations, all textures conform to the criteria established for the experimental upper bounds. However, the minimisation procedure results in texture pairs that saturate the allowed value for $|\mathbf{F}_{cu}^u|^2$ as shown in Table 5.11, when we consider a down or strange decoupled quark. Interestingly, the textures with a decoupled bottom quark do not follow this tendency: these predict a $|\mathbf{F}_{cu}^u|^2$ several orders of magnitude below the maximum threshold.

- **Rare top decays:** The phenomenological consequences coming from rare top decays can be inferred from Table 5.12. It is clear that the textures pairs are compatible with current experimental limits. We remark that the textures 5^d and 5^s present $|\mathbf{F}_{tu}^u|$ and $|\mathbf{F}_{tc}^u|$ values in the $10^{-8} \sim 10^{-5}$ range, with the 5^b textures leading to values $\sim 10^{-12}$. This, together with the results stemming from the D^0 meson oscillation, indicates that the structure of the 5^b textures provides a higher suppression of tree-level FCNC when compared to the ones with a decoupled d or s quark, which is corroborated by comparing the \mathbf{F}^u matrix entries values show in Table 5.7.
- **Rare bottom meson decays:** The theoretical values for the parameters in Eqs. (5.32) and (5.34) regarding the decays $B_q^0 \rightarrow \mu^+ \mu^-$, where $q = d, s$, are given in Tables 5.13 and 5.14, respectively. As explained in Sec. 5.1.3, the NP contributions to these decays stem from two distinct sources: $\lambda_{db}^T Y_0(x_T)$, which corresponds to the generalisation of the SM contribution, and the term $\Delta_{\text{NP}}^{\text{pen.}} = \sum \mathbf{V}_{id}^* (\mathbf{F}_{ij}^u - \delta_{ij}) \mathbf{V}_{jb} N(x_i, x_j)$ from the FCNC in the penguin diagram (see Fig. 5.7). We remark

that, once again, the dominant contribution for these processes comes from the SM term $\lambda_{db}^t Y_0(x_t)$, while each NP contribution individually is at least two orders of magnitude lower. There are two exceptions to this rule: the 5_3^s (5_3^d) texture produce $\lambda_{qb}^T Y_0(x_T)$ and $\Delta_{\text{NP}}^{\text{pen}}$ values comparable to the SM scenario for the B_d^0 (B_s^0) decay. However, these contributions cancel each other, turning the prediction of the model into the SM one. The texture pairs retain compatibility with the B_d^0 leptonic decay. In the B_s^0 case, there is a $\sim 1.73\sigma$ tension between the theoretical and experimental values, presenting a slight decline in compatibility when compared to the SM $\chi_{\text{SM}}^2 = 1.66$. This is a consequence of two distinct features: in our model the mixing matrix \mathbf{V} is no longer unitary; our methodology only fits the absolute values of \mathbf{V}_{CKM} . This results in different complex phases for the \mathbf{V} entries, which may lead to destructive or constructive effects in the calculations, thus altering the SM contributions.

- **Rare kaon decays and ϵ/ϵ' parameter:** The numerical results concerning the phenomenological constraints from rare kaon decays are presented in Tables 5.15, 5.16 and 5.17, and the ones for the CP violation parameter ϵ/ϵ' in Table 5.18. We remark a similar tendency in the data compared to the $B_q^0 \rightarrow \mu^+ \mu^-$ case: in general, the NP contribution is negligible. Note, however, that the 5_b^3 texture presents a cancellation between its NP contributions, which are individually $\sim 10^{-1}$ smaller than the SM counterparts. Regarding the agreement with experimental data, we verify that the texture pairs are in agreement with the experimental constraints discussed in the beginning of the Sec. 5.2.1.

Texture	$\Delta_{\text{SM}}^{B_d} (\times 10^{-4})$	$\Delta_{\text{NP}}^{B_d}$	$\Delta_{\text{NP}}^{B_d} / \Delta_{\text{SM}}^{B_d}$	Compatibility(χ^2)	
				Re	Im
5_1^d	$1.01388 - 0.00004i$	$(2.34538 - 0.00005i) \times 10^{-9}$	$(2.31328 + 0.00005i) \times 10^{-5}$	1.65	10.30
5_3^d	$1.01577 - 0.00004i$	$(6.549 - 2.898i) \times 10^{-17}$	$(6.448 - 2.853i) \times 10^{-13}$	1.65	10.30
5_1^s	$0.6629 + 0.7695i$	$(3.426 + 3.871i) \times 10^{-13}$	$(5.089 - 0.068i) \times 10^{-9}$	1.65	10.30
5_3^s	$0.6612 + 0.7688i$	$(-4.637 - 5.260i) \times 10^{-7}$	$(-6.915 + 0.085i) \times 10^{-3}$	1.53	10.31
5_1^b	$-1.016 - 0.006i$	$(-4.973 - 0.030i) \times 10^{-16}$	$(4.8968 + 0.0001i) \times 10^{-12}$	1.65	10.30
5_3^b	$-1.018 - 0.006i$	$(-0.031 + 1.383i) \times 10^{-16}$	$(0.023 - 1.359i) \times 10^{-12}$	1.65	10.30

Table 5.8: Model predictions for $\Delta_{\text{SM}}^{B_d}$ and $\Delta_{\text{NP}}^{B_d}$ for each texture pair identified in Table 5.6. Comparing the ratios $\Delta_{\text{NP}}^{B_d} / \Delta_{\text{SM}}^{B_d}$ with the constraints in Eqs. (5.17) and (5.18), we observe that the texture pairs present consistently $\chi^2 \sim 1.6$ and $\chi^2 \sim 10.3$ tension in the real and imaginary parts of $\Delta_{\text{NP}}^{B_d} / \Delta_{\text{SM}}^{B_d}$ respectively.

Texture	$\Delta_{\text{SM}}^{B_s} (\times 10^{-3})$	$\Delta_{\text{NP}}^{B_s}$	$\Delta_{\text{NP}}^{B_s} / \Delta_{\text{SM}}^{B_s}$	Compatibility	
				Re	Im
5_1^d	$1.498 - 1.744i$	$(1.064 - 1.204i) \times 10^{-14}$	$(6.989 + 0.096i) \times 10^{-12}$	✓	✓
5_3^d	$1.501 - 1.741i$	$(-0.996 + 1.125i) \times 10^{-5}$	$(-6.534 - 0.087i) \times 10^{-3}$	✓	✓
5_1^s	2.295	2.613×10^{-7}	1.139×10^{-4}	✓	✓
5_3^s	2.298	$(7.828 + 3.463i) \times 10^{-18}$	$(3.406 + 1.507i) \times 10^{-15}$	✓	✓
5_1^b	$-1.509 + 1.731i$	$(-7.391 + 8.477i) \times 10^{-15}$	4.897×10^{-12}	✓	✓
5_3^b	$-1.513 + 1.738i$	$(-1.028 - 0.926i) \times 10^{-16}$	$(-1.002 + 0.600i) \times 10^{-14}$	✓	✓

Table 5.9: Model predictions for $\Delta_{\text{SM}}^{B_s}$ and $\Delta_{\text{NP}}^{B_s}$ for each texture pair identified in Table 5.6. Comparing the ratios $\Delta_{\text{NP}}^{B_s} / \Delta_{\text{SM}}^{B_s}$ with the constraints in Eqs. (5.19) and (5.20), we conclude that the texture pairs are compatible with B_s^0 meson oscillation data.

Texture	$ \Delta_{\text{NP}}^{K^0} $	Compatibility	$ \text{Im } \Delta_{\text{NP}}^{K^0} $	Compatibility
5_1^d	4.774×10^{-12}	✓	3.388×10^{-12}	✓
5_3^d	8.148×10^{-17}	✓	2.994×10^{-17}	✓
5_1^s	2.430×10^{-11}	✓	1.701×10^{-11}	✓
5_3^s	9.631×10^{-18}	✓	3.588×10^{-18}	✓
5_1^b	5.345×10^{-21}	✓	3.834×10^{-21}	✓
5_3^b	1.059×10^{-8}	✓	7.498×10^{-9}	✓

Table 5.10: Model predictions for $|\Delta_{\text{NP}}^{K^0}|$ and $|\text{Im } \Delta_{\text{NP}}^{K^0}|$ for each texture pair identified in Table 5.6. Comparing these values with the bounds in Eqs. (5.15) and (5.16), we conclude that these texture pairs are compatible with kaon oscillation data.

Texture	$ \mathbf{F}_{cu}^u ^2$	Compatibility
5_1^d	3.321×10^{-8}	1σ
5_3^d	3.321×10^{-8}	1σ
5_1^s	3.321×10^{-8}	1σ
5_3^s	3.321×10^{-8}	1σ
5_1^b	2.044×10^{-25}	✓
5_3^b	2.529×10^{-12}	✓

Table 5.11: Model predictions for $|\mathbf{F}_{cu}^u|^2$ for each texture pair identified in Table 5.6. Comparing these values with the upper bound in Eq. (5.22), we observe that the texture pairs are compatible with D^0 meson oscillation data at 1σ .

Texture	$ \mathbf{F}_{tu}^u $	$ \mathbf{F}_{tc}^u $	$t \rightarrow Zu$ Compatibility	$t \rightarrow Zc$ Compatibility
5_1^d	6.972×10^{-6}	1.606×10^{-6}	✓	✓
5_3^d	2.594×10^{-7}	1.123×10^{-6}	✓	✓
5_1^s	7.818×10^{-6}	3.381×10^{-5}	✓	✓
5_3^s	2.358×10^{-7}	5.440×10^{-8}	✓	✓
5_1^b	5.151×10^{-13}	5.584×10^{-12}	✓	✓
5_3^b	3.664×10^{-12}	3.376×10^{-13}	✓	✓

Table 5.12: Model predictions for $|\mathbf{F}_{tu}^u|$ and $|\mathbf{F}_{tc}^u|$ for each texture pair identified in Table 5.6. Comparing these values with the upper bounds in Eq. (5.25), we observe that the texture pairs are compatible with rare top decays data.

Texture	$\lambda_{db}^t Y_0(x_t)(\times 10^{-3})$	$\lambda_{db}^T Y_0(x_T)$	$\Delta_{\text{NP}}^{\text{pen.}}$	$ \lambda_{db}^t Y_0(x_t) + \Delta_{\mu\mu}^{B_d} ^2$	Compatibility
5_1^d	$8.8264 - 0.0002i$	4.191×10^{-6}	$(1.87420 + 0.00009i) \times 10^{-5}$	7.831×10^{-5}	✓
5_3^d	$8.8346 - 0.0002i$	$(2.984 - 1.321i) \times 10^{-13}$	$(-1.861 + 0.856i) \times 10^{-9}$	7.805×10^{-5}	✓
5_1^s	$-8.030 - 3.682i$	$(-1.844 - 0.815i) \times 10^{-10}$	$(7.423 + 2.479i) \times 10^{-9}$	7.804×10^{-5}	✓
5_3^s	$8.022 + 3.682i$	$(-8.781 - 3.885i) \times 10^{-3}$	$(8.752 + 3.872i) \times 10^{-3}$	7.736×10^{-5}	✓
5_1^b	$-0.027 + 8.834i$	$(-0.021 + 6.829i) \times 10^{-13}$	$(-0.007 + 2.191i) \times 10^{-12}$	7.803×10^{-5}	✓
5_3^b	$0.024 - 8.846i$	$(-5.506 - 0.107i) \times 10^{-14}$	$(1.953 + 0.034i) \times 10^{-11}$	7.825×10^{-5}	✓

Table 5.13: Model predictions regarding the $B_d^0 \rightarrow \mu^+ \mu^-$ decay for each texture pair identified in Table 5.6 [check the terms in Eqs. (5.32) and (5.34)]. Comparing these values with the constraint in Eq. (5.36), we observe that the texture pairs are compatible with $B_d^0 \rightarrow \mu^+ \mu^-$ data. We denote $\Delta_{\text{NP}}^{\text{pen.}} = \sum \mathbf{V}_{id}^* (\mathbf{F}_{ij}^u - \delta_{ij}) \mathbf{V}_{jb} N(x_i, x_j)$.

Texture	$\lambda_{sb}^t Y_0(x_t)(\times 10^{-2})$	$\lambda_{sb}^T Y_0(x_T)$	$\Delta_{\text{NP}}^{\text{pen.}}$	$ \lambda_{sb}^t Y_0(x_t) + \Delta_{\mu\mu}^{B_s} ^2$	Compatibility(χ^2)
5_1^d	$-3.820 + 1.754i$	$(-5.515 + 2.441i) \times 10^{-12}$	$(1.685 - 0.559i) \times 10^{-9}$	1.767×10^{-3}	3.03
5_3^d	$-3.821 + 1.751i$	$(1.367 - 0.604i) \times 10^{-2}$	$(-1.356 + 0.599i) \times 10^{-2}$	1.757×10^{-3}	2.84
5_1^s	4.199	2.144×10^{-5}	5.528×10^{-5}	1.770×10^{-3}	3.09
5_3^s	-4.202	$(-2.027 - 0.897i) \times 10^{-14}$	$(3.826 + 1.981i) \times 10^{-10}$	1.766×10^{-3}	3.02
5_1^b	$-1.739 - 3.824i$	$(-1.345 - 2.956i) \times 10^{-12}$	$(-4.314 - 9.486i) \times 10^{-12}$	1.765×10^{-3}	2.99
5_3^b	$1.743 + 3.830i$	$(-1.062 - 0.462i) \times 10^{-14}$	$(3.842 - 1.471i) \times 10^{-12}$	1.770×10^{-3}	3.11

Table 5.14: Model predictions regarding the $B_s^0 \rightarrow \mu^+ \mu^-$ decay for each texture pair identified in Table 5.6 [check the terms in Eqs. (5.32) and (5.34)]. Comparing these values with the constraint in Eq. (5.37), we observe that the texture pairs present a tension with $B_s^0 \rightarrow \mu^+ \mu^-$ data at $\sim 1.73\sigma$. We denote $\Delta_{\text{NP}}^{\text{pen.}} = \sum \mathbf{V}_{is}^* (\mathbf{F}_{ij}^u - \delta_{ij}) \mathbf{V}_{jb} N(x_i, x_j)$.

Texture	$ \mathbf{V}_{us} ^2(\times 10^{-2})$	$Y_{NL}\text{Re}\lambda_{sd}^c(\times 10^{-5})$	$\eta_t^Y Y_0(x_t)\text{Re}\lambda_{sd}^t(\times 10^{-4})$	$\eta_T^Y Y_0(x_T)\text{Re}\lambda_{sd}^T$	$\Delta_{\text{NP}}^{\text{pen.}}$	Value($\times 10^{-7}$)	Compatibility
5_1^d	5.046	-6.423	-3.309	-1.630×10^{-7}	-7.838×10^{-7}	1.568	✓
5_3^d	5.065	-6.437	-3.312	-7.860×10^{-12}	-5.099×10^{-8}	1.566	✓
5_1^s	5.064	-6.437	-3.309	-1.752×10^{-7}	-5.021×10^{-7}	1.568	✓
5_3^s	5.046	-6.423	-3.309	2.542×10^{-12}	-5.495×10^{-8}	1.561	✓
5_1^b	5.066	-6.438	-3.311	-1.388×10^{-16}	2.372×10^{-14}	1.564	✓
5_3^b	5.065	-6.438	-3.321	8.001×10^{-5}	-7.485×10^{-5}	1.531	✓

Table 5.15: Model predictions regarding the $\text{Br}(K_L \rightarrow \mu^+ \mu^-)_{\text{SD}}/\text{Br}(K^+ \rightarrow \mu^+ \nu)$ ratio for each texture pair identified in Table 5.6 [check the terms in Eqs. (5.33) and (5.35)]. Comparing these values with the constraint in Eq. (5.38), we observe that the texture pairs are compatible with experimental data. We denote $\Delta_{\text{NP}}^{\text{pen.}} = \sum \eta_i^Y \text{Re} [\mathbf{V}_{is}^* (\mathbf{F}_{ij}^u - \delta_{ij}) \mathbf{V}_{jd}] N(x_i, x_j)$. The column “Value” presents the theoretical value computed from the bound (5.38).

57

Texture	$ \mathbf{V}_{us} ^2(\times 10^{-2})$	$\lambda_{sd}^c(\times 10^{-1})$	$\lambda_{sd}^t \eta_t^X X_0(x_t)(\times 10^{-4})$	$\lambda_{sd}^T \eta_T^X X_0(x_T)$	$\Delta_{\text{NP}}^{\text{pen.}}$	Value($\times 10^{-5}$)	Compatibility(χ^2)
5_1^d	5.046	$-2.185 - 0.001i$	$-4.988 + 2.290i$	$(-1.609 + 0.712i) \times 10^{-7}$	$(-7.714 + 3.169i) \times 10^{-7}$	3.282	0.92
5_3^d	5.065	$-2.189 - 0.001i$	$-4.994 + 2.288i$	$(7.733 + 0.005i) \times 10^{-12}$	$(-4.998 - 0.003i) \times 10^{-8}$	3.270	0.93
5_1^s	5.064	$-2.189 - 0.001i$	$-4.989 + 2.287i$	$(-1.772 + 0.784i) \times 10^{-7}$	$(-4.931 + 1.962i) \times 10^{-7}$	3.271	0.93
5_3^s	5.046	$-2.185 - 0.001i$	$-4.988 + 2.289i$	$(2.49786 + 0.00009i) \times 10^{-12}$	$(-5.5745 + 0.0002i) \times 10^{-8}$	3.273	0.93
5_1^b	5.066	$-2.190 - 0.001i$	$-4.991 + 2.288i$	$(-1.373 + 0.629i) \times 10^{-16}$	$(2.330 - 1.069i) \times 10^{-14}$	3.266	0.94
5_3^b	5.065	$-2.190 - 0.001i$	$-5.006 + 2.295i$	$(8.091 - 3.709i) \times 10^{-5}$	$(-7.352 + 3.370i) \times 10^{-5}$	3.210	1

Table 5.16: Model predictions regarding the $\text{Br}(K^+ \rightarrow \pi^+ \nu \bar{\nu})/\text{Br}(K^+ \rightarrow \pi^0 e^+ \bar{\nu})$ ratio for each texture pair identified in Table 5.6 [check the terms in Eqs. (5.39) and (5.41)]. Comparing these values with the constraint in Eq. (5.43), we observe that the texture pairs are compatible with $\text{Br}(K^+ \rightarrow \pi^+ \nu \bar{\nu})/\text{Br}(K^+ \rightarrow \pi^0 e^+ \bar{\nu})$ data at $\sim 1\sigma$. We denote $\Delta_{\text{NP}}^{\text{pen.}} = \sum \eta_i^X \mathbf{V}_{is}^* (\mathbf{F}_{ij}^u - \delta_{ij}) \mathbf{V}_{jd} N(x_i, x_j)$. The column “Value” presents the theoretical value computed from the bound (5.43).

Texture	$\lambda_{sd}^c X_0(x_c)(\times 10^{-4})$	$\lambda_{sd}^t X_0(x_t)(\times 10^{-4})$	$\lambda_{sd}^T X_0(x_T)$	$\Delta_{\text{NP}}^{\text{pen.}}$	Value	Compatibility
5_1^d	$-3.258 - 0.002i$	$-5.019 + 2.304i$	$(-1.618 + 0.717i) \times 10^{-7}$	$(-7.755 + 3.188i) \times 10^{-7}$	1.000	✓
5_3^d	$-3.265 - 0.002i$	$-5.024 + 2.302i$	$(7.780 + 0.005i) \times 10^{-12}$	$(-5.032 - 0.003i) \times 10^{-8}$	1.000	✓
5_1^s	$-3.267 - 0.002i$	$-5.019 + 2.301i$	$(-1.783 + 0.789i) \times 10^{-7}$	$(-4.961 + 1.973i) \times 10^{-7}$	1.000	✓
5_3^s	$-3.259 - 0.002i$	$-5.018 + 2.303i$	$(2.51294 + 0.00009i) \times 10^{-12}$	$(-5.5482 - 0.0002i) \times 10^{-12}$	1.000	✓
5_1^b	$-3.266 - 0.002i$	$-5.021 + 2.302i$	$(-1.381 + 0.633i) \times 10^{-16}$	$(2.344 - 1.075i) \times 10^{-14}$	1.000	✓
5_3^b	$-3.267 - 0.002i$	$-5.036 + 2.309i$	$(8.140 - 3.732i) \times 10^{-5}$	$(-7.396 + 3.391i) \times 10^{-5}$	0.971	✓

Table 5.17: Model predictions regarding the $\text{Br}(K_L \rightarrow \pi^0 \nu \bar{\nu}) / \text{Br}(K_L \rightarrow \pi^0 \nu \bar{\nu})_{\text{SM}}$ ratio for each texture pair identified in Table 5.6 [check the terms in Eqs. (5.40) and (5.42)]. Comparing these values with the constraint in Eq. (5.44), we observe that the texture pairs are compatible with $\text{Br}(K_L \rightarrow \pi^0 \nu \bar{\nu}) / \text{Br}(K_L \rightarrow \pi^0 \nu \bar{\nu})_{\text{SM}}$ data. We denote $\Delta_{\text{NP}}^{\text{pen.}} = \sum \mathbf{V}_{is}^* (\mathbf{F}_{ij}^u - \delta_{ij}) \mathbf{V}_{jd} N(x_i, x_j)$. The column “Value” presents the theoretical value computed from the bound (5.44).

58

Texture	$F_{\epsilon'}(x_t) \text{Im } \lambda_{sd}^t$	$F_{\epsilon'}(x_T) \text{Im } \lambda_{sd}^T$	$\Delta_{\text{NP}}^{\text{pen.}}$	Compatibility
5_1^d	1.495×10^{-3}	-4.549×10^{-7}	-2.078×10^{-6}	✓
5_3^d	1.493×10^{-3}	-3.282×10^{-14}	2.062×10^{-10}	✓
5_1^s	1.492×10^{-3}	-4.374×10^{-7}	-1.286×10^{-6}	✓
5_3^s	1.494×10^{-3}	-5.650×10^{-16}	1.099×10^{-11}	✓
5_1^b	1.493×10^{-3}	-3.982×10^{-16}	7.009×10^{-14}	✓
5_3^b	1.497×10^{-3}	2.079×10^{-4}	-2.210×10^{-4}	✓

Table 5.18: Model predictions regarding the CP violation parameter ϵ/ϵ' for each texture pair identified in Table 5.6 [check the terms in Eqs. (5.45) and (5.53)]. Comparing these values with $\epsilon/\epsilon' = (1.66 \pm 0.23) \times 10^{-3}$ [37], we observe that the texture pairs are compatible with ϵ/ϵ' data. We denote $\Delta_{\text{NP}}^{\text{pen.}} = (P_X + P_Y + P_Z) \sum_{i,j=u,c,t,T} \text{Im} [\mathbf{V}_{is}^* (\mathbf{F}_{ij}^u - \delta_{ij}) \mathbf{V}_{jd} N(x_i, x_j)]$.

5.2.3 Impact on the Cabibbo angle anomaly

So far, we have stated that the methodology employed in this Section improves the fit of the texture pairs to these phenomenological constraints when compared to the ones in Table 4.10. However, we have not yet checked the compatibility of these textures with quark data. In Fig. 5.8, we represent in the $(|(\mathbf{V}_{\text{CKM}})_{us}|, |(\mathbf{V}_{\text{CKM}})_{ud}|)$ plane, as coloured circles (triangles), the predictions of the texture pairs in the Table 4.10 (Table 5.6), obtained when excluding (including) flavour phenomenology. Each point is labelled with the corresponding texture pair, following the notation explained in Sec. 4.3. Analogously to the plot in Fig. 2.4, the green lines correspond to $\Delta\chi^2_{\text{non-uni.}} = 2.3, 6.18$ and 11.83 contours, the green cross to the best fit point obtained in Sec. 2.3 and the black line to the unitarity condition for the first line of \mathbf{V}_{CKM} . The purple error bars stem from the SM fit performed in Ref. [37].

We begin the analysis of the plots by focusing on the fit results excluding flavour phenomenology. It is clear that the 5_1^d , 5_3^s and 5_3^b textures accommodate the CAA, presenting $\Delta\chi^2_{\text{non-uni.}} \approx 0.2$, whereas the 5_1^b point is close to the unitarity condition (black line), elucidating the results from Fig. 4.1. We also note that the 5_1^s point is within the SM error bar, with 5_3^d falling close to this bound. Taking into account the flavour phenomenology in the minimisation procedure, the fit to quark data worsens, leading to a distancing of the $(|(\mathbf{V}_{\text{CKM}})_{us}|, |(\mathbf{V}_{\text{CKM}})_{ud}|)$ points from the best fit point. This should come as no surprise, as we impose more constraints to the same input variables. The inclusion of flavour phenomenology leads to a significant shift in the fit results:

- the 5_1^d and 5_3^s points fall outside the 1σ region, corresponding to $\Delta\chi^2_{\text{non-uni.}} \approx 2.7$;
- the 5_3^d and 5_1^s textures verify unitarity in the first row of \mathbf{V} within a short error margin;
- the 5_3^b presents the highest shift, with its best fit point going from a $\Delta\chi^2_{\text{non-uni.}} \approx 0.2$ to $\Delta\chi^2_{\text{non-uni.}} \approx 9.5$, which is within the SM fit errorbar;
- the 5_1^b texture presents similar results regardless of flavour phenomenology, i.e. is within the SM fit errorbar and thus does not accommodate the CAA.

The low impact of flavour phenomenology on the 5_1^b texture is due to small improvement in the fit provided by $\chi^2_{\text{pheno.}}$. Indeed, recalling the discussion in the beginning of Sec. 5.2, the most restrictive physical process is the $B_s \rightarrow \mu^+ \mu^-$ decay, which, from Eq. (5.58) and Table 5.14, undergoes a shift in $\chi^2 = 4.78 \rightarrow 2.99$ when taken into consideration in the fit. Hence, this tiny difference leads to a small shift in quark data compatibility. The same reasoning leads to similar conclusions regarding the remaining textures. The most limiting constraint for the 5^d and 5^s textures is the $D^0 - \bar{D}^0$ mixing. Employing the methodology explained in this Chapter, the compatibility of these textures to D^0 oscillations greatly improve. However, the reduction of \mathbf{F}_{uc}^u by one (two) orders of magnitude for the textures 5_1^d and 5_3^s (5_3^d and 5_1^s) results in a significant impact to CAA compatibility. The worst case consists of the 5_3^b texture, which fits the constraint coming from ϵ_K after an improvement of this value by three orders of magnitude. This argument is supported by the analysis done previously in Sec. 4.3. The parameter space of the 5_3^b texture in Fig. 4.1 retains less freedom compared to the 5_1^d and 5_3^s ones, explaining the worse fit to quark mixing data for 5_3^b compared to the latter ones when we include flavour phenomenology in our analysis.

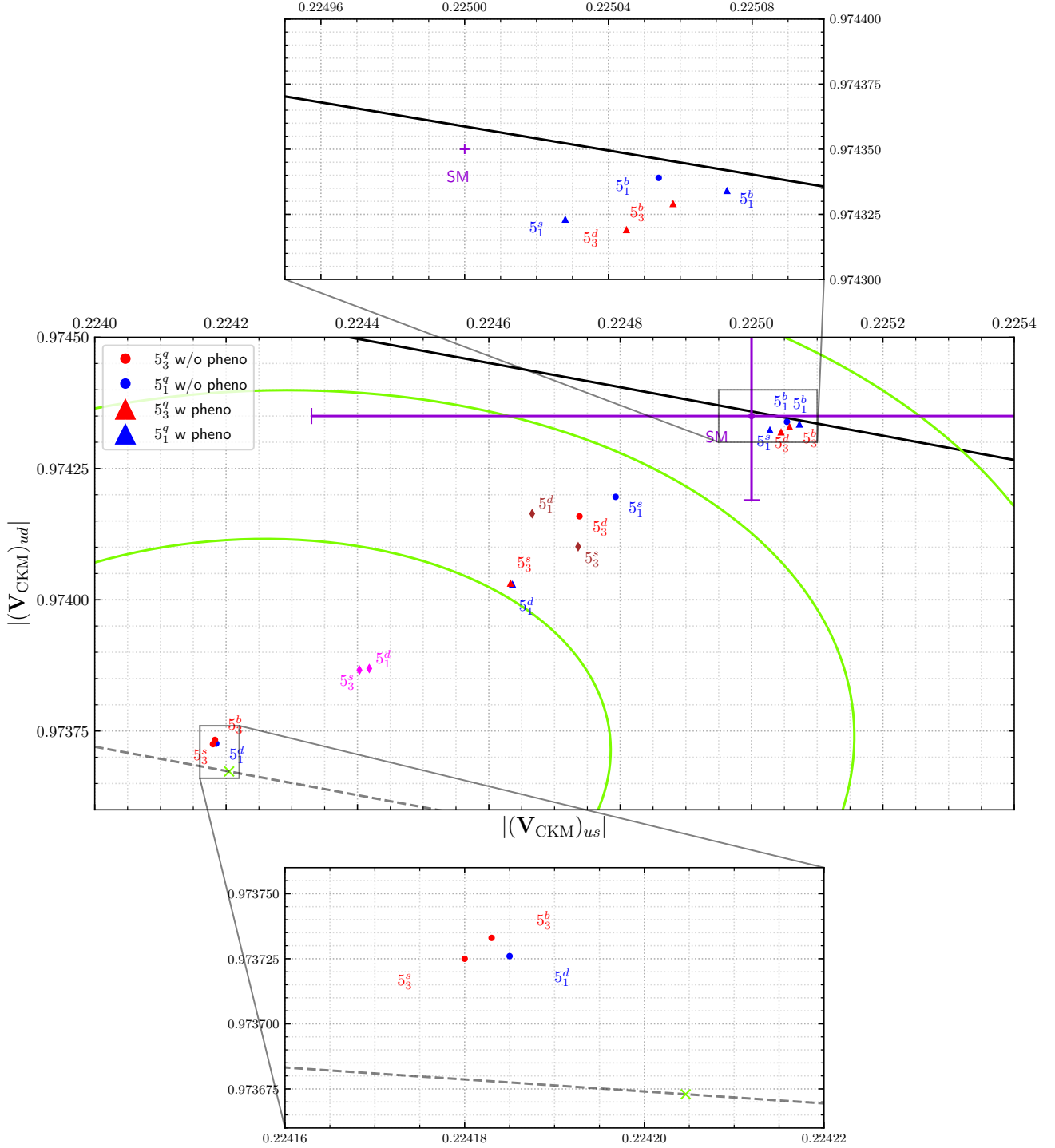


Figure 5.8: $(|(V_{CKM})_{us}|, |(V_{CKM})_{ud}|)$ points corresponding to the texture pairs in the Tables 4.10 and 5.6, represented as circles and triangles, respectively (see text for details). The purple error bars correspond to the SM fit to quark mixing data in Ref. [37]. The green contours and black curves are analogous to the ones in Fig. 2.4. The magenta and brown diamonds represent the global fit results obtained when using $\eta_D = 0.25$ and $\eta_D = 1$ as input.

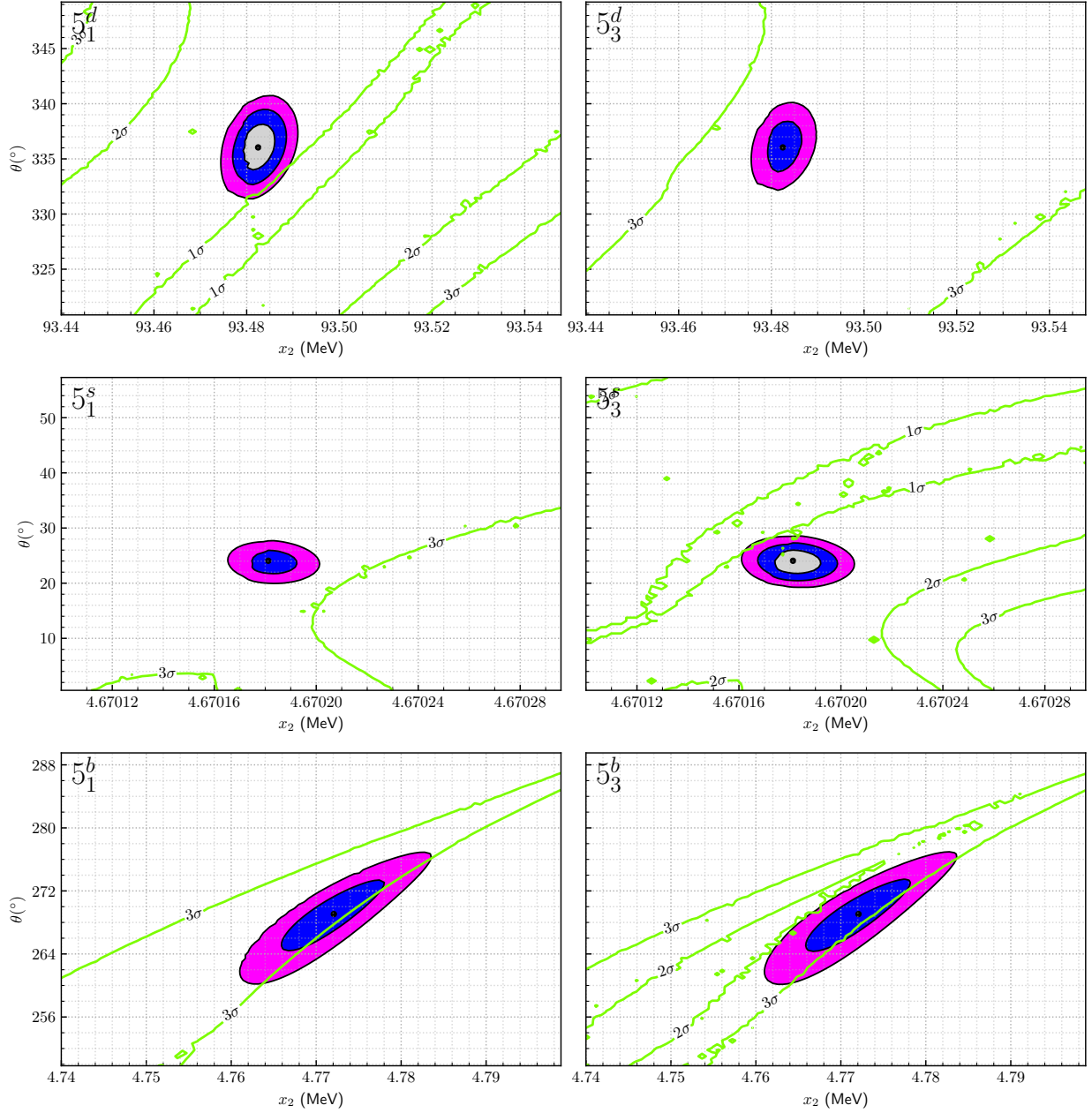


Figure 5.9: Constraints on the (x_2, θ) parameter space imposed by quark experimental data in Table 4.1 and flavour phenomenology described in Sec 5.1. The 1, 2 and 3σ regions for $\Delta\chi^2$ are coloured in grey, blue and magenta, respectively. The green contours representing the 1, 2 and 3σ for $\Delta\chi^2_{\text{non-uni.}}$ are determined following the procedure described in Sec. 2.3.

The textures 5_1^d and 5_3^s provide the most interesting results, improving the CAA fit while maintaining a similar compatibility to flavour phenomenology compared to the SM. Recalling the discussion on $D^0 - \overline{D}^0$ oscillations, we see in Table 5.11 that these textures saturate the $|\mathbf{F}_{uc}^u|^2$ upper bound. To confirm that this is indeed the most restrictive process, we repeat the fit described in Sec. 5.2.1 twice, assuming a negligible QCD correction η_D ($\eta_D = 1$), represented by the brown points, and inputting $\eta_D = 0.25$, corresponding to the magenta ones. The results confirm our hypothesis: the smaller value for η_D results in a slight increase to the $D^0 - \overline{D}^0$ upper bound, which in turn leads to a substantial improvement in the CAA fit. The opposite effect is observed for the $\eta_D = 1$ case. We also confirmed that the $\eta_D = 0.25$ fit does not influence the remaining flavour processes, as the fit gives a similar χ^2 to the original one. Hence, we conclude that the determination of the parameters B_D and η_D , corresponding to corrections stemming from the VIA and QCD, respectively, as well as the estimation of long distance contributions to $D^0 - \overline{D}^0$ mixing, are critical for our model compatibility to both quark data and flavour phenomenology.

Lastly, to better comprehend the impact of flavour processes on the parameter space of the mass matrices \mathbf{M}_u and \mathbf{M}_d , we repeat the methodology described in Sec. 4.3, now using the χ^2 function defined in Eq. (5.60). The results are displayed in Fig. 5.9. The (x_2, θ) parameter spaces in Figs. 4.1 and 5.9 are identical: the most striking difference is that the χ^2 minimum increase for 5_3^b is higher compared to 5_1^d and 5_3^s , exhibiting only $\Delta\chi^2 \leq 2\sigma$ and $\leq 3\sigma$ regions. This is corroborated by the identical x_2 and θ values in Tables 4.10 and 5.6, with the largest discrepancy being $\Delta\theta \approx 1^\circ$ between the 5^b textures. Furthermore, comparing the \mathbf{M}_u matrices between these Tables, we observe that only the b_2 and c entries of each texture present distinct values [revisit the parameterisation in Eq. (4.11)]. Recalling Eq. (4.15), together with the small fit values for a_3 compared to b_3 , we note that $a_3^2 + b_3^2 \approx b_3^2$. Given the discussion at the end of Sec. 4.3, the phenomenological constraints included in χ_{pheno}^2 are mostly accommodated by the variation in the b_2 and c values, since the remaining matrix entries are fixed by quark data and a_3 provides a negligible influence for the structure of \mathcal{H}^u . These constraints result in the translation of the $\Delta\chi_{\text{non-uni.}}^2 = 2.3, 6.18, 11.83$ green contours in Fig. 5.9. Specifically, the $\Delta\chi_{\text{non-uni.}}^2 \leq 1\sigma$ regions are now outside the $\Delta\chi^2 \leq 2\sigma$ regions for the 5_1^d and 5_3^s textures. Furthermore, the 5_3^b parameter space is within $2\sigma \leq \Delta\chi_{\text{non-uni.}}^2 \leq 3\sigma$ region. This is showcasing, once again, the more restrictive nature of 5_3^b compared to 5_1^d and 5_3^s . Finally, as stated before, the fit results for 5_1^b are the least affected by flavour phenomenology. This is shown in Figs. 4.1 and 5.9 by presenting identical parameter spaces.

Chapter 6

Concluding remarks

The remarkable success of the SM in the description of interactions among elementary particles is an astounding achievement of Physics. However, experimental evidence, such as neutrino oscillations, has established beyond doubt that the SM is an incomplete theory. Recent improvements in the determination of the \mathbf{V}_{CKM} first row are in tension with the SM prediction of a unitary quark mixing matrix. This observation constitutes a possible hint of NP. Furthermore, the highly stratified nature of fermion mixing and masses suggests the existence of an underlying guiding principle. However, the SM does not provide a mechanism that assembles this piece of the *flavour puzzle*.

In Chapter 2, after shortly reviewing the fundamental concepts of the SM, we revisit the determination of $|\mathbf{V}_{\text{CKM}}|_{ud}$ and $|\mathbf{V}_{\text{CKM}}|_{us}$ from three distinct experimental sources. This analysis showcases the current tensions among these observations within the SM, also known as CAA.

In this thesis we study a SM extension with an up-type isosinglet VLQ, which constitutes one of the simplest BSM frameworks addressing the CAA. To lay the theoretical foundation of this work, the general scenario with an arbitrary number of down-type and up-type isosinglet VLQs is discussed in Chapter 3. We show that these models present non-unitary mixing and tree-level FCNC mediated by the Z and Higgs bosons, and establish the relation between these features of the model.

A systematic search of the maximally restrictive texture zeros compatible with quark masses and mixing is performed in Chapter 4. The resulting patterns exhibit a total of 12 independent parameters responsible for the 16 current quark observables. These mass matrices flavour structures are imposed by global Abelian symmetries. To prevent vanishing mixings and massless quarks, this implementation requires the extension of the scalar sector with at least a second Higgs doublet. Out of the initial set of 237 non-equivalent maximally restrictive textures, only two are realisable within the minimal context of a 2HDM with a single $U(1)_F$ Abelian symmetry. The full reconstruction of the mass matrices from quark data proves to be cumbersome. Nonetheless, in Sec. 4.3 an indepth investigation of the parameter space clearly exhibits the predictive power of the texture zeros: for instance, the identified \mathbf{M}_d textures present a decoupled down quark state.

In Chapter 5, we study the phenomenological consequences to flavour processes, namely neutral meson mixing, rare meson and top decays, assuming the decoupling of 2HDM phenomenology. These constitute

vital tests to the model, as the GIM mechanism is violated by tree-level FCNC induced by VLQ mixing. A global fit to both quark data and flavour phenomenology is performed in Sec. 5.2.2. We observe that the presence of texture zeros heavily influences the impact of each flavour process: the textures with a decoupled b quark demonstrate a stronger suppression of FCNC compared to the ones with a decoupled d or s quark. This translates into more restrictive bounds coming from $D^0 - \bar{D}^0$ oscillations to the latter cases. Meanwhile, the decoupled b quark textures are more sensitive to kaon mixing and meson decays. Finally, in Sec. 5.2.3 we extensively discuss the interplay between flavour phenomenology and the CAA. We note an overall worse fit to CAA when flavour constraints are considered. This effect is most notorious for the 5_3^b texture: phenomenological constraints currently render this case as a non-viable solution to the CAA. Nonetheless, the 5_1^d and 5_3^s scenarios constitute the most promising results, presenting a better fit to CAA compared to the SM, while maintaining data compatibility according to the criteria established in Sec. 5.2.1.

This thesis leaves several possible pathways moving forward. The straightforward route is the study of the 2HDM effects on scalar and flavour constraints. The compatibility of the model with EW precision observables must also be checked. Should the model prove to be incompatible with these additional experimental constraints, a possible solution is to relax a few texture zeros, increasing both the model's degrees of freedom and the realisable texture pairs. Another interesting proposition is to attempt further symmetry realisations of the extensive list of maximally-restrictive textures identified in Table 4.2, extending the 2HDM scalar sector with another complex scalar singlet, and so on. Finally, similar frameworks using down-type or isodoublets VLQs are also possible. The plethora of potential branches from a minimal solution to both the CAA and the *flavour puzzle* shows the vast possibilities of SM extensions with VLQs and global Abelian flavour symmetries. This urges both experimental tests to clarify the CAA, as well as a theoretical effort to unveil the mysteries surrounding the origin of flavour structure.

Bibliography

- [1] G. Aad *et al.*, “Observation of a new particle in the search for the Standard Model Higgs boson with the ATLAS detector at the LHC,” *Physics Letters B*, vol. 716, no. 1, pp. 1–29, 2012.
- [2] S. Chatrchyan *et al.*, “Observation of a new boson at a mass of 125 GeV with the CMS experiment at the LHC,” *Physics Letters B*, vol. 716, no. 1, pp. 30–61, 2012.
- [3] F. Englert and R. Brout, “Broken Symmetry and the Mass of Gauge Vector Mesons,” *Phys. Rev. Lett.*, vol. 13, pp. 321–323, 1964.
- [4] P. W. Higgs, “Broken Symmetries and the Masses of Gauge Bosons,” *Phys. Rev. Lett.*, vol. 13, pp. 508–509, 1964.
- [5] P. W. Higgs, “Broken symmetries, massless particles and gauge fields,” *Phys. Lett.*, vol. 12, pp. 132–133, 1964.
- [6] G. Guralnik, C. Hagen, and T. Kibble, “Global Conservation Laws and Massless Particles,” *Phys. Rev. Lett.*, vol. 13, pp. 585–587, 1964.
- [7] N. Cabibbo, “Unitary Symmetry and Leptonic Decays,” *Phys. Rev. Lett.*, vol. 10, pp. 531–533, 1963.
- [8] M. Kobayashi and T. Maskawa, “CP Violation in the Renormalizable Theory of Weak Interaction,” *Prog. Theor. Phys.*, vol. 49, pp. 652–657, 1973.
- [9] C.-Y. Seng, M. Gorchtein, H. H. Patel, and M. J. Ramsey-Musolf, “Reduced Hadronic Uncertainty in the Determination of V_{ud} ,” *Phys. Rev. Lett.*, vol. 121, no. 24, p. 241804, 2018.
- [10] B. Belfatto, R. Beradze, and Z. Berezhiani, “The CKM unitarity problem: A trace of new physics at the TeV scale?,” *Eur. Phys. J. C*, vol. 80, no. 2, p. 149, 2020.
- [11] Y. Grossman, E. Passemar, and S. Schacht, “On the Statistical Treatment of the Cabibbo Angle Anomaly,” *JHEP*, vol. 07, p. 068, 2020.
- [12] A. M. Coutinho, A. Crivellin, and C. A. Manzari, “Global Fit to Modified Neutrino Couplings and the Cabibbo-Angle Anomaly,” *Phys. Rev. Lett.*, vol. 125, no. 7, p. 071802, 2020.

- [13] K. Cheung, W.-Y. Keung, C.-T. Lu, and P.-Y. Tseng, “Vector-like Quark Interpretation for the CKM Unitarity Violation, Excess in Higgs Signal Strength, and Bottom Quark Forward-Backward Asymmetry,” *JHEP*, vol. 05, p. 117, 2020.
- [14] A. Crivellin and M. Hoferichter, “ β Decays as Sensitive Probes of Lepton Flavor Universality,” *Phys. Rev. Lett.*, vol. 125, no. 11, p. 111801, 2020.
- [15] M. Endo and S. Mishima, “Muon $g - 2$ and CKM unitarity in extra lepton models,” *JHEP*, vol. 08, no. 08, p. 004, 2020.
- [16] B. Belfatto and Z. Berezhiani, “Are the CKM anomalies induced by vector-like quarks? Limits from flavor changing and Standard Model precision tests,” *JHEP*, vol. 10, p. 079, 2021.
- [17] G. C. Branco, J. T. Penedo, P. M. F. Pereira, M. N. Rebelo, and J. I. Silva-Marcos, “Addressing the CKM unitarity problem with a vector-like up quark,” *JHEP*, vol. 07, p. 099, 2021.
- [18] B. Capdevila, A. Crivellin, C. A. Manzari, and M. Montull, “Explaining $b \rightarrow s\ell^+\ell^-$ and the Cabibbo angle anomaly with a vector triplet,” *Phys. Rev. D*, vol. 103, no. 1, p. 015032, 2021.
- [19] A. Crivellin, F. Kirk, C. A. Manzari, and M. Montull, “Global Electroweak Fit and Vector-Like Leptons in Light of the Cabibbo Angle Anomaly,” *JHEP*, vol. 12, p. 166, 2020.
- [20] M. Kirk, “Cabibbo anomaly versus electroweak precision tests: An exploration of extensions of the Standard Model,” *Phys. Rev. D*, vol. 103, no. 3, p. 035004, 2021.
- [21] C. A. Manzari, A. M. Coutinho, and A. Crivellin, “Modified lepton couplings and the Cabibbo-angle anomaly,” *PoS*, vol. LHCP2020, p. 242, 2021.
- [22] A. K. Alok, A. Dighe, S. Gangal, and J. Kumar, “The role of non-universal Z couplings in explaining the V_{us} anomaly,” *Nucl. Phys. B*, vol. 971, p. 115538, 2021.
- [23] A. Crivellin, C. A. Manzari, M. Alguero, and J. Matias, “Combined Explanation of the $Z \rightarrow b\bar{b}$ Forward-Backward Asymmetry, the Cabibbo Angle Anomaly, and $\tau \rightarrow \mu\nu\nu$ and $b \rightarrow s\ell_+l_-$ Data,” *Phys. Rev. Lett.*, vol. 127, no. 1, p. 011801, 2021.
- [24] A. Crivellin, F. Kirk, C. A. Manzari, and L. Panizzi, “Searching for lepton flavor universality violation and collider signals from a singly charged scalar singlet,” *Phys. Rev. D*, vol. 103, no. 7, p. 073002, 2021.
- [25] A. Crivellin, M. Hoferichter, and C. A. Manzari, “Fermi Constant from Muon Decay Versus Electroweak Fits and Cabibbo-Kobayashi-Maskawa Unitarity,” *Phys. Rev. Lett.*, vol. 127, no. 7, p. 071801, 2021.
- [26] D. Marzocca and S. Trifinopoulos, “Minimal Explanation of Flavor Anomalies: B-Meson Decays, Muon Magnetic Moment, and the Cabibbo Angle,” *Phys. Rev. Lett.*, vol. 127, no. 6, p. 061803, 2021.

- [27] O. Fischer *et al.*, “Unveiling hidden physics at the LHC,” *Eur. Phys. J. C*, vol. 82, no. 8, p. 665, 2022.
- [28] F. J. Botella, G. C. Branco, M. N. Rebelo, J. I. Silva-Marcos, and J. F. Bastos, “Decays of the heavy top and new insights on ϵ_K in a one-VLQ minimal solution to the CKM unitarity problem,” *Eur. Phys. J. C*, vol. 82, no. 4, p. 360, 2022. [Erratum: *Eur.Phys.J.C* 82, 423 (2022)].
- [29] G. C. Branco, J. F. Bastos, and J. I. Silva-Marcos, “Do the small numbers in the quark mixing arise from new physics?,” *Eur. Phys. J. C*, vol. 83, no. 2, p. 141, 2023.
- [30] A. Crivellin, M. Kirk, T. Kitahara, and F. Mescia, “Global fit of modified quark couplings to EW gauge bosons and vector-like quarks in light of the Cabibbo angle anomaly,” *JHEP*, vol. 03, p. 234, 2023.
- [31] K. S. Babu and R. Dcruz, “Resolving **W** Boson Mass Shift and CKM Unitarity Violation in Left-Right Symmetric Models with Universal Seesaw,” 12 2022.
- [32] B. Belfatto and S. Trifinopoulos, “Cabibbo angle anomalies and oblique corrections: The remarkable role of the vectorlike quark doublet,” *Phys. Rev. D*, vol. 108, no. 3, p. 035022, 2023.
- [33] J. M. Alves, G. Branco, A. Cherchiglia, C. Nishi, J. Penedo, P. M. Pereira, M. Rebelo, and J. Silva-Marcos, “Vector-like singlet quarks: A roadmap,” *Physics Reports*, vol. 1057, pp. 1–69, 2024.
- [34] S. L. Glashow, J. Iliopoulos, and L. Maiani, “Weak Interactions with Lepton-Hadron Symmetry,” *Phys. Rev. D*, vol. 2, pp. 1285–1292, 1970.
- [35] J. A. Aguilar-Saavedra, R. Benbrik, S. Heinemeyer, and M. Pérez-Victoria, “Handbook of vectorlike quarks: Mixing and single production,” *Phys. Rev. D*, vol. 88, no. 9, p. 094010, 2013.
- [36] N. Aghanim *et al.*, “Planck 2018 results. VI. Cosmological parameters,” *Astron. Astrophys.*, vol. 641, p. A6, 2020. [Erratum: *Astron.Astrophys.* 652, C4 (2021)].
- [37] R. L. Workman *et al.*, “Review of Particle Physics,” *PTEP*, vol. 2022, p. 083C01, 2022.
- [38] P. O. Ludl and W. Grimus, “A complete survey of texture zeros in the lepton mass matrices,” *JHEP*, vol. 07, p. 090, 2014. [Erratum: *JHEP* 10, 126 (2014)].
- [39] P. O. Ludl and W. Grimus, “A complete survey of texture zeros in general and symmetric quark mass matrices,” *Phys. Lett. B*, vol. 744, pp. 38–42, 2015.
- [40] R. Gonzalez Felipe and H. Serodio, “Maximally restrictive leptonic texture zeros in two-Higgs-doublet models,” *J. Phys. G*, vol. 44, no. 6, p. 065002, 2017.
- [41] L. M. Cebola, D. Emmanuel-Costa, and R. G. Felipe, “Confronting predictive texture zeros in lepton mass matrices with current data,” *Phys. Rev. D*, vol. 92, no. 2, p. 025005, 2015.
- [42] W. Grimus, A. S. Joshipura, L. Lavoura, and M. Tanimoto, “Symmetry realization of texture zeros,” *Eur. Phys. J. C*, vol. 36, pp. 227–232, 2004.

- [43] A. Dighe and N. Sahu, “Texture zeroes and discrete flavor symmetries in light and heavy Majorana neutrino mass matrices: a bottom-up approach,” 1 2009.
- [44] B. Adhikary, A. Ghosal, and P. Roy, “mu tau symmetry, tribimaximal mixing and four zero neutrino Yukawa textures,” *JHEP*, vol. 10, p. 040, 2009.
- [45] P. M. Ferreira and J. P. Silva, “Abelian symmetries in the two-Higgs-doublet model with fermions,” *Phys. Rev. D*, vol. 83, p. 065026, 2011.
- [46] R. González Felipe and H. Serôdio, “Abelian realization of phenomenological two-zero neutrino textures,” *Nucl. Phys. B*, vol. 886, pp. 75–92, 2014.
- [47] R. Samanta and A. Ghosal, “Probing maximal zero textures with broken cyclic symmetry in inverse seesaw,” *Nucl. Phys. B*, vol. 911, pp. 846–862, 2016.
- [48] T. Kobayashi, T. Nomura, and H. Okada, “Predictive neutrino mass textures with origin of flavor symmetries,” *Phys. Rev. D*, vol. 98, no. 5, p. 055025, 2018.
- [49] M. H. Rahat, P. Ramond, and B. Xu, “Asymmetric tribimaximal texture,” *Phys. Rev. D*, vol. 98, no. 5, p. 055030, 2018.
- [50] N. Nath, “ $\mu - \tau$ reflection symmetry and its explicit breaking for leptogenesis in a minimal seesaw model,” *Mod. Phys. Lett. A*, vol. 34, no. 39, p. 1950329, 2019.
- [51] D. M. Barreiros, R. G. Felipe, and F. R. Joaquim, “Minimal type-I seesaw model with maximally restricted texture zeros,” *Phys. Rev. D*, vol. 97, no. 11, p. 115016, 2018.
- [52] D. M. Barreiros, R. G. Felipe, and F. R. Joaquim, “Combining texture zeros with a remnant CP symmetry in the minimal type-I seesaw,” *JHEP*, vol. 01, p. 223, 2019.
- [53] S. S. Correia, R. G. Felipe, and F. R. Joaquim, “Dirac neutrinos in the 2HDM with restrictive Abelian symmetries,” *Phys. Rev. D*, vol. 100, no. 11, p. 115008, 2019.
- [54] H. B. Camara, R. G. Felipe, and F. R. Joaquim, “Minimal inverse-seesaw mechanism with Abelian flavour symmetries,” *JHEP*, vol. 05, p. 021, 2021.
- [55] D. M. Barreiros, F. R. Joaquim, R. Srivastava, and J. W. F. Valle, “Minimal scoto-seesaw mechanism with spontaneous CP violation,” *JHEP*, vol. 04, p. 249, 2021.
- [56] D. M. Barreiros, H. B. Camara, and F. R. Joaquim, “Flavour and dark matter in a scoto/type-II seesaw model,” *JHEP*, vol. 08, p. 030, 2022.
- [57] G. C. Branco, P. M. Ferreira, L. Lavoura, M. N. Rebelo, M. Sher, and J. P. Silva, “Theory and phenomenology of two-Higgs-doublet models,” *Phys. Rept.*, vol. 516, pp. 1–102, 2012.
- [58] C.-N. Yang and R. L. Mills, “Conservation of Isotopic Spin and Isotopic Gauge Invariance,” *Phys. Rev.*, vol. 96, pp. 191–195, 1954.

- [59] S. Glashow, “Partial Symmetries of Weak Interactions,” *Nucl. Phys.*, vol. 22, pp. 579–588, 1961.
- [60] Y. Nambu and G. Jona-Lasinio, “Dynamical model of elementary particles based on an analogy with superconductivity. i,” *Phys. Rev.*, vol. 122, pp. 345–358, Apr 1961.
- [61] Y. Nambu and G. Jona-Lasinio, “Dynamical model of elementary particles based on an analogy with superconductivity. ii,” *Phys. Rev.*, vol. 124, pp. 246–254, Oct 1961.
- [62] J. Goldstone, “Field Theories with Superconductor Solutions,” *Nuovo Cim.*, vol. 19, pp. 154–164, 1961.
- [63] A. Salam, “Weak and Electromagnetic Interactions,” *Conf. Proc. C*, vol. 680519, pp. 367–377, 1968.
- [64] S. Weinberg, “A Model of Leptons,” *Phys. Rev. Lett.*, vol. 19, pp. 1264–1266, 1967.
- [65] M. Gell-Mann, “A Schematic Model of Baryons and Mesons,” *Phys. Lett.*, vol. 8, pp. 214–215, 1964.
- [66] G. Zweig, *An $SU(3)$ model for strong interaction symmetry and its breaking. Version 2*, pp. 22–101. 2 1964.
- [67] G. ’t Hooft, “Renormalizable Lagrangians for Massive Yang-Mills Fields,” *Nucl. Phys. B*, vol. 35, pp. 167–188, 1971.
- [68] G. ’t Hooft and M. Veltman, “Regularization and Renormalization of Gauge Fields,” *Nucl. Phys. B*, vol. 44, pp. 189–213, 1972.
- [69] F. Feruglio, “Pieces of the Flavour Puzzle,” *Eur. Phys. J. C*, vol. 75, no. 8, p. 373, 2015.
- [70] T. Nakano and K. Nishijima, “Charge Independence for V-particles,” *Prog. Theor. Phys.*, vol. 10, pp. 581–582, 1953.
- [71] J. Erler and M. Schott, “Electroweak Precision Tests of the Standard Model after the Discovery of the Higgs Boson,” *Prog. Part. Nucl. Phys.*, vol. 106, pp. 68–119, 2019.
- [72] C.-Y. Seng, D. Galviz, M. Gorchtein, and U.-G. Meißner, “Complete theory of radiative corrections to K_{l3} decays and the V_{us} update,” *JHEP*, vol. 07, p. 071, 2022.
- [73] Y. Aoki *et al.*, “FLAG Review 2021,” *Eur. Phys. J. C*, vol. 82, no. 10, p. 869, 2022.
- [74] J. C. Hardy and I. S. Towner, “Superaligned $0^+ \rightarrow 0^+$ nuclear β decays: 2014 critical survey, with precise results for V_{ud} and CKM unitarity,” *Phys. Rev. C*, vol. 91, no. 2, p. 025501, 2015.
- [75] J. C. Hardy and I. S. Towner, “Superaligned $0^+ \rightarrow 0^+$ nuclear β decays: 2020 critical survey, with implications for V_{ud} and CKM unitarity,” *Phys. Rev. C*, vol. 102, no. 4, p. 045501, 2020.
- [76] W. J. Marciano and A. Sirlin, “Improved calculation of electroweak radiative corrections and the value of $V(\text{ud})$,” *Phys. Rev. Lett.*, vol. 96, p. 032002, 2006.
- [77] I. S. Towner and J. C. Hardy, “The evaluation of $V(\text{ud})$ and its impact on the unitarity of the Cabibbo-Kobayashi-Maskawa quark-mixing matrix,” *Rept. Prog. Phys.*, vol. 73, p. 046301, 2010.

- [78] T. Kitahara and K. Tobioka, “MeV Sterile Neutrino in light of the Cabibbo-Angle Anomaly,” 8 2023.
- [79] V. Cirigliano, A. Crivellin, M. Hoferichter, and M. Moulson, “Scrutinizing CKM unitarity with a new measurement of the $K\mu 3/K\mu 2$ branching fraction,” *Phys. Lett. B*, vol. 838, p. 137748, 2023.
- [80] T. Felkl, J. Herrero-Garcia, and M. A. Schmidt, “The Singly-Charged Scalar Singlet as the Origin of Neutrino Masses,” *JHEP*, vol. 05, p. 122, 2021. [Erratum: *JHEP* 05, 073 (2022)].
- [81] A. Crivellin, M. Hoferichter, M. Kirk, C. A. Manzari, and L. Schnell, “First-generation new physics in simplified models: from low-energy parity violation to the LHC,” *JHEP*, vol. 10, p. 221, 2021.
- [82] V. Cirigliano, D. Díaz-Calderón, A. Falkowski, M. González-Alonso, and A. Rodríguez-Sánchez, “Semileptonic tau decays beyond the Standard Model,” *JHEP*, vol. 04, p. 152, 2022.
- [83] D. Bryman, V. Cirigliano, A. Crivellin, and G. Inguglia, “Testing Lepton Flavor Universality with Pion, Kaon, Tau, and Beta Decays,” *Ann. Rev. Nucl. Part. Sci.*, vol. 72, pp. 69–91, 2022.
- [84] G. Aad *et al.*, “Search for pair production of heavy top-like quarks decaying to a high-pT W boson and a b quark in the lepton plus jets final state at $\sqrt{s}=7$ TeV with the ATLAS detector,” *Phys. Lett. B*, vol. 718, pp. 1284–1302, 2013.
- [85] S. Chatrchyan *et al.*, “Search for Pair Produced Fourth-Generation Up-Type Quarks in pp Collisions at $\sqrt{s} = 7$ TeV with a Lepton in the Final State,” *Phys. Lett. B*, vol. 718, pp. 307–328, 2012.
- [86] O. Eberhardt, G. Herbert, H. Lacker, A. Lenz, A. Menzel, U. Nierste, and M. Wiebusch, “Impact of a Higgs boson at a mass of 126 GeV on the standard model with three and four fermion generations,” *Phys. Rev. Lett.*, vol. 109, p. 241802, 2012.
- [87] S. L. Adler, “Axial-vector vertex in spinor electrodynamics,” *Phys. Rev.*, vol. 177, pp. 2426–2438, Jan 1969.
- [88] G. ’t Hooft, “Symmetry breaking through bell-jackiw anomalies,” *Phys. Rev. Lett.*, vol. 37, pp. 8–11, Jul 1976.
- [89] C. Bouchiat, J. Iliopoulos, and P. Meyer, “An anomaly-free version of weinberg’s model,” *Physics Letters B*, vol. 38, no. 7, pp. 519–523, 1972.
- [90] F. del Aguila, M. Perez-Victoria, and J. Santiago, “Observable contributions of new exotic quarks to quark mixing,” *JHEP*, vol. 09, p. 011, 2000.
- [91] F. J. Botella and L.-L. Chau, “Anticipating the Higher Generations of Quarks from Rephasing Invariance of the Mixing Matrix,” *Phys. Lett. B*, vol. 168, pp. 97–104, 1986.
- [92] N. R. Agostinho, G. C. Branco, P. M. F. Pereira, M. N. Rebelo, and J. I. Silva-Marcos, “Can one have significant deviations from leptonic 3×3 unitarity in the framework of type I seesaw mechanism?,” *Eur. Phys. J. C*, vol. 78, no. 11, p. 895, 2018.

- [93] G. C. Branco, J. T. Penedo, P. M. F. Pereira, M. N. Rebelo, and J. I. Silva-Marcos, “Type-I Seesaw with eV-Scale Neutrinos,” *JHEP*, vol. 07, p. 164, 2020.
- [94] M. Aaboud *et al.*, “Combination of the searches for pair-produced vector-like partners of the third-generation quarks at $\sqrt{s} = 13$ TeV with the ATLAS detector,” *Phys. Rev. Lett.*, vol. 121, no. 21, p. 211801, 2018.
- [95] L. Panizzi, “Vector-like quarks: t' and partners,” *Nuovo Cim. C*, vol. 037, no. 02, pp. 69–79, 2014.
- [96] H. Dembinski and P. O. et al., “scikit-hep/iminuit,” Dec 2020.
- [97] F. James and M. Roos, “Minuit: A System for Function Minimization and Analysis of the Parameter Errors and Correlations,” *Comput. Phys. Commun.*, vol. 10, pp. 343–367, 1975.
- [98] A. M. Sirunyan *et al.*, “Search for vector-like T and B quark pairs in final states with leptons at $\sqrt{s} = 13$ TeV,” *JHEP*, vol. 08, p. 177, 2018.
- [99] H. Serôdio, “Yukawa sector of Multi Higgs Doublet Models in the presence of Abelian symmetries,” *Phys. Rev. D*, vol. 88, no. 5, p. 056015, 2013.
- [100] I. P. Ivanov, V. Keus, and E. Vdovin, “Abelian symmetries in multi-Higgs-doublet models,” *J. Phys. A*, vol. 45, p. 215201, 2012.
- [101] I. P. Ivanov and C. C. Nishi, “Abelian symmetries of the N-Higgs-doublet model with Yukawa interactions,” *JHEP*, vol. 11, p. 069, 2013.
- [102] T. Inami and C. S. Lim, “Effects of Superheavy Quarks and Leptons in Low-Energy Weak Processes $K_L \rightarrow \mu\mu$, $K^+ \rightarrow \pi + \nu\nu$ and $K^0 \leftrightarrow \bar{K}^0$,” *Progress of Theoretical Physics*, vol. 65, pp. 297–314, 01 1981.
- [103] G. Buchalla, A. J. Buras, and M. E. Lautenbacher, “Weak decays beyond leading logarithms,” *Rev. Mod. Phys.*, vol. 68, pp. 1125–1144, 1996.
- [104] J. A. Aguilar-Saavedra, “Effects of mixing with quark singlets,” *Phys. Rev. D*, vol. 67, p. 035003, 2003. [Erratum: *Phys.Rev.D* 69, 099901 (2004)].
- [105] G. C. Branco, L. Lavoura, and J. P. Silva, *CP Violation*, vol. 103. 1999.
- [106] V. Weisskopf and E. P. Wigner, “Calculation of the natural brightness of spectral lines on the basis of Dirac’s theory,” *Z. Phys.*, vol. 63, pp. 54–73, 1930.
- [107] J. Brod, M. Gorbahn, and E. Stamou, “Standard-Model Prediction of ϵ_K with Manifest Quark-Mixing Unitarity,” *Phys. Rev. Lett.*, vol. 125, no. 17, p. 171803, 2020.
- [108] A. Lenz, U. Nierste, J. Charles, S. Descotes-Genon, H. Lacker, S. Monteil, V. Niess, and S. T’Jampens, “Constraints on new physics in $b - \bar{B}$ mixing in the light of recent lhcb data,” *Phys. Rev. D*, vol. 86, p. 033008, Aug 2012.

- [109] L. Wolfenstein, “D0d0 mixing,” *Physics Letters B*, vol. 164, no. 1, pp. 170–172, 1985.
- [110] A. J. Buras and D. Guadagnoli, “Correlations among new CP violating effects in $\Delta F = 2$ observables,” *Phys. Rev. D*, vol. 78, p. 033005, 2008.
- [111] G. Buchalla and A. J. Buras, “QCD corrections to rare K and B decays for arbitrary top quark mass,” *Nucl. Phys. B*, vol. 400, pp. 225–239, 1993.
- [112] G. Eilam, J. L. Hewett, and A. Soni, “Rare decays of the top quark in the standard and two-higgs-doublet models,” *Phys. Rev. D*, vol. 44, pp. 1473–1484, Sep 1991.
- [113] F. J. Botella, G. C. Branco, and M. Nebot, “Singlet Heavy Fermions as the Origin of B Anomalies in Flavour Changing Neutral Currents,” 12 2017.
- [114] E. Nardi, “Top - charm flavor changing contributions to the effective $b s Z$ vertex,” *Phys. Lett. B*, vol. 365, pp. 327–333, 1996.
- [115] P. N. Kopnin and M. I. Vysotsky, “Manifestation of a singlet heavy up-type quark in the branching ratios of rare decays $K \rightarrow \pi \nu \text{ anti-}\nu$, $B \rightarrow \pi \nu \text{ anti-}\nu$ and $B \rightarrow K \nu \text{ anti-}\nu$,” *JETP Lett.*, vol. 87, pp. 517–523, 2008.
- [116] I. Picek and B. Radovic, “Nondecoupling of terascale isosinglet quark and rare K- and B-decays,” *Phys. Rev. D*, vol. 78, p. 015014, 2008.
- [117] A. J. Buras, J. Girrbach, D. Guadagnoli, and G. Isidori, “On the Standard Model prediction for $BR(B_{s,d} \rightarrow \mu^+ \mu^-)$,” *Eur. Phys. J. C*, vol. 72, p. 2172, 2012.
- [118] W. J. Marciano and Z. Parsa, “Rare kaon decays with “missing energy”,” *Phys. Rev. D*, vol. 53, pp. R1–R5, Jan 1996.
- [119] G. Buchalla and A. J. Buras, “The rare decays $K \rightarrow \pi \nu \bar{\nu}$, $B \rightarrow X \nu \bar{\nu}$ and $B \rightarrow l^+ l^-$: An Update,” *Nucl. Phys. B*, vol. 548, pp. 309–327, 1999.
- [120] G. Isidori and R. Unterdorfer, “On the short-distance constraints from $k_{L,S} \rightarrow \mu + \mu^-$,” *Journal of High Energy Physics*, vol. 2004, p. 009, jan 2004.
- [121] A. J. Buras, S. Uhlig, and F. Schwab, “Waiting for precise measurements of $K^+ \rightarrow \pi^+ \nu \bar{\nu}$ and $K_L \rightarrow \pi^0 \nu \bar{\nu}$,” *Rev. Mod. Phys.*, vol. 80, pp. 965–1007, Aug 2008.
- [122] J. H. Christenson, J. W. Cronin, V. L. Fitch, and R. Turlay, “Evidence for the 2π decay of the k_2^0 meson,” *Phys. Rev. Lett.*, vol. 13, pp. 138–140, Jul 1964.
- [123] G. Buchalla, A. J. Buras, and M. K. Harlander, “Penguin box expansion: Flavor changing neutral current processes and a heavy top quark,” *Nucl. Phys. B*, vol. 349, pp. 1–47, 1991.
- [124] J. Aebischer, C. Bobeth, and A. J. Buras, “ ϵ'/ϵ in the Standard Model at the Dawn of the 2020s,” *Eur. Phys. J. C*, vol. 80, no. 8, p. 705, 2020.

Appendix A

Non-realisable texture pairs

The equations (4.10) result in the following general constraints on the patterns of texture zeros:

- (1) The columns of non-zero entries in the fourth row of \mathbf{M}_u must have the same texture zeros:

$$x_{T_L} - x_{u_{Ri}} = 0 \wedge x_{T_L} - x_{u_{Rj}} = 0 \implies x_{u_{Ri}} = x_{u_{Rj}}; \quad (\text{A.1})$$

- (2) If a Higgs field accounts for more than one non-zero entry in a given row (column) in \mathbf{M}_d or $\mathbf{M}_u^{\text{Yuk.}}$, then the columns (rows) corresponding to these non-zero entries have the same texture zeros ¹:

$$\begin{aligned} \text{row: } & x_{q_{Li}} - x_{d_{Rj}} - x_{\Phi_k} = 0 \wedge x_{q_{Li}} - x_{d_{Rn}} - x_{\Phi_k} = 0 \implies x_{d_{Rj}} = x_{d_{Rn}}, \\ \text{column: } & x_{q_{Li}} - x_{d_{Rj}} - x_{\Phi_k} = 0 \wedge x_{q_{Ln}} - x_{d_{Rj}} - x_{\Phi_k} = 0 \implies x_{q_{Li}} = x_{q_{Ln}}. \end{aligned} \quad (\text{A.2})$$

The conditions (A.1) and (A.2) allow the independent inspection of the quark matrices presented in Sec. 4.1. For clarity, we analyse the textures represented below in detail to showcase these arguments.

$\begin{pmatrix} 0 & 0 & 0 & \times \\ 0 & \times & \times & 0 \\ \times & \times & \times & 0 \\ 0 & 0 & \times & \times \end{pmatrix}$	$\begin{pmatrix} \times & 0 & 0 & \times \\ 0 & \times & \times & 0 \\ \times & \times & \times & 0 \\ 0 & 0 & \times & 0 \end{pmatrix}$	$\begin{pmatrix} \times & 0 & 0 & \times \\ 0 & \times & \times & 0 \\ 0 & \times & \times & 0 \\ 0 & 0 & \times & \times \end{pmatrix}$	$\begin{pmatrix} 0 & 0 & 0 & \times \\ 0 & 2 & 2 & 0 \\ 2 & 1 & 1 & 0 \\ 0 & \times & \times & 0 \end{pmatrix}$
(1) ✗	(1) ✓	(1) ✗	(1) ✓
(2) ✗	(2) ✗	(2) ✓	(2) ✓

The first texture, which corresponds to 8_{13}^u , cannot be explained with Abelian symmetries within a 2HDM. Firstly, the non-zero entries in the fourth row have different column textures. Furthermore, since we are considering a 2HDM, at least two non-zero entries in the third row must couple to the same Higgs field, therefore presenting identical columns. The remaining three textures are obtained by swapping one texture zero by one non-zero entry in 8_{13}^u . The second texture only violates (A.2), since the fourth row only has one non-zero entry. Regarding the third texture, the first three rows verify (A.2), but the

¹Recall the definition of $\mathbf{M}_u^{\text{Yuk.}}$ in Eq. (4.7). The condition (A.2) is similar for the case of up-type quarks.

(1) ✓ (2) ✓	9_9^u $10_1^u 10_3^u$ 11_1^u
(1) ✓ (2) ✗	$8_1^u 8_2^u 8_3^u 8_{11}^u 8_{17}^u$ $9_3^u 9_4^u 9_5^u 9_6^u 9_8^u 9_{16}^u$ 10_5^u
(1) ✗ (2) ✓	$8_4^u 8_7^u 8_{10}^u 8_{12}^u 8_{14}^u 8_{15}^u 8_{18}^u 8_{19}^u 8_{20}^u 8_{24}^u 8_{27}^u$ $9_1^u 9_2^u 9_7^u 9_{10}^u 9_{11}^u 9_{12}^u 9_{13}^u 9_{14}^u 9_{15}^u 9_{19}^u 9_{20}^u$ $10_2^u 10_4^u 10_6^u 10_7^u 10_8^u$ 11_2^u
(1) ✗ (2) ✗	$8_5^u 8_6^u 8_8^u 8_9^u 8_{13}^u 8_{16}^u 8_{21}^u 8_{22}^u 8_{23}^u 8_{25}^u 8_{26}^u$ $9_{17}^u 9_{18}^u 9_{21}^u 9_{22}^u 9_{23}^u$

Table A.1: Classification of textures for the full 4×4 up-type quark mass matrix under conditions (A.1) and (A.2).

(2) ✓	$3_1^d 3_2^d 3_3^d$ $4_1^d 4_2^d 4_3^d 4_6^d 4_7^d 4_{11}^d$ $5_1^d 5_2^d 5_3^d 5_4^d 5_5^d 5_6^d$ 6_1^d
(2) ✗	$4_4^d 4_5^d 4_8^d 4_9^d 4_{10}^d 4_{12}^d$

Table A.2: Classification of textures for the 3×3 SM down-type quark mass matrix under conditions (A.1) and (A.2).

fourth row contains non-zero entries with distinct column textures. Finally, the fourth texture complies with both requirements: both non-zero entries in the last row have the same column texture; two of the non-zero entries in the third row have identical columns. In this case, (A.2) imposes the only possible decomposition of the mass matrix into Yukawa matrices ², where the 1 and 2 entries correspond to non-zero entries explained by Φ_1 and Φ_2 , respectively.

The mass matrices identified in Sec. 4.1 and respective classification under conditions (A.1) and (A.2) are presented in Tables A.1 and A.2. This procedure reduces the 237 maximally-restrictive $(\mathcal{M}_u, \mathbf{M}_d)$ texture-zeros pairs identified in Tables 4.3 and 4.2 to 20 pairs consistent with both requirements. However, we have not yet considered the interplay between the textures of a given pair. Suppose that a column j of M_d has two non-zeros entries in rows i and k coupled to distinct Higgs doublets Φ_a , i.e. $(\mathbf{Y}_d^1)_{ij} \neq 0$ and $(\mathbf{Y}_d^2)_{kj} \neq 0$. This imposes the relation $x_{q_{Li}} - x_{\Phi_1} = x_{q_{Lk}} - x_{\Phi_2}$. The quark doublets q_{Li} couple to both up and down-type RH quarks [see Eq. (4.6)]. Thus, further assuming that \mathcal{M}_u has a non-zero entry in row i coupled to Φ_2 , we get the relation $x_{q_{Li}} - x_{u_{Rn}} + x_{\Phi_2} = x_{q_{Lk}} - x_{u_{Rn}} + x_{\Phi_1} = 0$ for $n = 1, 2, 3, 4$. The last equality demonstrates that $(\mathbf{Y}_u^1)_{kn} \neq 0$ if $(\mathbf{Y}_u^2)_{in} \neq 0$. This reasoning leads to a third prerequisite for a $(\mathcal{M}_u, \mathbf{M}_d)$ pair to be realisable via Abelian symmetries:

- (3) If $(\mathbf{Y}_d^1)_{ij} \neq 0$ and $(\mathbf{Y}_d^2)_{kj} \neq 0$, where $i, j, k = 1, 2, 3$ with $j \neq k$, then

$$(\mathbf{Y}_u^2)_{in} \neq 0 \iff (\mathbf{Y}_u^1)_{kn} \neq 0, \quad n = 1, 2, 3, 4, \quad (\text{A.3})$$

²Recall that the subscript $a = 1, 2$ is simply a label, i.e. the Lagrangian is invariant under $\Phi_1 \leftrightarrow \Phi_2$.

where we consider $x_{u_{R4}} \equiv x_{T_R}$.

The requirements (A.1) and (A.2) determine the possible decompositions of the quark mass matrix textures into Yukawa matrices. The contrapositive statement of (A.2) states that if the columns (rows) of two non-zero entries in a given row (column) of \mathbf{M}_d or $\mathbf{M}_u^{\text{Yuk.}}$ have distinct texture zeros, then these non-zero entries must be generated by distinct Higgs fields. This criteria produces the decompositions represented in Table A.3, where the entries 1 and 2 correspond to non-zero entries coupled to Φ_1 and Φ_2 , respectively. The \times entries of textures 11^u and 5^d correspond to non-zeros that may couple to either Φ_a . Since the Lagrangian is invariant under $\Phi_1 \leftrightarrow \Phi_2$ [see Eq. (4.6)], we ignore decompositions of \mathbf{M}_d obtained by the transformation $1 \leftrightarrow 2$, to eliminate redundancy when considering the pairings $(\mathcal{M}_u, \mathbf{M}_d)$.

To exemplify the application of criteria (A.3), consider the texture pair $(10_1^u, 4_1^d)$, which verifies (A.1) and (A.2). The first column of 4_1^d and the columns of 10_{1A}^u verify (A.3). However, the first and fourth column of 10_{1A}^u are in conflict with the third column of 4_1^d :

$$4_1^d \sim \begin{pmatrix} 0 & 1 & \textcolor{blue}{2} \\ 1 & 0 & 0 \\ 2 & 0 & \textcolor{blue}{1} \end{pmatrix}, \quad 10_{1A}^u \sim \begin{pmatrix} \textcolor{red}{1} & 0 & 0 & 1 \\ 0 & 1 & 2 & 0 \\ 2 & 0 & 1 & \textcolor{red}{2} \end{pmatrix}, \quad (\text{A.4})$$

where we represent the needed “corrections” for the pair of textures to comply with (A.3) in red ³. Following this notation, we present the analysis between 4_1^d and the remaining decompositions 10_{1B}^u , 10_{1C}^u and 10_{1D}^u .

$$4_1^d \sim \begin{pmatrix} 0 & 1 & 2 \\ \textcolor{blue}{1} & 0 & 0 \\ \textcolor{blue}{2} & 0 & 1 \end{pmatrix}, \quad 10_{1B}^u \sim \begin{pmatrix} 0 & 0 & 0 & 1 \\ \textcolor{red}{2} & 2 & 1 & 0 \\ 1 & \textcolor{red}{1} & 2 & 0 \end{pmatrix}, \quad \text{and } 4_1^d \sim \begin{pmatrix} 0 & 1 & \textcolor{blue}{2} \\ 1 & 0 & 0 \\ 2 & 0 & \textcolor{blue}{1} \end{pmatrix}, \quad 10_{1B}^u \sim \begin{pmatrix} 0 & 0 & \textcolor{red}{1} & 1 \\ 0 & 2 & 1 & 0 \\ 1 & 0 & 2 & \textcolor{red}{2} \end{pmatrix}, \quad (\text{A.5})$$

$$4_1^d \sim \begin{pmatrix} 0 & 1 & \textcolor{blue}{2} \\ 1 & 0 & 0 \\ 2 & 0 & \textcolor{blue}{1} \end{pmatrix}, \quad 10_{1C}^u \sim \begin{pmatrix} \textcolor{red}{1} & 0 & 0 & 2 \\ 0 & 1 & 2 & 0 \\ 2 & 0 & 1 & 0 \end{pmatrix}, \quad (\text{A.6})$$

$$4_1^d \sim \begin{pmatrix} 0 & 1 & 2 \\ \textcolor{blue}{1} & 0 & 0 \\ \textcolor{blue}{2} & 0 & 1 \end{pmatrix}, \quad 10_{1D}^u \sim \begin{pmatrix} 0 & 0 & 0 & 2 \\ \textcolor{red}{2} & 2 & 1 & 0 \\ 1 & \textcolor{red}{1} & 2 & 0 \end{pmatrix}, \quad \text{and } 4_1^d \sim \begin{pmatrix} 0 & 1 & \textcolor{blue}{2} \\ 1 & 0 & 0 \\ 2 & 0 & \textcolor{blue}{1} \end{pmatrix}, \quad 10_{1D}^u \sim \begin{pmatrix} 0 & 0 & \textcolor{red}{1} & 2 \\ 0 & 2 & 1 & 0 \\ 1 & 0 & 2 & 0 \end{pmatrix}. \quad (\text{A.7})$$

The condition (A.3) reduces the remaining 20 pairs consistent with (A.1) and (A.2) to just the two decompositions represented in Table 4.9. Defining the notation:

$$[i : j] \equiv \text{column } i \text{ of } \mathbf{M}_d \text{ incompatible under (A.3) with column } j \text{ of } \mathbf{M}_u^{\text{Yuk.}}. \quad (\text{A.8})$$

³There are multiple ways of “correcting” the textures. We choose to add the needed non-zero to elucidate the reasoning behind condition (A.3).

$3_1^d \sim \begin{pmatrix} 0 & 2 & 1 \\ 1 & 0 & 2 \\ 0 & 2 & 1 \end{pmatrix}$	$3_2^d \sim \begin{pmatrix} 0 & 2 & 1 \\ 0 & 2 & 1 \\ 1 & 0 & 2 \end{pmatrix}$		
$4_1^d \sim \begin{pmatrix} 0 & 1 & 2 \\ 1 & 0 & 0 \\ 2 & 0 & 1 \end{pmatrix}$	$4_2^d \sim \begin{pmatrix} 0 & 0 & 1 \\ 1 & 2 & 0 \\ 0 & 1 & 2 \end{pmatrix}$	$4_3^d \sim \begin{pmatrix} 0 & 1 & 2 \\ 0 & 0 & 1 \\ 1 & 2 & 0 \end{pmatrix}$	$4_6^d \sim \begin{pmatrix} 0 & 1 & 2 \\ 2 & 0 & 1 \\ 1 & 0 & 0 \end{pmatrix}$
$4_7^d \sim \begin{pmatrix} 0 & 0 & 1 \\ 0 & 1 & 2 \\ 1 & 2 & 0 \end{pmatrix}$	$4_{11}^d \sim \begin{pmatrix} 0 & 1 & 2 \\ 2 & 0 & 1 \\ 0 & 2 & 0 \end{pmatrix}$		
$5_1^d \sim \begin{pmatrix} 0 & 0 & 1 \\ 0 & \times & 0 \\ 1 & 0 & 2 \end{pmatrix}$	$5_2^d \sim \begin{pmatrix} 0 & 0 & \times \\ 0 & 1 & 0 \\ 1 & 2 & 0 \end{pmatrix}$	$5_3^d \sim \begin{pmatrix} 0 & 0 & 1 \\ 0 & 1 & 2 \\ \times & 0 & 0 \end{pmatrix}$	$5_4^d \sim \begin{pmatrix} 0 & 1 & 2 \\ \times & 0 & 0 \\ 0 & 0 & 1 \end{pmatrix}$
$5_5^d \sim \begin{pmatrix} 0 & 1 & 2 \\ 0 & 0 & 1 \\ \times & 0 & 0 \end{pmatrix}$	$5_6^d \sim \begin{pmatrix} 0 & 0 & \times \\ 1 & 2 & 0 \\ 0 & 1 & 0 \end{pmatrix}$		
$9_{9A}^u \sim \begin{pmatrix} 0 & 0 & 1 & 2 \\ 0 & 2 & 0 & 1 \\ 1 & 0 & 2 & 0 \end{pmatrix}$	$9_{9B}^u \sim \begin{pmatrix} 0 & 0 & 2 & 1 \\ 0 & 1 & 0 & 2 \\ 2 & 0 & 1 & 0 \end{pmatrix}$		
$10_{1A}^u \sim \begin{pmatrix} 0 & 0 & 0 & 1 \\ 0 & 1 & 2 & 0 \\ 2 & 0 & 1 & 0 \end{pmatrix}$	$10_{1B}^u \sim \begin{pmatrix} 0 & 0 & 0 & 1 \\ 0 & 2 & 1 & 0 \\ 1 & 0 & 2 & 0 \end{pmatrix}$	$10_{1C}^u \sim \begin{pmatrix} 0 & 0 & 0 & 2 \\ 0 & 1 & 2 & 0 \\ 2 & 0 & 1 & 0 \end{pmatrix}$	$10_{1D}^u \sim \begin{pmatrix} 0 & 0 & 0 & 2 \\ 0 & 2 & 1 & 0 \\ 1 & 0 & 2 & 0 \end{pmatrix}$
$10_{3A}^u \sim \begin{pmatrix} 0 & 0 & 0 & 1 \\ 0 & 0 & 1 & 2 \\ 1 & 2 & 0 & 0 \end{pmatrix}$	$10_{3B}^u \sim \begin{pmatrix} 0 & 0 & 0 & 2 \\ 0 & 0 & 2 & 1 \\ 1 & 2 & 0 & 0 \end{pmatrix}$	$10_{3C}^u \sim \begin{pmatrix} 0 & 0 & 0 & 1 \\ 0 & 0 & 1 & 2 \\ 2 & 1 & 0 & 0 \end{pmatrix}$	$10_{3D}^u \sim \begin{pmatrix} 0 & 0 & 0 & 2 \\ 0 & 0 & 2 & 1 \\ 2 & 1 & 0 & 0 \end{pmatrix}$
$11_{1A}^u \sim \begin{pmatrix} 0 & 0 & 0 & \times \\ 0 & 0 & \times & 0 \\ 1 & 2 & 0 & 0 \end{pmatrix}$	$11_{1B}^u \sim \begin{pmatrix} 0 & 0 & 0 & \times \\ 0 & 0 & \times & 0 \\ 2 & 1 & 0 & 0 \end{pmatrix}$		

Table A.3: Possible decompositions of $\mathbf{M}_u^{\text{Yuk.}}$ and \mathbf{M}_d for the textures 10_1^u and 4_1^d . The entries 1 and 2 correspond to non-zero entries coupled to Φ_1 and Φ_2 , respectively. The \times entries of the textures 11^u and 5^d may couple to either Φ_a .

we present in Tables A.4, A.5 and A.6 one incompatibility between each of the textures 11_1^u , 10_1^u , 10_3^u and 9_9^u and the respective forbidden down texture pairings. Using the previous example between 4_1^d and 10_{1A}^u [see Eq. (A.4)], their incompatibility is represented as $[3 : 1]$ and $[3 : 4]$.

	11_{1A}^u	11_{1B}^u
3_1^d	$[3 : 2]$	$[3 : 1]$
3_2^d	$[3 : 1]$	$[3 : 2]$

Table A.4: Incompatibility under (A.3) between each of the decompositions of 11_1^u and the respective forbidden down texture pairings.

	10_{1A}^u	10_{1B}^u	10_{1C}^u	10_{1D}^u	10_{3A}^u	10_{3B}^u	10_{3C}^u	10_{3D}^u
4_1^d	$[3 : 1]$	$[1 : 1]$	$[3 : 1]$	$[1 : 1]$	$[1 : 1]$	$[1 : 1]$	$[1 : 2]$	$[1 : 2]$
4_2^d	$[2 : 2]$	$[3 : 1]$	$[2 : 1]$	$[3 : 1]$	$[2 : 2]$	$[2 : 2]$	$[2 : 1]$	$[2 : 1]$
4_3^d	$[2 : 3]$	$[2 : 1]$	$[2 : 3]$	$[2 : 1]$	$[2 : 1]$	$[2 : 4]$	$[2 : 2]$	$[2 : 2]$
4_6^d	$[1 : 1]$	$[3 : 4]$	$[1 : 1]$	$[3 : 2]$	$[1 : 2]$	$[1 : 2]$	$[1 : 1]$	$[1 : 1]$
4_7^d	$[3 : 2]$	$[2 : 2]$	$[3 : 2]$	$[2 : 1]$	$[2 : 1]$	$[2 : 3]$	$[2 : 2]$	$[2 : 2]$
4_{11}^d	$[3 : 4]$	$[3 : 4]$	$[2 : 3]$	$[2 : 1]$	$[2 : 1]$	$[2 : 1]$	$[2 : 2]$	$[2 : 2]$

Table A.5: Incompatibility under (A.3) between each of the decompositions of 10_1^u and 10_3^u and the respective forbidden down texture pairings.

	9_{9A}^u	9_{9B}^u
5_1^d	$[3 : 4]$	$[2 : 4] \mid \checkmark$
5_2^d	$[2 : 2]$	$[2 : 3]$
5_3^d	$[1 : 3] \mid \checkmark$	$[3 : 3]$
5_4^d	$[2 : 4]$	$[3 : 1]$
5_5^d	$[3 : 3]$	$[2 : 3]$
5_6^d	$[2 : 3]$	$[2 : 2]$

Table A.6: Incompatibility under (A.3) between each of the decompositions of 9_9^u and the respective forbidden down texture pairings. For the pairings $(9_{9A}^u, 5_3^d)$ and $(9_{9B}^u, 5_1^d)$, we present the results for the \times entry of 5^d coupling to $\Phi_1 \mid \Phi_2$. The checkmarks correspond to the decompositions presented in Table 4.9.

Appendix B

Inami-Lim functions

The gauge dependent functions $B_0(x)$, $C_0(x)$ and $D_0(x)$ resulting from the box (see Fig. 5.4), the Z -penguin (see Fig. 5.5) and the electromagnetic penguin diagrams, respectively, are, in the 't Hooft-Feynman gauge:

$$B_0(x) = \frac{1}{4} \left[\frac{x}{1-x} + \frac{x \log x}{(x-1)^2} \right], \quad (\text{B.1})$$

$$C_0(x) = \frac{x}{8} \left[\frac{x-6}{x-1} + \frac{3x+2}{(x-1)^2} \log x \right], \quad (\text{B.2})$$

$$D_0(x) = -\frac{4}{9} \log x + \frac{-19x^3 + 25x^2}{36(x-1)^3} + \frac{x^2(5x^2 - 2x - 6)}{18(x-1)^4} \log x. \quad (\text{B.3})$$

In an arbitrary R_ξ -gauge, these functions are given by:

$$B(x, \xi, T_3) = \begin{cases} B(x) + \frac{1}{8} \bar{\rho}(x, \xi), & T_3 = \frac{1}{2}, \\ B(x) + \frac{1}{2} \bar{\rho}(x, \xi), & T_3 = -\frac{1}{2}, \end{cases} \quad (\text{B.4})$$

$$C(x, \xi) = C(x) + \frac{1}{2} \bar{\rho}(x, \xi), \quad (\text{B.5})$$

$$D(x, \xi) = D(x) - 2 \bar{\rho}(x, \xi), \quad (\text{B.6})$$

where T_3 is the weak isospin of the fermion in the flavour-conserving current of the diagram in Fig. 5.4 and we define:

$$\bar{\rho}(x, \xi) = \rho(x, \xi) - \frac{7}{2} B_0(x), \quad (\text{B.7})$$

$$\begin{aligned} \rho(x, \xi) = & \frac{\xi}{x-\xi} \left(\frac{3}{4} \frac{1}{x-1} + \frac{1}{8} \frac{\xi}{x-\xi} \right) x \log x + \frac{1}{8} \frac{\xi^2}{x-\xi} \left[\left(\frac{5+\xi}{1-\xi} - \frac{\xi}{x-\xi} \right) \log \xi - 1 \right] \\ & - \frac{\xi}{8} \left(\frac{6}{1-\xi} \log \xi - 1 \right). \end{aligned} \quad (\text{B.8})$$

The gauge invariant functions $Y_0(x)$, $X_0(x)$ and $Z_0(x)$ are defined as:

$$X_0(x) = C(x, \xi) - 4B(x, \xi, 1/2) = C_0(x) - 4B_0(x), \quad (\text{B.9})$$

$$Y_0(x) = C(x, \xi) - B(x, \xi, -1/2) = C_0(x) - B_0(x) , \quad (\text{B.10})$$

$$Z_0(x) = C(x, \xi) + \frac{1}{4}D(x, \xi, 1/2) = C_0(x) + \frac{1}{4}D_0(x) . \quad (\text{B.11})$$

For more details regarding these Inami-Lim functions, we refer the reader to [123].

We now complement the discussion on meson mixing in Sec. 5.1.1. Using the relation (5.9) and $x_u \approx 0$, we rewrite the sum:

$$\sum_{i,j=u,c,t,T} \lambda_{\beta\alpha}^i \lambda_{\beta\alpha}^j F(x_\alpha, x_\beta) \underset{x_u \approx 0}{=} \sum_{i,j=c,t,T} \lambda_{\beta\alpha}^i \lambda_{\beta\alpha}^j [F(x_\alpha, x_\beta) - F(x_\alpha, 0) - F(0, x_\beta) + F(0, 0)] , \quad (\text{B.12})$$

where,

$$F(x_i, x_j) = \frac{1}{(1-x_i)(1-x_j)} \left(\frac{7x_i x_j}{4} - 1 \right) + \frac{x_i^2 \log x_i}{(x_j - x_i)(1-x_i)^2} \left(1 - 2x_j + \frac{x_i x_j}{4} \right) + \frac{x_j^2 \log x_j}{(x_i - x_j)(1-x_j)^2} \left(1 - 2x_i + \frac{x_i x_j}{4} \right) , \quad (\text{B.13})$$

$$F(x, 0) = F(0, x) = -\frac{1}{1-x} - \frac{x^2 \log x}{x(1-x^2)} , \quad (\text{B.14})$$

$$F(0, 0) = -1 . \quad (\text{B.15})$$

Substituting these expressions into Eq. (B.12) yields:

$$F(x_\alpha, x_\beta) - F(x_\alpha, 0) - F(0, x_\beta) + F(0, 0) = S_0(x_\alpha, x_\beta) , \quad (\text{B.16})$$

leading to Eq. (5.10).

We list below the gauge-invariant Inami-Lim functions used for the phenomenological constraints described in Chapter 5.

$$S_0(x_i, x_j) = x_i x_j \left[\frac{(1 - 2x_i + x_i^2/4)}{(x_i - x_j)(1-x_i)^2} \log x_i + \frac{(1 - 2x_j + x_j^2/4)}{(x_j - x_i)(1-x_j)^2} \log x_j - \frac{3}{4(1-x_i)(1-x_j)} \right] , \quad (\text{B.17})$$

$$S_0(x) = \frac{x}{4(1-x)^2} \left[4 - 11x + x^2 - \frac{6x^2}{(1-x)} \log x \right] , \quad (\text{B.18})$$

$$Y_0(x) = \frac{x}{8} \left[\frac{x-4}{x-1} + \frac{3x}{(1-x)^2} \log x \right] , \quad (\text{B.19})$$

$$X_0(x) = \frac{x}{8} \left[\frac{x+2}{x-1} + 3 \frac{x-2}{(x-1)^2} \log x \right] , \quad (\text{B.20})$$

$$Z_0(x) = x \frac{108 - 259x + 163x^2 - 18x^3}{144(1-x)^3} + \frac{24x^4 - 6x^3 - 63x^2 + 50x - 8}{72(1-x)^4} \log x , \quad (\text{B.21})$$

$$E_0(x) = x \frac{18 - 11x - x^2}{12(1-x)^3} - \frac{4 - 16x + 9x^2}{6(1-x)^4} \log x . \quad (\text{B.22})$$

For completeness, we plot these function in Fig. B.1 for $m_T \in [0.1; 10]$ TeV. Note that $S_0(x_T) > S_0(x_t, x_T) \gg S_0(x_c, x_T)$ for $m_T > 1$ TeV. Furthermore, the functions $S_0(x_c, x_T) \approx 2 \times 10^{-3}$, $E_0(x_T) \approx 8 \times 10^{-2}$ and $S_0(x_t, x_T) \approx 10$ exhibit an asymptotic behaviour and $Y_0(x_T) \approx X_0(x_T) \approx Z_0(x_T)$ for $m_T > 3$ TeV. The latter relation is a consequence of $B_0(x_T) \rightarrow 1/4$ and $D_0(x_T) \rightarrow -\frac{7}{18} \log x_T - \frac{19}{36}$ in

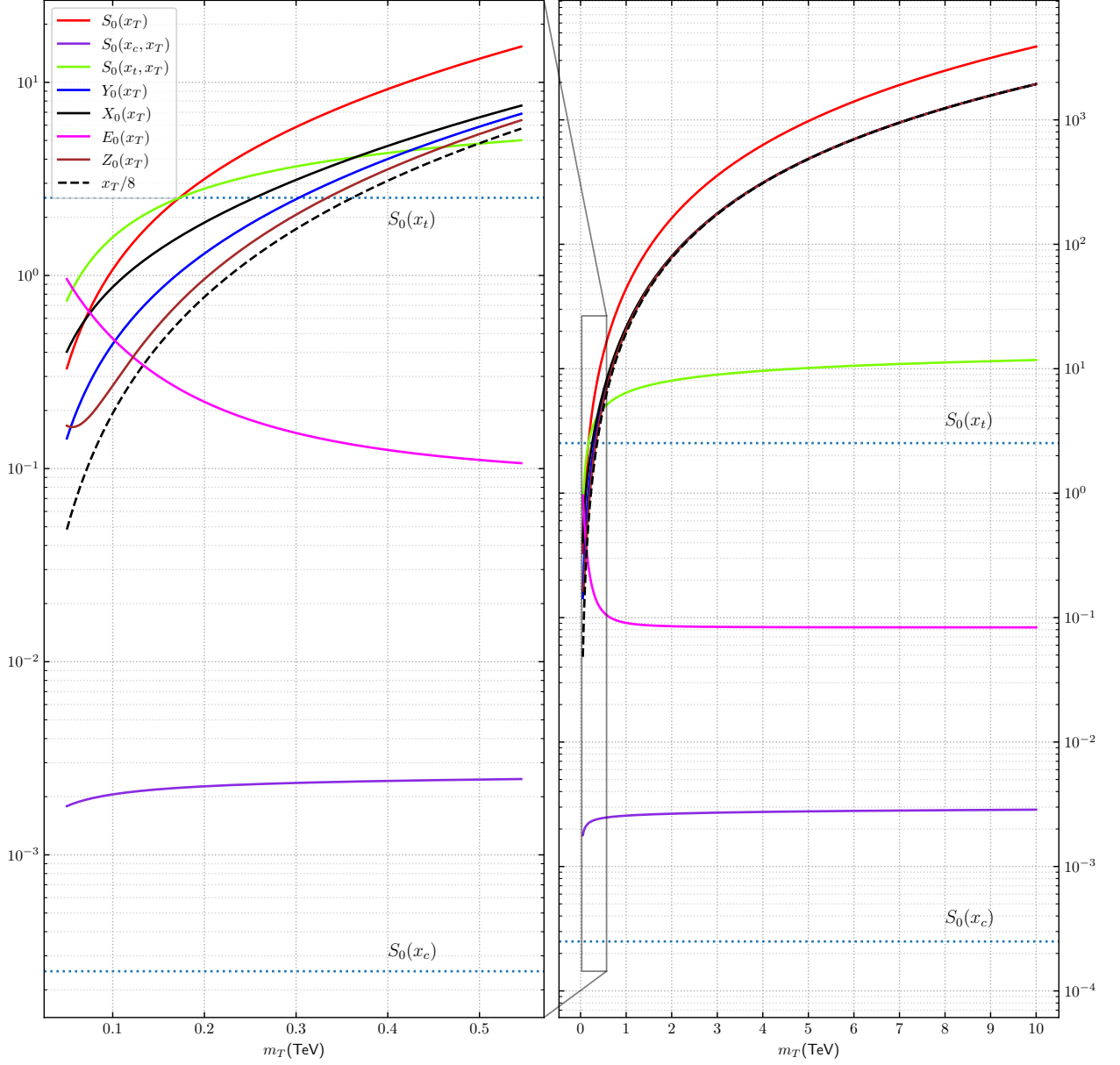


Figure B.1: Inami-Lim functions for $m_T \in [0.1; 10]$ TeV. The dotted blue lines correspond to the values $S_0(x_t) = 2.52$ and $S_0(x_c) = 2.50 \times 10^{-4}$.

the limit $x_T \rightarrow \infty$, while $C_0(x_T) \approx \frac{x_T}{8}$ retains a linear dependence on x_T . To further elucidate this argument, we include this linear relation represented as a dashed curve in the plot.

The loop function entering the expressions regarding the FCNC effect on the penguin diagrams, depicted in Fig. 5.7, is:

$$N(x_i, x_j) = \frac{x_i x_j}{8} \frac{\log x_i - \log x_j}{x_i - x_j}, \quad x_i = x_j \implies N(x) = \frac{x}{8}. \quad (\text{B.23})$$